

SOME TRANSPORT PROPERTIES OF THE
INDIUM ANTIMONIDE / NICKEL ANTIMONIDE
EUTECTIC SYSTEM

by

JEFFREY HARRINGTON

A dissertation submitted for the degree of
Doctor of Philosophy at the University of Salford

September 1970.

ABSTRACT

Some Transport Properties of the Indium Antimonide Nickel Antimonide Eutectic System

The eutectic InSb-NiSb system was found by Wilhelm and Weiss to contain unidirectionally orientated inclusion rods of NiSb in a matrix of InSb.

The Hall coefficient, electrical conductivity and magnetoresistance have been investigated from 77^oK to 650^oK, while thermo-electric power and thermal conductivity measurements have been plotted from 320^oK to 590^oK, on samples cut so that the directional anisotropy could be examined. Of particular interest, a sample orientated so that the inclusion rods, current and magnetic field are mutually perpendicular changes its resistance by a factor 9 (at 7kg) at 300^oK.

Measurements well above 300^oK show a general convergence of properties, while well below this temperature the samples become p-type, with electrical conductivity progressively falling.

For rods parallel to the temperature gradient the thermo-electric power decreases from 184 μ V^oK⁻¹ at 320^oK to 156 μ V^oK⁻¹ at 600^oK, whereas rods parallel to the temperature gradient show a much sharper fall from 265 μ V^oK⁻¹ to 154 μ V^oK⁻¹ at the same temperatures, accompanied by thermal conductivity values of lesser disparity.

The size and distribution of the inclusions was probed by stereoscan electron microscopy, giving average dimensions of length 2.20 μ , and diameter 0.72 μ .

The modifications in Hall effect and magnetoresistance brought about by the inclusions can be explained by comparison with similar values obtainable from pure InSb samples of various geometries, while the thermo-electric power and thermal conductivity can be explained by a model based on the nature of the inclusions.

ACKNOWLEDGEMENTS

It is with great pleasure that I take this opportunity of thanking my supervisor, Dr. A. D. Stuckes, Senior Lecturer in Physics at Salford University, for all the help, encouragement and inspiration which she has constantly provided in the course of this work.

I am also indebted to Professor R. S. Tebble for his benevolence and the goodwill he has borne me.

Thanks are also due to my colleagues Mr. I. John, Mr. M. Aspland and Mr. A. Simpson for the many interesting and helpful discussions we have had.

Lastly, I would like to express my gratitude to Miss E. Burgess, Mr. S. Gothard, Mr. W. Scott and Mr. G. Atkins for the practical assistance they have rendered in various ways which has greatly facilitated this work.

CONTENTS

List of Figures.	Page
CHAPTER 1	
1.1 INTRODUCTION	1
1.1.1 Energy Bands in Solids	1
1.1.2 Effective Mass and Positive Holes	4
1.1.3 Metals, Insulators and Semiconductors	5
1.1.4 Intrinsic and Extrinsic Semiconductors	6
1.1.5 Lattice Vibrations	8
1.1.6 Scattering Mechanisms	10
1.2 INDIUM ANTIMONIDE AND THE 3-5 COMPOUNDS	13
1.2.1 Crystalline Structure	13
1.2.2 Binding Mechanism	13
1.2.3 Band Structure of Indium Antimonide	14
1.2.4 Indium Antimonide and other 3-5 Compounds	16
1.2.5 Alloys of InSb and Other 3-5 Compounds	17
1.2.6 Controlled Eutectic Systems	19
CHAPTER 2	
2.1 ELECTRICAL PROPERTIES OF EXTENDED SAMPLES	22
2.1.1 Simple Hall Effect	22
2.1.2 Associated Effects	23
2.1.3 Transverse Magnetoresistance	23
2.1.4 Relaxation Time and Drift Mobility	25
2.1.5 Electrical Conductivity	29
2.1.6 Hall Coefficient	30
2.1.7 Acceptor Concentration and Hole Mobility	31
2.1.8 Electron Concentration and Electron Mobility	32
2.1.9 The Hall Angle	33
2.1.10 Transverse Magnetoresistance	33

CONTENTS

2.2	ELECTRICAL PROPERTIES OF NON-EXTENDED SAMPLES	35
2.2.1	Geometrical Effects	35
2.2.2	Pseudo-Geometrical Effects	40
2.2.3	Isolated Inclusions	42
2.3	THERMOELECTRIC POWER	44
2.4	THERMAL CONDUCTIVITY	47
2.4.1	The Lattice Component	48
2.4.2	The Electronic Component	50
CHAPTER 3		
3.1	ELECTRICAL METHODS	53
3.1.1	Operation of the Electrical Circuit	53
3.1.2	The Measuring Circuit	57
3.1.3	Measurement Procedure and Accuracy	60
3.1.4	The Sample Holder	61
3.1.5	The Furnace	62
3.1.6	Simple Cryostat	65
3.1.7	Magnet and Fluxmeter	66
3.1.8	Sample Preparation and Experimental Errors	69
CHAPTER 4		
4.1	THERMAL METHODS	71
4.1.1	Thermal Conductivity and Thermoelectric Power	71
4.1.2	Sample Preparation and Stack Assembly	72
4.1.3	Measurement Procedure	75
4.1.4	Theory of the Comparative Method	76
4.1.5	Experimental Errors	77

CONTENTS

CHAPTER 5	
5.1	STEREOSCAN ELECTRON MICROSCOPY 78
5.1.1	Structure of InSb/NiSb 78
CHAPTER 6	
6.1	ELECTRICAL PROPERTIES OF InAs 80
CHAPTER 7	
INTERPRETATION OF EXPERIMENTAL RESULTS 83	
7.1	Electrical Properties of InSb/NiSb 83
7.1.1	Electrical Conductivity 83
7.1.2	Hall Coefficient 87
7.1.3	Transverse Magnetoresistance
7.2	THERMOELECTRIC POWER 101
7.3	THERMAL CONDUCTIVITY 105
7.4	DISCUSSION 109
CHAPTER 8	
CONCLUSION	
REFERENCES	
APPENDICES OF TABULATED RESULTS	
1	Electrical conductivity of InSb at room temperature
2	Electrical conductivity of InSb/NiSb at various temperatures
3	Electrical conductivity of InSb/NiSb vs. temperature
4	Measured Hall coefficients of InSb/NiSb vs. temperature
5	ρ_{xx} vs. ρ_{xy} for InSb/NiSb
6	ρ_{xx} vs. ρ_{xy} for InSb/NiSb

LIST OF FIGURES

1. (a) Kronig-Penney potential (b) Sommerfeld model
(c) Bloch wave model
2. The Wilson model
3. Donor and Acceptor levels
4. Band structure of InSb
5. Geometrical component, r_g v. \tan (Hall Angle, θ_m)
6. (a) $G(\lambda/\omega, \theta_m)$ v. λ/ω (b) $G(\lambda/\omega, \theta_m)$ v. θ_m
7. Composite model for InSb/NiSb
8. Simplified electrical circuit
9. Chopper settings and currents
10. The measuring circuit
11. The furnace
12. Electrical circuit of the furnace
13. Temperature control settings
14. Temperature profile of the furnace
15. The Cryostat
16. The Stack assembly
17. Heat flow through the stack
18. Distribution curves of the inclusion dimensions
19. Hall coefficient of InAs v. Temperature
20. Electrical conductivity of InAs v. Temperature
21. Electron mobility of InAs v. Temperature
22. Magnetoresistance of InAs at room temperature
23. Composite model for InSb/NiSb samples in orientations A and B
24. Electrical conductivity of InSb/NiSb v. Temperature
25. Measured Hall coefficients of InSb/NiSb v. Temperature
26. $n_i/T^{3/2}$ v. T^{-1} for InSb/NiSb
27. $|R_H^x|/\sigma$ v. T for InSb/NiSb

28. Properties of InSb/NiSb in orientation A at 294°K .
29. Properties of InSb/NiSb in orientation A at 367°K .
30. Properties of InSb/NiSb in orientation A at 528°K .
31. Properties of InSb/NiSb in orientation A at 698°K .
32. Properties of InSb/NiSb in orientation B at 294°K .
33. Properties of InSb/NiSb in orientation B at 377°K .
34. Properties of InSb/NiSb in orientation B at 529°K .
35. Properties of InSb/NiSb in orientation B at 696°K .
36. Properties of InSb/NiSb in orientation C at 292°K .
37. Properties of InSb/NiSb in orientation C at 370°K .
38. Properties of InSb/NiSb in orientation C at 529°K .
39. Properties of InSb/NiSb in orientation C at 683°K .
40. Thermoelectric power of InSb/NiSb v. Temperature
41. Thermal conductivity of InSb/NiSb v. Temperature
42. Lattice thermal conductivity of InSb/NiSb v. Temperature

CHAPTER 1

1.1. INTRODUCTION

1.1.1. Energy Bands in Solids

The fact that many crystalline solids are good conductors of electricity enables them to be pictured as fairly regular matrices of atomic cores through which electrons may drift under the influence of an applied electric field. The large number of interacting particles make an approximation process essential before wave mechanics can be used to account for the physical properties of the solids.

An extensively used model is the "One Electron" approximation in which the field experienced by a given electron arises from the fixed atomic cores plus an averaged contribution produced by all the other electrons.

On this basis two widely used theoretical approaches are founded. One starts with the properties of free atoms, which are relatively well known, and investigates the changes that occur in these properties when the atoms are brought together. This is the Heitler-London approach and is most useful in dealing with low mobility solids. In such materials the electron is strongly influenced by particular atomic cores and may be treated in terms of localised wave functions. The alternative method, of more general application, is to idealise the solid into a completely regular array of atomic cores and to assume that the electron belongs to the crystal as a whole, rather than any particular atomic core.

A useful criterion for selecting the right approach involves the de Broglie wavelength of a "thermal" electron. If this is smaller than, or comparable to, the lattice parameter the former approach should be used. If, however, the de Broglie wavelength is much

larger than the lattice parameter, the latter approach is preferable.

The Heitler-London case deals with an electron moving in a hydrogen-like potential field, whereas in the other case two different types of potential field have been postulated by Sommerfeld² and Bloch.³

In Sommerfeld's "Free Electron" model, originally applied to metals, the electron was pictured as a plane wave moving freely through a constant potential field, with impenetrable walls at the crystal boundary. Solving Schrödinger's equation for such a potential shows that the electron takes on quantised energy values, proportional to the square of the permitted values of wave vector.

$$\text{i.e. } E = \frac{\hbar^2 k^2}{2m} \quad \text{and} \quad k = \frac{2\pi}{\lambda} = \frac{p}{\hbar}$$

In these equations \hbar is the reduced value of Planck's constant, k is the wave vector of the electron of mass m , de Broglie wavelength λ and momentum p .

In contrast, Bloch pictured the electron moving through a perfectly periodic potential produced by the regular arrangement of atomic cores of the crystal lattice. The electron was then represented by a plane wave modulated by the periodicity of the lattice. Departures from perfection, such as grain boundaries, dislocations and foreign atoms, were then shown to be responsible for the electrical resistance of the material.

The use of periodically modulated wave functions (called Bloch functions) leads to two further extremely important results, namely, that allowed energy bands exist, which are separated by forbidden regions and that the functions $E(k)$ are periodic in k .

In order to locate the energy discontinuities, the form of the periodic potential must be specified. For the present discussion

the simple one dimensional array of potential wells first used by Kronig and Penney⁴ serves this purpose. This is shown in Fig.1(a).

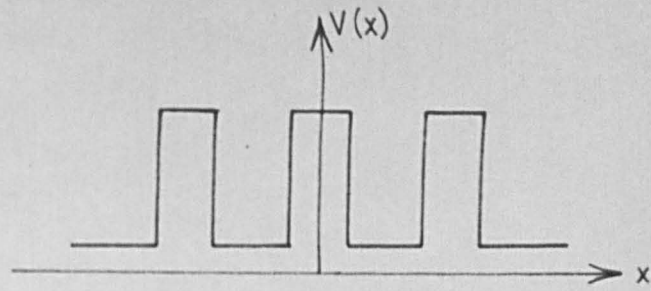
The solution of Schrodinger's equation then shows that the wave vectors associated with the energy discontinuities are given

$$\text{by } k = \frac{n\pi}{a} \quad \text{for } n = \pm 1, \pm 2, \pm 3 \dots\dots\dots$$

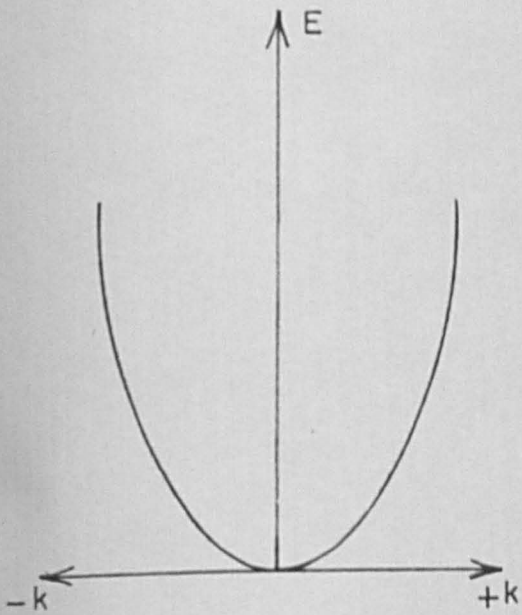
these values of k defining the so called Brillouin Zones. The modification to the $E - k$ curve brought about by using the Bloch model with a Kronig-Penney potential, in preference to the Sommerfeld model are illustrated in Figs. 1(b) and 1(c). Since the energy is a periodic function of the wave vector repeating at intervals of $2\pi/a$, "reduced wave vector" energy band diagrams can be used as in Fig. 1(c). This also leads to the conclusion that the $E - k$ curve must cut the zone boundaries normally. Consideration of the wave functions at the edges of the Brillouin Zones shows that the electron waves suffer strong reflection, setting up stationary wave systems governed by the Bragg reflection condition. Electrons of the corresponding energies do not occur naturally in crystals and if they are introduced artificially, they are Bragg reflected out of the crystal and cannot take part in conduction processes.

In three dimensions the fundamental range $\pm\pi/a$ or 1st Brillouin zone becomes a polyhedron in k -space. The property of undergoing Bragg reflection, commonly shared by electrons and x -rays suggests that the symmetry of the crystal lattice determines the shape of the Brillouin zone. It is necessary to draw $E - k$ diagrams for specified crystallographic directions and their shapes are determined by the nature of the lattice atoms and their proximities in the unit cell. Consequently the band structures are more complicated than that appearing in Fig. 1(c). For example, more than one energy minimum may exist as in germanium and silicon, or the width of the

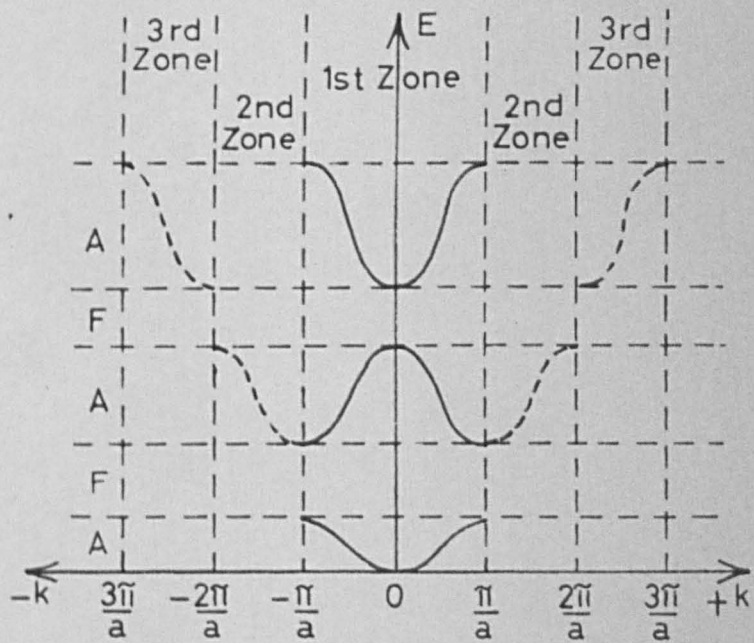
Fig. 1



(a) KRONIG-PENNEY POTENTIAL



(b) SOMMERFELD MODEL



(c) BLOCH WAVE MODEL

A: Allowed Band
F: Forbidden Band

SCHEMES :-

- Reduced wave vector (one zone model)
- Full wave vector (many zone model)

forbidden band may vary with crystalline direction. The latter may result in the overall absence of a forbidden region as a consequence of overlapping energy bands. This frequently occurs in metallic substances, accounting for the metallic conduction of divalent elements.

The number of electrons held by a given energy band may be estimated by considering the perturbation of the atomic levels of a single atom brought about by other atoms. In a single atom the allowed energy levels are discrete. As two similar atoms approach each energy level is split so that the binary system consists of two closely spaced energy levels which separate at closer distances of approach. Therefore, N well separated similar atoms coalescing to lattice parameter separations in forming a crystal, create N closely spaced energy levels in each energy band. Pauli's exclusion principle showed that each level can be occupied by two electrons of opposite spin, so that a full band contains $2N$ electrons.

The uppermost filled energy band is labelled the "Valence Band" while the next higher energy band is called the "Conduction Band".

1.1.2. Effective Mass and Positive Holes.

Bloch's model gives, to a good approximation, a spherically symmetrical minimum to the conduction band with

$$E = \frac{\hbar^2 k^2}{2m^*}$$

This is similar to Sommerfeld's expression, with a different constant of proportionality. The electron behaves as if it has a mass m^* , different to m , called the "Effective mass" of the electron. Simple analysis of the motion of the electron in an electric field shows that

$$m^* = \hbar^2 / \frac{d^2 E}{dk^2}$$

whereas for the general case of non-spherical energy bands m^* takes the form of a tensor. The interaction of the electron with the lattice is, however, clearly responsible for the difference between m and m^* .

In a full band electrical conduction is impossible since the electrons in the band cannot accept energy from an applied electric field as there are no neighbouring states of higher energy into which the electron may move. If, however, there is an unoccupied energy state in the band an electron can transfer to it and acquire a drift velocity from the electric field. Near the top of a full band the electron has a negative effective mass so that it moves in the direction of the applied electric field. The current which results is then equivalent to that obtained from a positively charged electron with a positive effective mass in the same electric field. Unoccupied energy states in almost filled energy bands are, therefore, termed positive holes.

1.1.3. Metals, Insulators and Semiconductors.

The forgoing ideas were used by A. H. Wilson⁵ to make a clear distinction between different types of crystalline solids.

An insulator is pictured as being composed of energy bands which are either completely full or completely empty at all temperatures up to the melting point. The bands are so remotely separated that inter-band transitions of carriers brought about by thermal means and governed by the Boltzmann factor may be practically neglected.

A metal contains energy bands which are incompletely filled so that conduction can take place by the movement of electrons into higher energy states under the influence of an applied electric field, the number of conduction electrons remaining constant with increased temperature.

In semiconductors the valence band is separated from the conduction band by an energy gap, E_g , as in Fig.2. Therefore, above absolute zero, a number of carriers governed by the Boltzmann factor, $\exp(-E_g/kT)$, are excited from the valence band into the conduction band. The resulting exponential increase in electrical conductivity with temperature is a striking feature of semiconductors and provides a ready means of identification.

1.1.4. Intrinsic and Extrinsic Semiconductors.

In an intrinsic semiconductor, each electron excited into the conduction band leaves a positive hole in the valence band, so that electron conduction may occur in the conduction band simultaneously with hole conduction in the valence band. By adding small amounts of other elements to intrinsic semiconductors the concentrations of electrons and holes in their respective bands may be drastically altered, causing great changes in electrical properties. For example, by adding a one millionth part of Boron to pure Silicon the electrical conductivity is increased by a factor of one thousand at room temperature.

In Germanium and Silicon each tetravalent atom forms bonds with four like atoms at the corners of a regular tetrahedron. Although the valence electrons are in rapid motion and exchange positions with each other at absolute zero there are, on average, two electrons in each bond. Satisfying the valence requirements of each atom in this way clearly leads to a filled valence band, so that no electrical conduction results from the motion of the valence electrons. If a pentavalent impurity atom is substituted for one of the lattice atoms it becomes bonded to its neighbours by four electrons leaving one electron loosely bound to the impurity atom, by forces resembling those present in a hydrogen atom. Above absolute zero the fifth electron is readily excited above its ground state and at comparatively low

Fig. 2

THE WILSON MODEL

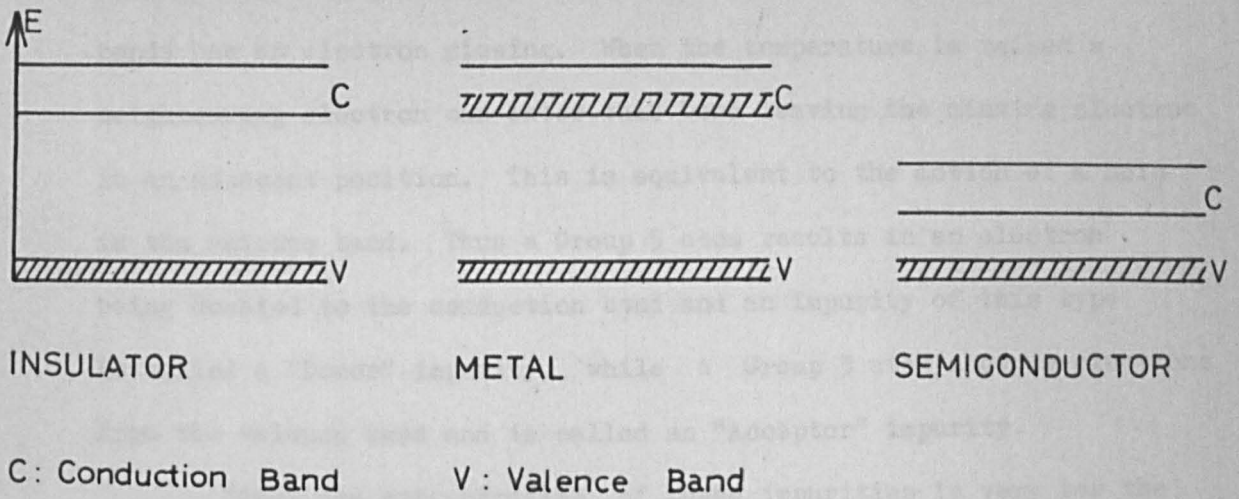
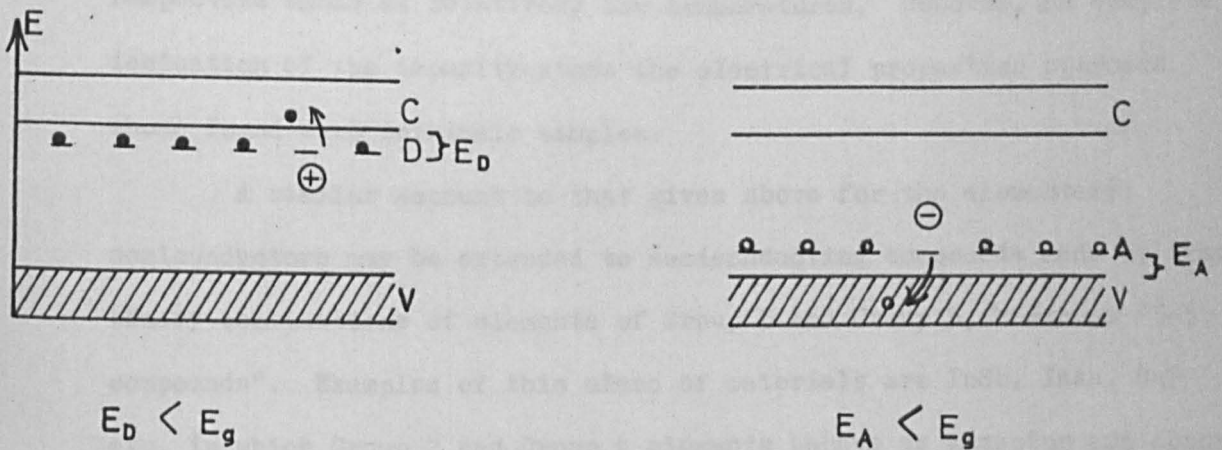


Fig. 3

DONOR AND ACCEPTOR LEVELS



•: Donor Electrons

◦: Acceptor Holes

⊕: Localised Positive Ion

⊖: Localised Negative Ion

temperatures the impurity atom becomes ionised and the electron is excited into the conduction band. Similarly, if a trivalent atom is substituted for a lattice atom, at absolute zero, it becomes bonded to its neighbours by three electrons so that one of the four bonds has an electron missing. When the temperature is raised a neighbouring electron can enter this bond leaving the missing electron in an adjacent position. This is equivalent to the motion of a hole in the valence band. Thus a Group 5 atom results in an electron being donated to the conduction band and an impurity of this type is called a "Donor" impurity, while a Group 3 atom accepts electrons from the valence band and is called an "Acceptor" impurity.

Since the concentration of these impurities is very low the impurity atoms are so far apart that no splitting of the atomic levels occurs, so that "Acceptor Levels" and "Donor Levels" are formed, as in Fig.3. These levels may reside in the normally "Forbidden" energy region of an intrinsic semiconductor, allowing localised charge carriers to be excited from their impurity levels into their respective bands at relatively low temperatures. However, on complete ionisation of the impurity atoms the electrical properties approach those found with intrinsic samples.

A similar account to that given above for the elementary semiconductors may be extended to semiconducting compounds made up from binary combinations of elements of Group 3 and Group 5, known as "3-5 compounds". Examples of this class of materials are InSb, InAs, GaP etc. in which Group 2 and Group 6 elements behave as acceptor and donor impurities, respectively.

The electrical resistance of 3-5 compounds may, however, originate from quite different sources than in elementary semiconductors. A prime difference occurs in the scattering of carriers by means of thermal vibrations of the crystal lattice, which will

now be discussed.

1.1.5. Lattice Vibrations.

An early treatment of the thermal vibrations of a crystal lattice was put forward by Debye⁶ in his treatment of the thermal conductivity of an insulator. The lattice was pictured as a continuum in which the atoms vibrated as in a compression wave of frequency ω and wave vector q , where $\omega = vq$ and v is the velocity of propagation of the wave.

Classical consideration of the lattice as a coupled harmonic oscillator, shows that Debye's model becomes inadequate as the wavelength decreases and approaches the lattice parameter. As this happens, the linear frequency wave vector relation breaks down and gives way to a periodic relationship similar to that obtained between the energy, $E(\underline{k})$ and the wave vector, \underline{k} , for electrons in a periodic potential.

Thus a Brillouin Zone may also be defined between the frequency $\omega(\underline{q})$ and the wave vector \underline{q} . Within the Brillouin Zone there exists for each value of wave vector a discrete vibration spectrum. In a given direction of a diatomic lattice this consists of three "Acoustic" modes separated by a frequency gap from three "Optical" modes. The term "Acoustic" refers to the lower frequency branches in which neighbouring atoms move in phase, in the manner of compression waves. The term "Optical" is applied to the upper frequency branches, in which neighbouring atoms possess different charges (e.g. Na^+ , Cl^-) and move in antiphase. This constitutes a fluctuating dipole moment which may couple with electro-magnetic waves to produce strong absorption in the infra-red range.

Quantum mechanical treatment of the lattice as a coupled harmonic oscillator shows that the vibrational energy of the atomic cores, induced by a particular mode of vibration in a particular

branch of the vibration spectrum, is quantised according to the rule.

$$E(q) = \hbar\omega(q) \left(N(q) + \frac{1}{2} \right) \quad (1.1)$$

where $N(q)$ is zero or a positive integer. Equation (1) describes a mode of vibration containing N "phonons" or N quanta of energy $\hbar\omega_q$. The mode may, therefore, change its energy providing a mechanism exists whereby the number of phonons contained by the mode may be altered. In the idealised insulating crystal discussed so far, no such mechanisms are available, so that the energy of each mode is distributed uniformly throughout the crystal and is non-localised in space. By consideration of the perturbations brought about by the anharmonic forces that exist in actual crystals, it may be shown that energy is exchanged between the modes of the unperturbed system so that the number of phonons in a particular mode may change with time.

By treating phonons as wave packets of energy which may permeate the crystal, an account of the energy transfer processes involved in thermal conduction may be given. Such wave packets possess energy $E = \hbar\omega(q)$, Group Velocity, $v(q) = \frac{d\omega(q)}{dq}$ and momentum $\hbar q = \frac{\hbar\omega(q)}{u}$, where u is the velocity at which acoustic waves are propagated through the crystal.

In a perfect crystal a phonon wave packet moves freely through the crystal with a momentum that is constant in time. However, in real crystals the wave packet may collide with another wave packet or with localised imperfections. In these collisions wave packets may be created or destroyed entirely, in such a way that the total energy is conserved. Such collisions continually occur so that, in thermal equilibrium, a particular branch of the vibration spectrum contains a time averaged number of phonons given by the

Bose-Einstein formula

$$N(q) = \left(\exp \frac{\hbar\omega(q)}{kT} - 1 \right)^{-1} \quad (1.2)$$

The occurrence of such thermal vibrations in semiconductors provides a mechanism by which charge carriers may be scattered.

1.1.6. Scattering Mechanisms

At a given temperature the concentration of charge carriers present in a semiconductor is constant. Therefore, the electrical conductivity is limited by the velocity at which the carriers drift in the direction of the electric field, between collisions with various types of lattice discontinuity. In a unit electric field this velocity is termed the carrier mobility, μ , and from the variation of mobility with temperature, T , it is sometimes possible to deduce the predominant scattering source.

From equations (1.1) and (1.2) it is evident that at a constant temperature an atomic core of the crystal lattice possesses a quantised amount of vibrational energy. As the temperature is lowered the vibrational energy of the atomic core reduces in quantum steps of magnitude $\hbar\omega(q)$, until eventually only the "zero point" energy, $\frac{1}{2}\hbar\omega(q)$ is left at absolute zero. In a collision process between, say, an electron and an atomic core, a phonon of energy $\hbar\omega(q)$ must either be emitted, or absorbed, by the atomic core. In order to scatter electrons a phonon must, therefore, be given up by the atomic core. As the temperature is lowered, however, the atomic core has progressively less phonons available to scatter electrons so that electron-phonon scattering diminishes and vanishes completely at absolute zero. At higher temperatures the number of lattice vibrations of a particular frequency is given by equation (1.2), so that lattice scattering increases.

For the acoustic modes of vibration, as a result of the movement of neighbouring atomic cores in the same direction, the lattice spacing varies periodically causing a small perturbation of the crystal potential. This perturbation moves through the crystal at the velocity of sound, so that, at ordinary temperature, much faster moving thermally excited electrons encounter a periodically perturbed lattice. Calculations based on this model show that, except at low temperatures, the electrons suffer isotropic scattering with little loss of energy giving a $\mu_e \propto T^{-3/2}$ temperature dependence.

Scattering by the higher energy or "Optical" mode originates in movement of neighbouring atoms, possessing different charges, in opposite directions. The fluctuating dipole moments set up in this way may couple strongly with the charge carriers to produce a scattering law of the form

$$\mu \propto T^{1/2} F(\theta_l/T) (\exp(\theta_l/T) - 1)$$

In this formula θ_l is the optical mode temperature and $F(\theta_l/T)$ is a slowly varying function of T . At high temperatures where $T \gg \theta_l$ the mobility becomes proportional to the square root of the absolute temperature. At low temperature, however, insufficient energy is available for excitation of the optical modes and this type of scattering, which clearly cannot occur in elementary semiconductors, is generally superseded by another, such as ionised impurity scattering.

Previously it was mentioned that in the extrinsic range, semiconductors owe their electrical conductivity to carriers which are thermally excited from impurity atoms into appropriate band. The remaining ionised impurities form point sources by which the free carriers may be scattered. The charge on the impurity atoms is modified by the free carriers present, forming a screened coulomb

potential⁸ which causes Rutherford scattering. As a result, the faster carriers are preferentially scattered less and a $\mu \propto T^{3/2}$ scattering law emerges.

In the intrinsic range ionised impurity scattering becomes less important as lattice scattering increases. Additionally, scattering may occur between intrinsic electrons and holes. If the effective mass of the holes is much larger than the effective mass of the electrons, then the scattering processes become essentially similar to ionised impurity scattering, with a similar temperature dependence.

Collisions between carriers of the same type are more complex and tend to redistribute the momentum⁹ of the carriers ensuring that the carriers have an equilibrium distribution of energy. They are generally regarded as unimportant, except under very degenerate conditions.

Further sources of scattering are neutral atoms and lattice dislocations. Neutral atoms¹⁰ act as scattering centres that are independent of carrier velocity and temperature, with a mobility that is inversely proportional to their density. Dislocations¹¹ also scatter electrons by means of the lattice distortion they produce. Again this usually proves to be an unimportant mechanism compared with lattice scattering and ionised impurity scattering in the upper regions of the extrinsic range, but may well dominate at very low temperatures in pure semiconductors.

The relative importance of these scattering mechanisms in indium antimonide and indium arsenide is discussed later, after due consideration of the general properties of these compound semiconductors.

1.2. INDIUM ANTIMONIDE AND THE 3-5 COMPOUNDS

1.2.1. Crystalline Structure.

In common with the elementary semiconductors, Germanium and Silicon, the 3-5 compound semiconductors also form lattices in which each atom is surrounded by four nearest neighbours. The elements crystallise in the Diamond structure while the compounds form the Zinc Blende (ZnS) structure. Each may be described as two face centred cubic lattices, the main difference being that in the diamond lattice all the atoms are identical and in the zinc blende structure the two sublattices contain different atoms. The lattices of both types of atoms are orientated parallel and displaced by a vector $(a/4, a/4, a/4)$, where a is the lattice parameter. If, in a single crystal, a single layer of atoms of one sublattice is labelled A and a single layer of the other sublattice is labelled B the succession of layers in the (111) direction is ABABAB..., whereas in the $(\bar{1}\bar{1}\bar{1})$ direction the succession is BABABA..., so that the two directions are distinguishable. In the diamond lattice, since $A = B$, there is clearly an inversion centre which is absent in the zinc blende lattice.

1.2.2. Binding Mechanism.

In the elementary semiconductors each tetravalent atom is surrounded by four identical nearest neighbours so that purely covalent bonds are formed. In materials having a zinc blende structure, however, each atom is surrounded by four nearest neighbours of different type. Between any two nearest neighbours the number of valence electrons is eight, so that each atom has on average four electrons available for the formation of bonds. Consequently covalent bonding can occur, even though it cannot be expected to be completely identical with the bonding of the diamond lattice, because of the unequal charges on the atomic cores. In germanium for instance, the

atomic cores are all Ge^{4+} ions, whereas in InSb they are In^{3+} and As^{5+} ions.

In forming a covalent bond the indium core must acquire a net negative charge while the arsenic core must acquire a net positive charge, the resulting ionicity providing a stronger bond than the purely covalent case. Coulson, Redei and Stocker¹² calculated the effective charges e^* on the A atoms of the A B compounds, some of which are listed below, in order of increasing ionicity.

Compound	GaSb	AlSb	GaP	GaAs	InSb	AlAs	InP	InAs
e^*/e	0.43	0.44	0.45	0.46	0.46	0.47	0.49	0.49

The electronic polarisations have been shown to generally correspond to the listed values by Sirota,¹³ using x-ray electron mapping techniques on the antimonides and arsenides of indium and gallium.

1.2.3. Band Structure of Indium Antimonide.

The energy gap, derived from optical measurements near the fundamental absorption edge, has been shown by Roberts and Quarrington¹⁴ to be strongly temperature dependent, reducing from 0.23 eV at 0°K to 0.18 eV at room temperature.

Cyclotron resonance work on n-type indium antimonide by Desselhaus¹⁵ et al, gave an effective mass of 0.013m for electrons in the conduction band. The resonant frequency proved to be independent of crystal orientation suggesting that the conduction band has spherical symmetry.

Further work by Desselhaus et al on p-type indium antimonide gave resonance lines corresponding to a hole effective mass of 0.18m, and suggested the possibility of another hole effective mass

greater than $1.20m$. The former effective mass is attributed to the uppermost valence band while the latter value remains unexplained and is not considered to be reliable.

Using the above information on symmetry, energy gap and effective mass, Kane¹⁶ was able to make a detailed calculation of the band structure, the results of which will now be outlined.

The conduction band, C, is parabolic, having spherical symmetry about the minimum at $k = 0$, but the curvature decreases with increasing k , giving an increased effective mass, as shown in Fig.4.

The valence band in the elementary semiconductors consists of three twofold degenerate bands. These are a heavy hole band, V_1 , and a light hole band, V_2 , which are degenerate at $k = 0$ and a split off band V_3 . A similar valence band structure exists in InSb and other 3-5 compounds except that due to the lack of inversion symmetry mentioned in section 1.2.1. the V_1 and V_2 bands are just resolved.

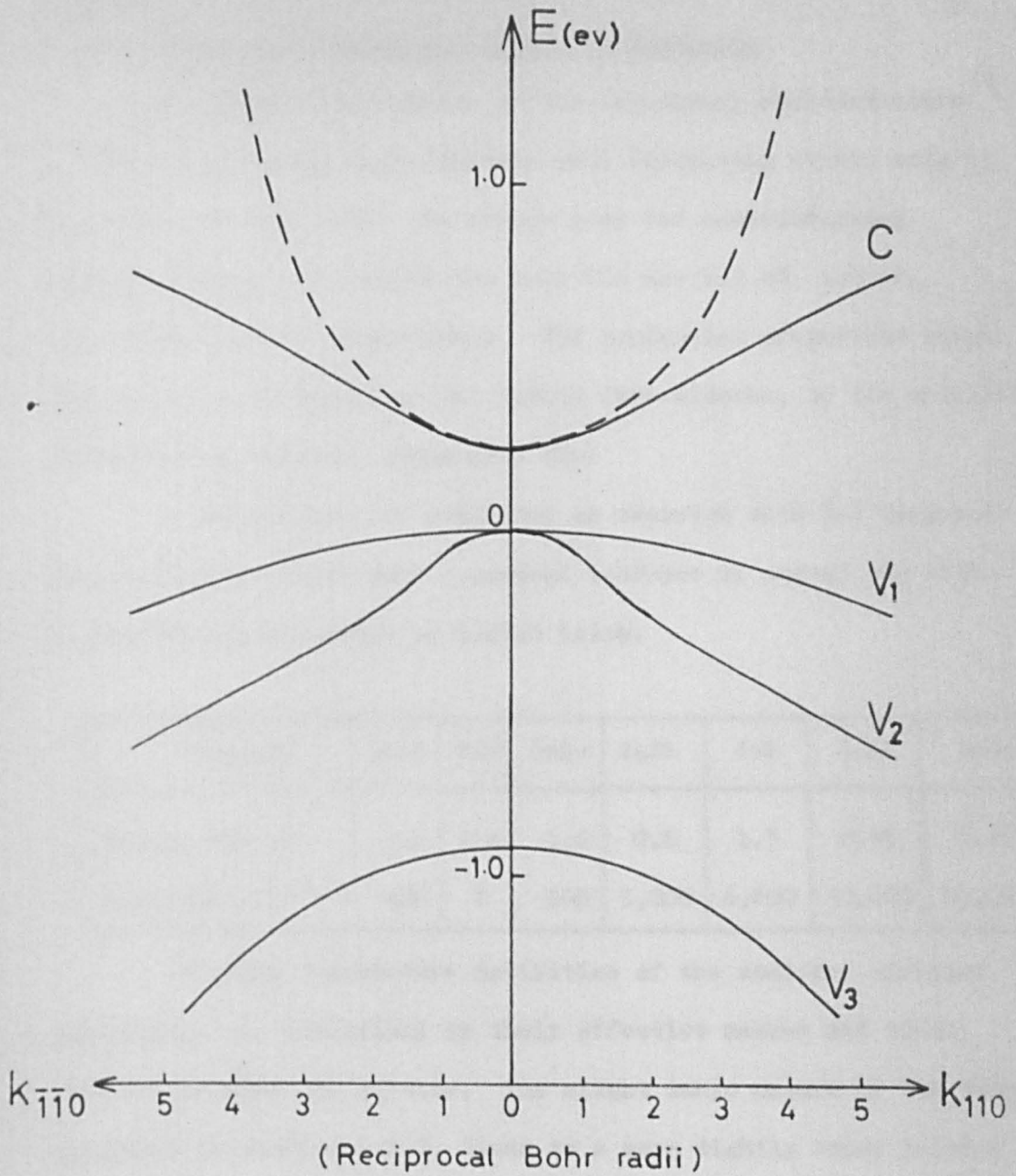
As the value of k increases the bands lose their parabolic nature and the interaction of the lower lying bands splits the V_1 and V_2 bands by an amount proportional to k . The split off band V_3 is similar to the V_2 band but contains no terms linear in k .

The magnitude of the spin-orbit splitting of the valence bands is not known experimentally, but from the splittings of the p-functions in single atoms of In and Sb Kane was able to deduce a value of 0.9 eV by assuming that the valence electron spends 65 per cent of the time on the Sb atom and 35 per cent of its time on the In atom.

Attempts to identify the light hole effective mass directly from cyclotron resonance experiments have so far been unsuccessful. A value of $0.012m$ has been suggested by Fan and Gobel¹⁷, from infrared work, and also by Champness¹⁸ from magnetoresistance measurements, but

Fig. 4

BAND STRUCTURE OF InSb



Splitting of the two fold degeneracy has not been included.

— — — — Parabolic approximation for the conduction band.

more evidence is required before this value can be fully accepted.

1.2.4. Indium Antimonide and other 3-5 Compounds.

An interesting feature of the elementary semiconductors is that their energy gaps decrease with increasing atomic weight. Classified in this order the energy gaps for semiconducting Diamond, Silicon, Germanium and Gray Tin are 5.3 eV, 1.2 eV, 0.9 eV and 0.08 eV respectively. The conduction properties range from almost pure insulator for defect free diamond, to the metallic conduction of strongly doped gray tin.

A similar sort of behaviour is observed with 3-5 compound semi-conductors which show a general decrease in energy gap with increasing atomic weight as listed below.

Compound	Alsb	GaP	GaAs	GaSb	InP	InAs	InSb
Energy Gap eV.	1.6	2.4	1.6	0.8	1.3	0.45	0.25
Mobility $\text{cm}^2\text{V}^{-1}\text{s}^{-1}$	400	?	600	5,000	4,600	30,000	80,000

The room temperature mobilities of the dominant carriers (electrons) are determined by their effective masses and their interaction with the lattice. The slight ionic nature of the compounds mentioned in section 1.2.2. leads to a more tightly bound lattice than is possible with covalent elementary semiconductors. This increased rigidity results in a weaker interaction between the charge carriers and the crystal lattice. Consequently there is an increase in the carrier mobility which generally runs parallel with increasing atomic weight. InSb, however, has a smaller ionicity and a greater carrier mobility than InAs. This results from the comparatively small effective mass of the electrons in InSb.

The very high mobilities of both these semiconductors make

them interesting device substances, with applications in magneto-resistance and infra-red detector fields. The inherent properties of these and other 3-5 semiconductors may be modified by suitable alloying procedures.

1.2.5. Alloys of InSb and other 3-5 Compounds

Alloys of 3-5 semiconductors, taken in pairs, have been prepared and studied. The pairs are generally chosen to have one element in common, for example, InSb-GaSb, GaAs-GaP. A requirement for the formation of these mixed crystal systems is that the lattice parameters of the two participant systems, which are determined by the atomic sizes of the elementary constituents, should not be very different. In addition, since each component has polarised bonds, the binding of the resultant lattice must also have an ionic contribution. Therefore, in order to avoid strong distortion of the crystal lattice, the two components must have similar polarisations. The ionicity table in section 1.2.2. shows that the InAs-InP system is probably easier to prepare than the InSb-InAs system. However, the difference in the size of the As and P ions is such that a mixed crystal is unlikely to be formed.

The InSb-GaSb system shows that with increasing ^{14,20} GaSb content there is a linear decrease in lattice parameter accompanied by an almost linear increase in optical energy gap. This is confirmed by electrical measurements up to 60 mole % GaSb, after which differences appeared between the sets of results obtained from the two types of measurement. The electron mobility decreases rapidly from the value $60,000 \text{ cm}^2 \text{ V}^{-1} \text{ s}^{-1}$ for pure InSb, flattening to $10,000 \text{ cm}^2 \text{ V}^{-1} \text{ s}^{-1}$ for the 40:60 alloy.

The scattering mechanisms operating in these alloys are unknown, but the mobilities do not seem to be influenced by the statistical distribution of dissimilar atoms of the components.

The situation is different for energy transport by phonons through the lattice. Internal stresses brought about by the alloying process reinforce the anharmonicity of the lattice vibrations. Consequently phonons are more strongly scattered by the lattice and have a reduced mean free path, with the result that the thermal conductivity is smaller in mixed crystals than in their components. Abrahams, Braunstein and Rosi²¹ found a pronounced minimum in the thermal conductivity of a 50% mole mixture of the InAs-GaAs system. The thermal conductivity of this mixture having a value of 0.012 cal.cm.⁻¹°K⁻¹ as opposed to 0.07 cal.cm. K for pure InAs and 0.09 cal.cm.⁻¹°K⁻¹ for pure GaAs. Since the alloying process results in a much greater reduction in thermal conductivity than in mobility, it is possible that suitably chosen alloys of the 3-5 compounds would have a sufficiently high thermoelectric figure of merit to be used as thermoelectric generators.

The InAs-InP system is more easily prepared than the previously mentioned mixed crystal systems and Oswald²² measured the energy gap optically. This was found to increase linearly from the InAs to the InP value and an equation relating the energy gap to the mixing ratio and the specimen temperature was obtained. For a given mixture the energy gap, Hall effect and electrical conductivity all show a similar temperature dependence to that of the 3-5 compounds. This alloy also has a pronounced minimum in its thermal conductivity for a 50% mole mixture. The mobility decreases sharply with increasing InP content up to 20 mole % where the value is half that of pure InAs, then decreases more slowly to that of pure InP.

When 3-5 compounds are formed, no matter how much one constituent is in excess of the other in the melt, a completely stoichiometric 3-5 crystal results with the excess constituent solidifying as a separate phase. If a stoichiometric sample is

desired care must be taken to cut away the excess phase.

Alternatively, if a two-phase sample is required the deliberately introduced excess phase is left in the sample which therefore constitutes a controlled eutectic solid.

1.2.6. Controlled Eutectic Systems.

By unidirectionally solidifying a eutectic mixture in much the same way as a metal is zone refined either parallel fibres of one phase in a matrix of the other result, or parallel alternating laminae of the two phases are formed. Generally the former configuration is expected if the volume fraction of one phase is much smaller than the other, and the latter if the volume fractions are nearly equal. Although other configurations are possible these two types usually prevail. In view of their microstructure, it is not surprising that such specimens should possess considerably greater crystallographic anisotropy than is possible in the simpler constituent phases.

To date, a comprehensive range of eutectic solids has been formed from widely differing substances, which have possible application as thermoelectric, magnetoresistive, optically polarising, superconducting or ferromagnetic materials.²³

In 1963, Liebmann and Millar²⁴ at R.C.A. laboratories began one of the earliest investigations into the thermoelectric behaviour of a controlled eutectic, using the InSb/Sb system. The microstructure consisted of triangular sectioned rods of Sb running parallel to the growth direction continuously through the InSb matrix. The phase diagram of this system records the ideal eutectic behaviour of complete miscibility of the components in the liquid state and negligible solubility in the solid state.

The crystallisation process, which is probably typical of this type of material is thought to proceed in the following manner.

When an InSb/Sb melt of eutectic composition is cooled below the eutectic point by a sharp temperature gradient, both phases start to crystallise simultaneously. During the process an undercooled liquid layer rich in Sb forms around every InSb crystallite and a similar layer rich in InSb forms around every Sb crystallite. If the excess Sb around the InSb crystallites can diffuse to the Sb crystallites, then a steady rate crystallisation can be maintained during which InSb and Sb crystallites of constant dimensions grow parallel to each other until the whole liquid is solidified.

The size of the rods formed was found to depend linearly upon the rate of solidification of the material. X-ray analysis revealed both the InSb matrix and the Sb rods to be single crystals, with their lattices orientated to produce minimal mismatch at the boundaries and a correspondingly highly stable structure.

The thermoelectric power in the growth direction compared with that perpendicular to the growth direction was cut by factor 4, while the electrical conductivity was increased by a factor 10 and the thermal conductivity was increased by a factor $4/3$. In addition, compared with pure InSb the electrical conductivity is greatly enhanced in the growth direction, while the thermal conductivity is reduced and the thermoelectric power is greatly reduced. The last factor proved to be the undoing of this substance for thermoelectric devices, as it resulted in a figure of merit lower than that of pure InSb.

Subsequent work to the same end was carried out by Galasso and Darby²³ on a $\text{Bi}_2\text{Te}_3/\text{Te}$ eutectic with a microstructure of irregular plates of Bi_2Te_3 orientated with the plate faces parallel to the growth direction in a Te matrix. Again, for the same reason,

however, Bi Te was shown to be a superior material.

At about the same time as Liebmann and Millar began their investigations, Wilhelm and Weiss²⁵ of Erlagen, West Germany, reported the information of a unidirectionally solidified eutectic system of InSb/NiSb which exhibited a twenty fold increase in resistance in a magnetic field of 10 kilogauss. A eutectic material of 1.8% NiSb and 98.2% InSb, by weight, containing needles of NiSb 1μ in diameter and of about 50μ length, randomly orientated was first produced. By zone melting such a system they were able to force an orientation of the NiSb needles along the temperature gradient.

Measurements by Wagini²⁶ on NiSb show that the electrical conductivity at room temperature is at least two orders of magnitude greater than that of InSb, so that the NiSb needles represent highly conducting inclusions within the InSb matrix.

A study of the physical properties and anisotropy of the InSb/NiSb eutectic forms the subject of this thesis. An examination of the microstructure of this material using stereoscan electron microscopy was carried out, together with experimental measurements on the Hall Effect, electrical conductivity, magnetoresistance, thermoelectric power and thermal conductivity. The corresponding experimental parameters have been deduced for the principal directions dictated by the microstructure, over a range of temperature and where appropriate, comparisons have been drawn with the behaviour of pure InSb.

CHAPTER 2

2.1. ELECTRICAL PROPERTIES OF EXTENDED SAMPLES.

2.1.1. Simple Hall Effect.

The Hall Effect was discovered in 1879 when E. H. Hall observed that a conductor carrying a current, I_x , in a transverse magnetic field, B_z , produced an electric field, E_y , in a mutually perpendicular direction.

This phenomenon can be explained in the following manner. A single charge $\pm e$, moving through an extended medium with velocity v_x in a magnetic field B_z , experiences a Lorentz force, F , given by

$$\underline{F} = (\pm e) (\underline{E} + \underline{v}_x \times \underline{B}_z) \quad (2.1)$$

This makes the charge follow a helical path limited only by the boundaries of the medium, at which the charges accumulate. Further accumulation is prevented when the electric field, \underline{E} , set up by these charges, reduces deflection force, \underline{F} , to zero, when

$$E_y = v_x B_z \quad (2.2)$$

Consequently an electric field must appear in the y-direction. If the medium contains N similar charges per unit volume the current density is $j_x = N(\pm e)v_x$ From (2).

$$E_y = \frac{j_x B_z}{N(\pm e)} \quad (2.3)$$

The Hall electric field, E , is then maintained as a result of charges leaving and arriving at the boundaries at the same rate.

From (3) it is clear that the electric field, E_y , is proportional to the current density, j_x , and the magnetic field, B_z . Consequently, a Hall coefficient, R_H , is defined where

$$R_H = \frac{E_y}{j_x B_z} = \frac{V_H d}{I_x B_z} = \frac{1}{N(\pm e)} \quad (2.4)$$

In equation (2.4) d is the thickness of the medium in the direction of the magnetic field and V_H is the Hall voltage.

Using (2.4) an experimental determination of the Hall coefficient, via the Hall voltage, is clearly possible, from which the concentration and sign of the carriers may be deduced.

2.1.2. Associated Effects.

Three other effects accompany the Hall Effect, namely the Ettinghausen Effect, the Nernst Effect and the Righi-Leduc Effect.

The Ettinghausen Effect owes its existence to the thermal distribution of velocities amongst the current carriers which has been neglected in the simple description of the Hall Effect. Close examination shows that the slower carriers are deflected more than the faster carriers, so that they are preferentially driven to the side of the specimen at which they accumulate to produce the Hall voltage. Therefore, the side which becomes electrically negative by means of the Hall voltage also becomes colder. The transverse temperature gradient activates a small transverse current flow, resulting in a transverse Ettinghausen voltage which provides a small increment to the Hall voltage.

The presence of a longitudinal temperature gradient causes a longitudinal flow of charge, which produces situations analogous to those described above. Providing the flow of charge is in the same direction as the electric current, the Nernst Effect, which is analogous to the Hall Effect, adds the related voltage to the Hall voltage. The spread of carrier velocities also provides a small transverse voltage in a similar way to the Ettinghausen Effect and this is called the Righi-Leduc Effect. Again, if the thermally activated flow of charge is in the same direction as the current, this voltage also adds to the Hall voltage.

2.1.3. Transverse Magnetoresistance.

Most materials increase their resistance if they are placed in a transverse magnetic field. If a given material

behaves in this way, it is said to possess a finite "transverse magnetoresistance".

Although the Hall and Nernst Effects may be crudely described without invoking a thermal distribution of carriers, such a procedure cannot account for the magnetoresistance observed in semiconductors having one type of carrier. In an extended sample of an extrinsic semiconductor, the force exerted by the magnetic field on a particular carrier depends solely on the carrier velocity. Since the charge carriers have a thermal distribution of velocities, some carriers are more strongly deflected than others by the magnetic field. The Hall field set up at the sample boundaries takes on an average value depending on the average velocity of the carriers. This causes a lateral drift of the charge carriers reducing their mobilities between the conductivity probes and consequently increasing the resistance. Theoretically, it may be shown that this increase in resistance is proportional to the square of the magnetic field, at low field values and approaches a limit independent of the magnetic field, at high field values.

In an intrinsic semiconductor, however, the Hall field cannot possibly restrain the lateral motions of both electrons and holes. This indicates that greater lateral drift of the dominant, higher mobility, carrier is possible than in the extrinsic case, so that a larger transverse magnetoresistance should be possible. This suggests that in order to theoretically account for the observed magnetoresistance of intrinsic semiconductors, an explanation based on averaging the thermal distribution of velocities of the dominant carrier over the energy states will be inadequate.

27

For the particular case of InSb Ehrenreich has shown that the carrier mobility of the dominant carriers, electrons, is determined at and above room temperature by polar scattering and

above 500°K by a combination of polar and electron hole scattering. When polar scattering dominates a relaxation time cannot adequately be defined which is valid near and above the optical mode temperature, 260°K . The electrical properties are later discussed after making the approximation that constant relaxation times exist above room temperature which are independent of the carrier energy for both electrons and holes, though the vulnerability of this assumption is acknowledged at very high temperatures, where $T \gg \Theta_L$.

Using this assumption Hilsum and Barrie²⁸ were able to give an impressive account of the room temperature magnetoresistances of eight samples of InSb of widely differing purities. For the present discussion of Hall effect, electrical conductivity and magnetoresistance of InSb/NiSb parameters will also be introduced again using constant energy-independent relaxation times.

2.1.4. Relaxation Time and Drift Mobility.

In order to describe the behaviour of electrons and holes in semiconductors in crossed electric and magnetic fields, it is necessary to assign a relaxation time to the carriers. This is the average time for which a given carrier can exist in free, unimpeded movement between collisions. In the absence of applied fields the carriers are supposed to move in random directions with a thermal distribution of velocities.

Let the probability of a single carrier suffering a collision in the small time interval dt be dt/τ where τ is assumed to be a constant, independent of the direction of motion of the carrier. The probability of an electron not colliding in this time interval is then $(1 - dt/\tau)$. Let $P(t)$ be the probability that t seconds after a collision has taken place, a further collision does not follow. Then

$$P(t + dt) = P(t) + \frac{dP(t)}{dt} \cdot dt \quad (2.5)$$

$$\text{and } P(t + dt) = P(t) P(dt) = P(t) (1 - dt/\tau) \quad (2.6)$$

From (2.5) and (2.6)

$$\begin{aligned} dP(t) &= -P(t).dt/\tau \\ \therefore P(t) &= \exp(-t/\tau) \end{aligned} \quad (2.7)$$

since $P(0) = 1$, for $t = 0$.

Therefore, the probability that the carrier shall be free for the time interval between t and $t + dt$ is given by

$$P(t) - P(t + dt) = - \frac{dP(t)}{dt} = \frac{1}{\tau} \exp(-t/\tau) dt$$

The average free time, or relaxation time of the carrier is given by averaging this probability over all collisions as below.

$$\langle \tau \rangle = \frac{1}{\tau} \int_0^{\infty} t \exp(-t/\tau) dt = \tau. \quad (2.9)$$

Clearly τ achieves significance as the relaxation time of the carriers.

If a system of such carriers is subjected to an impressed electric field, electrical conduction takes place. Further discussion of this process is made easier by considering a simple semiconductor possessing one type of carrier only, namely electrons. The electric field superimposes a small drift velocity on the random thermal motion of the carrier in the direction opposite to the field direction. This drift velocity increases with time until a collision process, governed by the relaxation time, τ , takes place. For isotropic scattering in which the electron has an equal probability of being scattered in any direction, when averaged over a large number of collisions, the drift velocity acquired from the electric field must be completely lost in the scattering process.

By Newton's Second Law, an electron of mass m^* in an electric field \underline{E} , acquires an acceleration $\dot{\underline{v}}$ given by

$$\dot{\underline{v}} = - \frac{|e| \hbar}{m^*} \underline{E}$$

$$\therefore \underline{v} = \underline{v} - \frac{e}{m^*} \underline{E}t, \quad \text{for } v = v_0 \text{ at } t = t_0.$$

Averaging over a large number of isotropic collisions

$\langle \underline{v} \rangle = 0$ and using (2.9)

$$\langle \underline{v} \rangle = - \frac{|e| \underline{E} \tau}{m^*} \quad (2.10)$$

The drift velocity $\langle \underline{v} \rangle$ is therefore directly related to the relaxation time.

If there are n electrons per unit volume the current density, j , that is the quantity of charge flowing across unit area perpendicular to the field is given by

$$j = - |e| n \langle \underline{v} \rangle$$

$$\therefore \langle j \rangle = \frac{n e^2 \tau \underline{E}}{m^*}$$

$$\text{or } \langle j \rangle = \sigma \underline{E} \quad (2.11)$$

Here σ is identified as the electrical conductivity of the semiconductor. The drift mobility, μ , of the electrons is defined as the velocity acquired by an electron in a unit electric field.

$$\therefore \mu = \frac{\langle \underline{v} \rangle}{\underline{E}} = \frac{|e| \tau}{m^*} \quad (2.12)$$

Comparison of the thermal velocity with the drift velocity acquired by an electron in germanium with an electric field of 10 V.cm^{-1} shows the drift velocity to be three orders of magnitude lower. In this case the mean free path may be shown to be of order several hundred lattice spacings.

Equations complementary to (2.10), (2.11) and (2.12) may be obtained for the drift velocity, electrical conductivity and drift mobility of the holes which are also present in an intrinsic semiconductor by changing the sign of the carriers and using a different relaxation time and effective mass.

Having stated this, the consequences of applying crossed electric and magnetic fields to a p-type semiconductor in which both

types of carrier exist simultaneously, will now be examined.

For this purpose the energy bands are taken to have a single minimum in the conduction band and a single maximum in the valence band, both located at the centre of the Brillouin zone and possessing spherical symmetry. Therefore, scalar effective masses m_e and m_p must be assigned to the electrons and holes respectively. The relaxation times for both electrons and holes are taken to be constant at τ_e and τ_p , respectively.

For a sample extended in the x-direction with a magnetic field $\underline{B} = B_z$ and an electric field $\underline{E} = (E_x, E_y)$ in which electrons travel with velocity $\underline{v}_e = (v_{ex}, v_{ey})$ and holes travel at velocity $\underline{v}_p = (v_{px}, v_{py})$ respectively, the equations of motion are

$$\dot{v}_{ex} = -\frac{e}{m_e} E_x - \omega_e v_{ey} \quad \dot{v}_{px} = \frac{e}{m_p} E_x + \omega_p v_{py}$$

$$\dot{v}_{ey} = -\frac{e}{m_e} E_y + \omega_e v_{ex} \quad \dot{v}_{py} = \frac{e}{m_p} E_y - \omega_p v_{px}$$

where $\omega_{e,p} = \frac{|e|B_z}{m_{e,p}}$ defines the cyclotron resonance frequencies of the electrons and holes.

Using the complex variable $Z_e = v_{ex} + i v_{ey}$, for the electronic equations in (2.13) the general solution governing the electronic motion is

$$Z_e = Z_{e0} + \frac{e}{m_e} (E_x + i E_y) (1 - \exp i \omega_e t)$$

where $Z_e = Z_{e0}$ when $t = 0$.

Averaging over all the collisions as in (2.9),

$$\begin{aligned} \langle Z_e \rangle &= 1/\tau_e \int_0^{\infty} Z_e \exp(-t/\tau_e) dt \\ &= -\frac{e}{m_e} (E_x + i E_y) \frac{\tau_e}{(1 + i \omega_e \tau_e)} \end{aligned}$$

since $\langle Z_{e0} \rangle$ must be zero in order to take into account the contributions due solely to the impressed fields.

Rationalising and separating into real and imaginary parts gives

$$v_{ex} = \frac{-e}{m_e} \left[\frac{\tau_e E_x}{1 + \omega_e^2 \tau_e^2} - \frac{\omega_e \tau_e^2 E_y}{1 + \omega_e^2 \tau_e^2} \right]$$

$$v_{ey} = \frac{-e}{m_e} \left[\frac{\tau_e E_y}{1 + \omega_e^2 \tau_e^2} + \frac{\omega_e \tau_e^2 E_x}{1 + \omega_e^2 \tau_e^2} \right]$$

Also, the current densities of the electrons are $J_{ex} = n(-e) v_{ex}$ and $J_{ey} = n(-e) v_{ey}$ in the x and y directions respectively, where n is the concentration of electrons, so that

$$J_{ex} = A_1 E_x - D_1 E_y \quad (2.14)$$

and $J_{ey} = A_1 E_y + D_1 E_x \quad (2.15)$

Where $A_1 = \frac{ne^2 \tau_e}{m (1 + \omega_e^2 \tau_e^2)}$, $D_1 = \frac{ne^2 \omega_e \tau_e^2}{m (1 + \omega_e^2 \tau_e^2)}$

Following identical procedures, the equivalent expressions for the positive holes are

$$J_{px} = A_2 E_x + D_2 E_y \quad (2.16)$$

and $J_{py} = A_2 E_y - D_2 E_x \quad (2.17)$

where $A_2 = \frac{pe^2 \tau_p}{m (1 + \omega_p^2 \tau_p^2)}$, $D_2 = \frac{pe^2 \omega_p \tau_p^2}{m (1 + \omega_p^2 \tau_p^2)}$

for a hole concentration p.

As $J_x = J_{ex} + J_{px}$ and $J_y = J_{ey} + J_{py}$, then

$$J_x = (A_1 + A_2) E_x + (D_2 - D_1) E_y \quad (2.18)$$

and $J_y = (A_1 + A_2) E_y - (D_2 - D_1) E_x. \quad (2.19)$

2.1.5. Electrical Conductivity.

The electrical conductivity, σ , in zero magnetic field may be obtained from (2.18). For this case,

$$\begin{aligned} J_x &= \frac{ne^2 \tau_e}{m_e} E + \frac{pe^2 \tau_p}{m_p} E \\ &= (ne\mu_e + pe\mu_p) E \quad \text{using (2.12)}. \end{aligned}$$

This equation then relates the electrical conductivity to the carrier concentrations and their mobilities, as

$$\frac{J_x}{E_x} = \sigma = ne\mu_e + pe\mu_p \quad (2.20)$$

This may be expressed in an alternative form by introducing the ratios $c = n/p$ and $b = \mu_e/\mu_p$. Substitution into (2.20) then gives

$$\sigma = pe\mu_p(1 + bc) \quad (2.21)$$

2.1.6. Hall Coefficient.

When mixed conduction is taking place in magnetic fields low enough for $\omega_{e,p}^2 \tau_{e,p}^2 = \mu_{e,p}^2 B_z^2 \ll 1$, the current densities become, using (2.18) and (2.19),

$$J_x = [ne\mu_e + pe\mu_p] E_x + [ne\mu_e^2 + pe\mu_p^2] \frac{B_z}{B_z} E_y \quad (2.22)$$

$$J_y = [ne\mu_e + pe\mu_p] E_y + [ne\mu_e^2 - pe\mu_p^2] \frac{B_z}{B_z} E_x \quad (2.23)$$

In the steady state $J_y = 0$,

$$\therefore E_x = - \frac{[ne\mu_e + pe\mu_p]}{[ne\mu_e^2 - pe\mu_p^2]} E_y$$

Substituting into (2.22), neglecting terms in B_z^2 and transposing in terms of the ratios b and c , gives

$$E_y = \frac{(1 - b^2c)}{pe(1 + bc)^2} J_x B_z \quad (2.24)$$

As the Hall coefficient, R_H , is defined by the equation

$$E_y = R_H J_x B_z$$

$$\therefore R_H = \frac{(1 - b^2c)}{pe(1 + bc)^2} \quad (2.25)$$

In order to derive a similar expression to (2.25) for the general case of an arbitrary magnetic field, a closer examination of the "low field" condition is necessary.

For fairly pure InSb, Steigmeier²⁹ has shown that in the mixed conduction range, the mobility falls from a room temperature value of order $800 \text{ cm}^2 \cdot \text{V}^{-1} \cdot \text{s}^{-1}$ as the temperature rises. Therefore, magnetic fields of more than 12 kG are necessary to invalidate the low field condition over this temperature range.

The value of the electronic mobility, over the same temperature range, never falls below a value of order $10,000 \text{ cm}^2 \cdot \text{V}^{-1} \cdot \text{s}^{-1}$ so that a 1 kG magnetic field is sufficient to break the low

field condition.

Bearing in mind that the present measurements were taken over a range of magnetic fields not exceeding 8 kG., a more general expression for the Hall coefficient was sought from (2.18) and (2.19). This expression showed that for an arbitrary magnetic field the R.H.S. of (2.25) must be modified by a factor

$$1 + \mu_e^2 B^2 / b^2 c^2$$

At room temperature in fairly pure material $c \doteq 1$, $b \doteq 90$ and $\mu_e \doteq 70,000 \text{ cm}^2 \text{ V}^{-1} \text{ s}^{-1}$, so that magnetic fields above 40 kG are necessary to render (2.25) noticeably inaccurate. As even greater magnetic fields are necessary to do this at higher temperatures, then (2.25) remains valid over the range of experimental measurement.

2.1.7. Acceptor Concentration and Hole Mobility.

In the extrinsic range, where electronic conduction may be neglected, $c \rightarrow 0$, so that from (2.25),

$$R_H = \frac{1}{pe} = \frac{1}{N_A e} \quad (2.26)$$

where N_A is the density of ionised acceptors.

Equations (2.18) and (2.19) again show that (2.26) remains true and that the Hall coefficient is invariant in a changing magnetic field. Therefore, the experimentally deduced Hall coefficient may be used to estimate the density of ionised acceptor impurities present, which enable extrinsic hole conduction to take place.

Other theoretical arguments, involving energy dependent relaxation times, suggest that a factor r should be included in the R.H.S. of (2.26), where r takes a value depending on the predominant scattering mechanism, i.e. 1.93 for ionised impurity scattering, 1.18 for non-degenerate acoustic scattering etc. However, in the

absence of direct experimental verification, the value of unity obtained for holes, in (2.26) and later, for electrons in (2.32), has been assumed for the present work.

Therefore, in the extrinsic range, combining (2.21) and (2.26),

$$R_H \sigma = \mu_p. \quad (2.27)$$

From equation (2.27) it is clear that, from an experimental measurement of the Hall coefficient and the electrical conductivity at low temperatures, a direct estimate of the hole mobility may be made.

2.1.8. Electron Concentration and Electron Mobility.

At higher temperatures where mixed conduction is taking place, the concentrations of electrons and holes are linked to the concentration of intrinsic carriers, n_i by the relation

$$np = n_i^2 \quad (2.28)$$

In (2.28) $p = n + N_A$, where all acceptors are assumed to be ionised.

$$\begin{aligned} \therefore p^2 c &= n_i^2 \\ \text{or } p &= n_i / \sqrt{c}. \end{aligned} \quad (2.29)$$

Substitution in (2.21) and (2.25) gives

$$R_H = \frac{(1 - b^2 c) \sqrt{c}}{n_i e (1 + bc)} \quad (2.30)$$

$$\sigma = n_i e \mu_e \frac{(1 + bc)}{b \sqrt{c}} \quad (2.31)$$

Since the mobility ratio in InSb is very large in the mixed conduction range when $c \rightarrow 1$ equation (2.30) reduces to

$$R_H = - \frac{1}{n_i \sqrt{c} e} = - \frac{1}{ne} \quad (2.32)$$

Under these conditions the number of conduction electrons may be estimated from a direct experimental measurement of the Hall coefficient. If the concentration of extrinsic carriers is also known, the concentration of intrinsic carriers may be calculated using (2.28).

$$\text{Also, from (2.31), } \sigma = n e \mu_e \sqrt{c} = n e \mu_e. \quad (2.33)$$

Evidently under these conditions the hole contribution to the electrical conductivity may be neglected. Further, from (2.32) and (2.33),

$$R_H \sigma = \mu_e \quad (2.34)$$

The mobility of the electrons may therefore be deduced from a measurement of the Hall coefficient and the electrical conductivity.

2.1.9. The Hall Angle.

By setting $J_y = 0$ in (2.19), clearly,

$$(A_1 + A_2) E_y = (D_2 - D_1) E_x$$

The Hall angle, θ , gives the inclination between the resultant electric field and the resultant current density, within the semiconductor as below

$$\tan \theta = \frac{E_y}{E_x} = \frac{D_2 - D_1}{A_1 + A_2} \quad (2.35)$$

$$= \mu_p B_z \frac{1 + \mu_e^2 B_z^2 - cb^2}{1 + bc + \mu_e^2 B_z^2} \quad (2.36)$$

In the extrinsic range, $c \rightarrow 0$, $\theta = \theta_p$ and

$$\tan \theta_p = \mu_p B_z \quad (2.37)$$

For InSb in the intrinsic range $cb^2 \gg \mu_e^2 B_z^2, 1$, for $B < 14$ Kg. and as $bc \gg 1$, to a one per cent approximation for mixed conduction where

$$\tan \theta_m \doteq - \frac{\mu_e^2 B_z^2}{[1 + \mu_e^2 B_z^2 / bc]} \quad (2.38)$$

By inserting the appropriate parameters into (2.37) and (2.38) the Hall angles may be calculated in the extrinsic and intrinsic ranges, respectively.

2.1.10. Transverse Magnetoresistance.

By setting $J_y = 0$ in (2.19), E_y may be obtained in terms of E_x . Substitution for E_y in (2.18) then gives

$$J_x = (A_1 + A_2) E_x + \frac{(D_2 - D_1)^2}{(A_1 + A_2)} E_x$$

Following the previous approximation methods the value of the electrical conductivity, σ_3 , in terms of the magnetic field B_z is given by

$$\frac{J_x}{E_x} = \sigma_3 = \frac{ne\mu_e}{1 + \mu_e^2 B_z^2 / bc} \quad (2.39)$$

Using (2.34),

$$\sigma_3 = \frac{\sigma}{1 + \mu_e^2 B_z^2 / bc} \quad (2.40)$$

$$\therefore \frac{\sigma}{\sigma_3} = \frac{\rho_3}{\rho} = r_m = 1 + \mu_e^2 B_z^2 / bc$$

Equation (2.41) gives the ratio of the resistivities ρ_3 and ρ , or transverse magnetoresistance, r_m , in the form used by Hilsum and Barrie. Insertion of the parameters μ_e , b and c then enables the magnetoresistance to be calculated for various values of the applied field.

2.2. ELECTRICAL PROPERTIES OF NON-EXTENDED SAMPLES.

2.2.1. Geometrical Effects.

The Hall effect, electrical conductivity and magneto-resistance of a material are all defined in terms of continuous, infinitely extended samples. Therefore, if the experimental parameters derived from these effects are to be a true reflection of the nature of the material, a homogeneous sample should be chosen with dimensions which approximate effectively to the infinitely extended case.

30

Isenberg, Russell and Green considered the case of a rectangular sample provided with large area current contacts, which had a high conductivity and a Hall coefficient negligible compared with that of the sample. It was shown that accurate experimental determination of the Hall coefficient, by means of centrally placed Hall probes, is only possible for a sample of aspect ratio $l/\omega \gg 4$ where l is the sample length and ω is its width. If, however, $l/\omega < 4$ the full value of the Hall coefficient is not obtained, as some of the Hall voltage is shorted out by the current contacts.

31

Volger generalised this approach and showed that a diminished Hall coefficient is also obtained as the position of the Hall probes is varied in such a sample.

32

Wick concluded that the shorting out of the Hall voltage caused an increase in resistance between the end contacts of a rectangular specimen. This "Hall resistance" behaves very much like the transverse magnetoresistance described in 2.1.3. and 2.1.10, in that the increase in resistance is proportional to the square of the magnetic field, for low magnetic fields, but differs from it by tending to direct proportionality at high magnetic fields.

As explained in 2.1.3. transverse magnetoresistance arises through processes which allow carriers to drift laterally, giving

a reduced carrier mobility, and increased resistivity, measured between the conductivity probes. The magnitude of the transverse magnetoresistance would be expected to be small compared with the increases in resistance that are made possible by reducing l/w since, by shorting out the Hall field, greatly enhanced lateral drift becomes possible.

As l/w is decreased the shorting out of the Hall field results in an increased sample resistance, approaching a limit as l/w approaches zero. Clearly, this limit cannot be attained experimentally by using a rectangular sample. However, l/w may be made to approach zero through the minimisation of the Hall field achieved by using a Corbino disc shaped sample, with current electrodes at the centre and circumference.

The general conclusions drawn above on the influences of sample geometry on sample resistance are strongly supported by experimental evidence.

³³
Hilsum and Barrie measured the relative resistances of a Corbino disc and a long, narrow sample, both taken from the same ingot of InSb, with an electron mobility of $76,000 \text{ cm}^2 \text{ V}^{-1} \text{ s}^{-1}$. In a magnetic field of 10 kG., the Corbino disc increased its resistance by a factor 33, while the long, narrow sample increased its resistance by a factor 1.57.

For samples of InSb of a shape intermediate between these two extremes of geometry, Willardson and Beer ³⁴ found that for a given magnetic field the relative increases in resistance became larger as was reduced.

³⁵
Further support was furnished by Welker and Weiss, who made measurements on four different shaped samples of InSb of the same purity and having an electron mobility of $43,000 \text{ cm}^2 \text{ V}^{-1} \text{ s}^{-1}$. The chosen sample shapes were a Corbino disc, two samples of aspect

ratio 0.5 and 1.0 and a long, narrow sample. In a magnetic field of 10 kG., these samples taken in the above order, increased their resistances by factors 18, 11, 5.5 and 2 respectively.

Generally, apart from the cases of Corbino discs, and long, narrow samples, which fulfil the "extended sample" requirement, no attempt has been made, in these papers, to account for the relative resistance values obtainable from a sample of arbitrary aspect ratio.

36

In order to rectify this situation C. A. Simmons conducted an investigation on InSb, of mobility $77,400 \text{ cm}^2 \text{ V}^{-1} \text{ s}^{-1}$, aimed at identifying the relative parts played by the geometry and by the actual nature of the sample material.

Using a specially designed sample holder consisting of two transverse probes, the transverse voltage was measured at various points along the sample. By taking one large area current contact as the zero of potential and moving the probes along the sample, a potential profile could be plotted. The resistivity, ρ , was obtained by plotting such a profile in the absence of a magnetic field and measuring the sample current. By following a similar procedure in the presence of a magnetic field, the Hall voltage and the total resistance between the current contacts were deduced. The potential difference between the end contacts gave the total change in resistivity due to the magnetic field, B_z , which may be written in the form $(\Delta\rho_s/\rho)_T$. This clearly includes a contribution due to the physical nature of the sample and a geometrical contribution. After some manipulation Simmons concluded that

$$(\Delta\rho_s/\rho)_T = (\Delta\rho_s/\rho) + (\Delta\rho_s/\rho)_g$$

Here the subscript p refers to the "physical" contribution due to the nature of the sample, which was measured using an extended sample and may be identified with the transverse magneto-

resistance, while the subscript g refers to the geometrical contribution.

By plotting $(\Delta\rho_B/\rho)$ against l/ω , the above formula was shown to hold for a series of samples in the range $0.35 \leq l/\omega \leq 12$. For $B = 10\text{kG.}$, it was also shown that in the upper limit of l/ω , a value $(\Delta\rho_B/\rho) = 0.49$, emerged, while in the lower limit as $(\Delta\rho_B/\rho)_{\frac{1}{T}} = 13$ the geometrical contribution clearly dominates.

A further advance was made by Lippmann and Kuhrt³⁷ who were able to directly relate the sample geometry to the geometrical contribution which it produced. Their analysis, based on the invariance of the Hall angle with sample geometry, enabled the relative resistance observed in magnetic field to be split into two terms. A physical magnetoresistance term, r_{∞} , arises from the way in which the applied magnetic field prevents the charge carriers from travelling at their full drift velocity which is characteristic of their average behaviour between two collisions in the absence of a magnetic field. This reduced drift mobility decreases the specific conductivity, σ , measured on an extended sample, to a value, σ_B , in a magnetic field B_2 , so that

$$r = \frac{H}{g_B} \quad (2.42)$$

The other term is the geometrical resistance term, r_g , arising from the deflection of the current streamlines. This means that the current no longer passes through the conductor by the shortest path from one electrode to the other, but experiences an amount of lateral drift depending on the shape of the sample.

The geometrical contributions for different values of l/ω have been obtained in terms of the Hall angle. In their formulations Lippmann and Kuhrt assumed that only one type of carrier was present undergoing acoustic scattering. For the case of a constant

relaxation time and mixed conduction these formulations reduce to the equations below.

For small Hall angles, $0 \leq \tan \theta_m \leq 0.45$, where $\tan \theta_m$ is given by (2.38)

$$r_g = 1 + (8/3\pi)^2 \theta_m^2 g(\ell/\omega) \quad (2.43)$$

In (2.43), $g(\ell/\omega)$ is a function which reduces from 1, at $\ell/\omega = 0$, to values which asymptotically approach zero as ℓ/ω approaches infinity. The former clearly refers to a Corbino disc sample, while the latter refers to an extended sample.

For large Hall angles, $\theta_m \approx \pi/2$ and

$$r = 1 + (\omega/\ell) \left[(8/3\pi) \tan \theta_m - (4/\pi) \ln 2 \right] \quad (2.44)$$

In the intermediate range of Hall angles, the values of r_g , obtained for various specific values of ℓ/ω , are plotted as a function of the tangent of the Hall angle, as shown in Fig.5.

The total resistance of the sample, r , is then given by the product of the magnetoresistive term and the geometrical term, i.e.

$$r = r_\infty r_g$$

Experimental evidence shows that for InSb in the mixed conduction range, the geometrical term may be ignored provided $\ell/\omega \gg 5$. Therefore, providing a sample geometry consistent with this requirement is used, r_∞ and r_m become identical and

$$r = r_m r_g \quad (2.45)$$

where r is given by (2.41).

38

In a further paper, the same authors used identical techniques to explain the dependence of the experimentally observed Hall coefficients on the sample geometry chosen. Again a resultant Hall coefficient, R_H^x occurs as the product of two terms, which reduce to

$$R_H^x = R_H G(\ell/\omega, \theta_m) \quad (2.46)$$

for a mixed conductor.

In equation (2.46) R_H is the Hall coefficient observed

Fig. 5

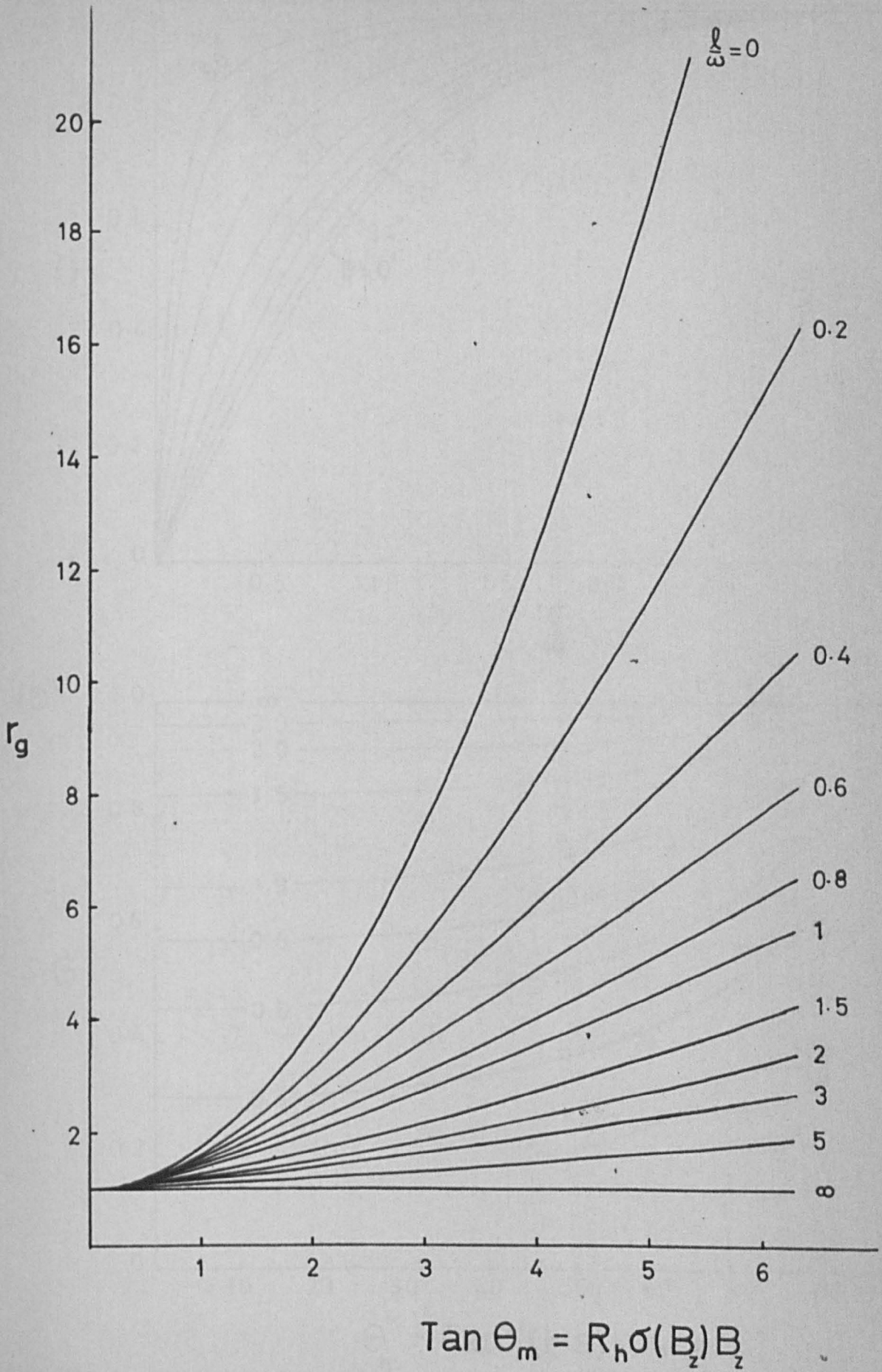
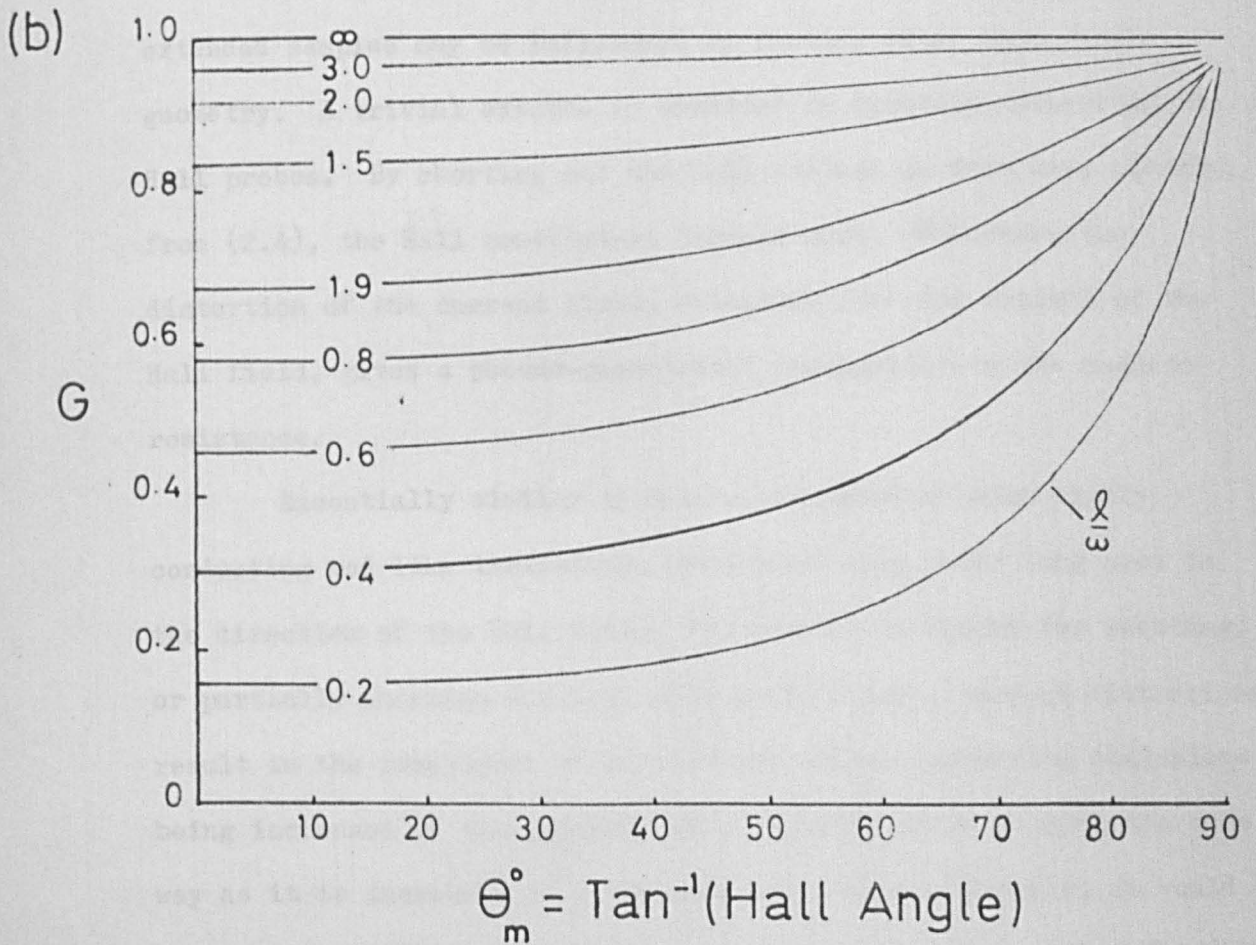
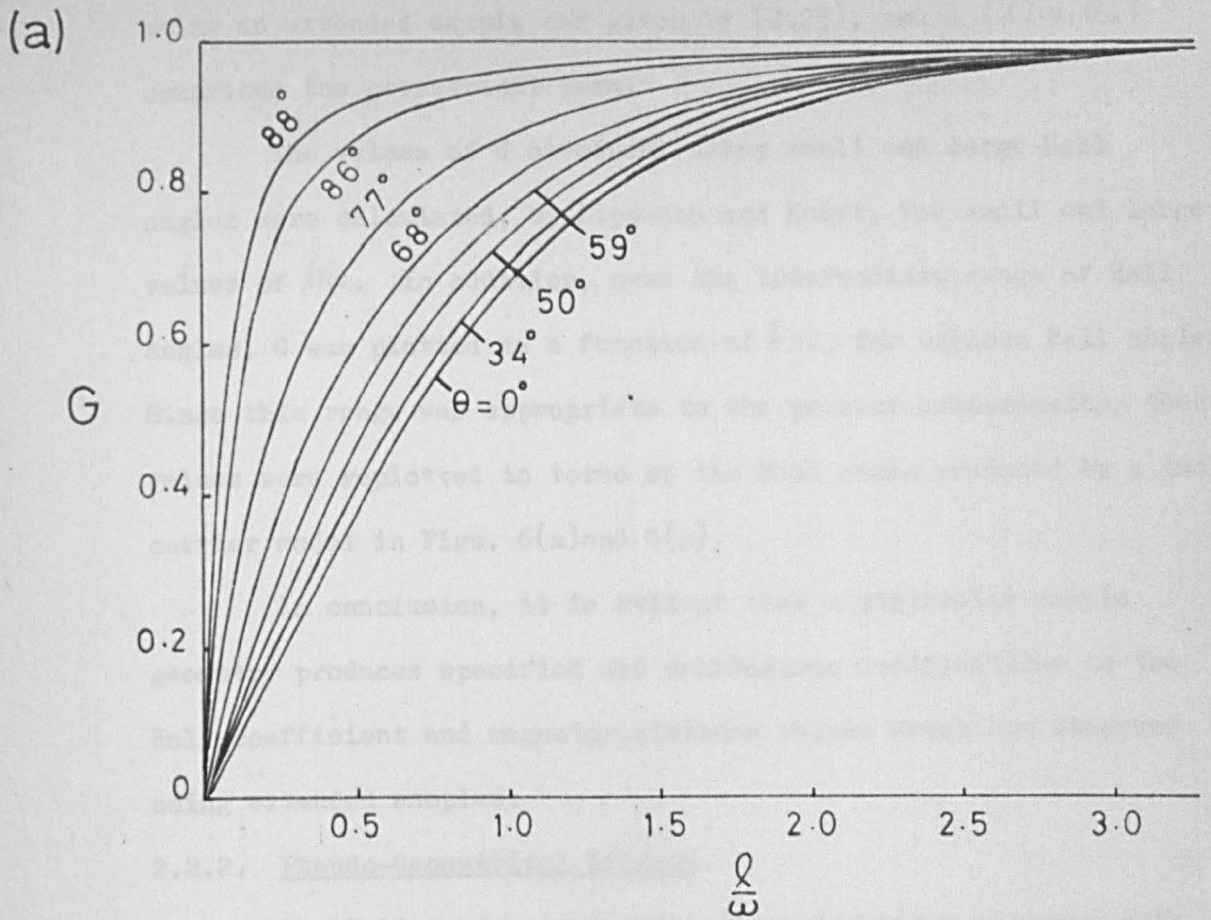


Fig.6



using an extended sample and given by (2.25), and $G(\ell/\omega, \theta_m)$ comprises the geometrical term.

The values of G obtained, using small and large Hall angles were calculated, by Lippmann and Kuhrt, for small and large values of ℓ/ω . In addition, over the intermediate range of Hall angles, G was plotted as a function of ℓ/ω , for various Hall angles. Since this range was appropriate to the present measurements, these values were replotted in terms of the Hall angle produced by a two carrier model in Figs. 6(a) and 6(b).

In conclusion, it is evident that a particular sample geometry produces specified and unambiguous modifications to the Hall coefficient and magnetoresistance values which are observed using extended samples.

2.2.2. Pseudo-Geometrical Effects.

The Hall coefficient and magnetoresistance observed with extended samples may be influenced by factors other than sample geometry. A trivial example is provided by directly connecting the Hall probes. By shorting out the Hall voltage in this way, clearly, from (2.4), the Hall coefficient becomes zero. Moreover, the distortion of the current lines, resulting from the removal of the Hall field, gives a pseudo-geometrical enhancement to the magnetoresistance.

Essentially similar processes are involved when highly conducting rod like inclusions, orientated with their long axes in the direction of the Hall field, are used as an agency for shorting, or partially shorting the Hall voltage. Therefore, current distortions result in the resistance of an extended sample containing inclusions being increased in the presence of a magnetic field in much the same way as it is increased in a non-extended sample. Further, it would be expected that if the Hall voltages in both these cases are reduced by

the same ratio, then similar increases in resistance would result.

This forms a basis whereby the behaviour of the InSb/NiSb eutectic may be represented as a series of similar rectangular elements of InSb separated by thin, large area, electrode-like layers of NiSb. By determining the Hall angle in each InSb element of the above model and the ratio of the Hall coefficient of InSb/NiSb to that of pure InSb, the appropriate "geometry" may be assigned to the element in accordance with (2.46) and by inspection of Fig.6(b). Then, using the Hall angle and the elementary "geometry" of the InSb, the corresponding "geometrical" resistance may be estimated using Fig.5.

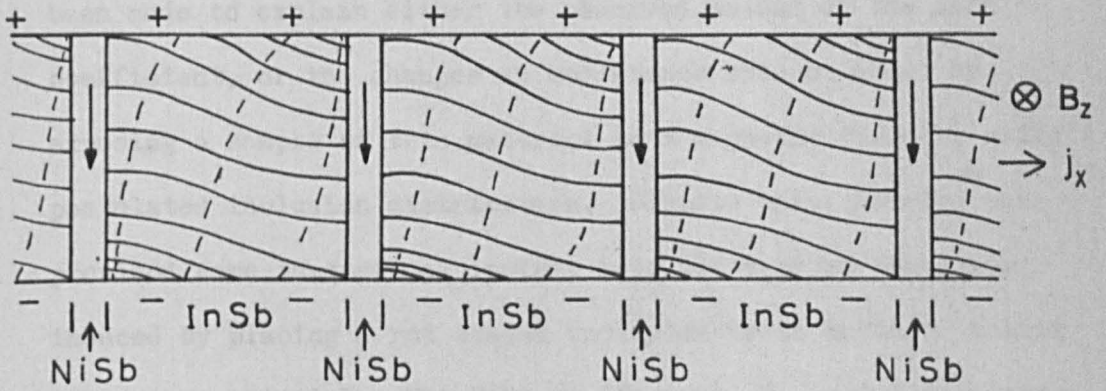
A regular composite sample, as described above, must be constructed from thin layers of NiSb and thick layers of InSb, since the volume fraction of NiSb is small in the InSb/NiSb eutectic. In each similar layer the Hall coefficient, resistivity and current flow follows a similar pattern.

The current component, j_x , must be the same in each layer and since the Hall coefficient changes in successive layers, j_x gives rise to a Hall contribution to E_y which changes from one layer to the next and is proportional to B_z .

As $\nabla \times \underline{E} = 0$, the total E_y must be the same in each layer and ohmic contributions to E_y must arise from the y-components of \underline{j} and these must be proportional to B_z . Thus, as $B_z \rightarrow \infty$ the current lines must distort as shown in Fig.7. This means that the current lines flow in such a way as to reduce the tangential component, E_y , on the InSb side of the boundary to the much lower value on the NiSb side. This distortion entails a resistive dissipation which, for given j_x , increases without limit as $B_z \rightarrow \infty$. The patterns of current flow are then repeated in each elementary pair of InSb and NiSb layers throughout the sample, so that the "geometry" and the resistive

Fig. 7

COMPOSITE MODEL FOR InSb/NiSb



- LINES OF CURRENT FLOW .IN InSb
- DIRECTION OF SHORTING CURRENT IN NiSb
- EQUIPOTENTIAL LINES

dissipation of each InSb layer are characteristic of the whole composite sample.

2.2.3. Isolated Inclusions.

The InSb/NiSb eutectic mixture is composed of small, unidirectionally orientated, rod shaped inclusions of NiSb dispersed throughout an InSb matrix. No successful attempt has been made to explain either the observed values of the Hall coefficient, or the changes in resistance brought about by exposing a sample of this material to a magnetic field by using a postulated inclusion distribution. Despite this, Herring has³⁹ provided some theoretical insight into the type of behaviour induced by placing a rod shaped inclusion in an infinite matrix of another material. The Hall coefficient, R_H , and resistivity, ρ , were taken to approach constant limits as $B \rightarrow \infty$, the limiting Hall coefficient of the rod differing that of the surrounding material. For an inclusion with its long axis lying in the direction of the magnetic field and considering the current flow perpendicular to this axis, then

$$E_t = R_H B j_n + \rho j_t \quad (2.47)$$

In (2.47) the subscripts t and n refer to the directions tangential and normal to the inclusion rod boundary. Since R_H is discontinuous across the boundary, while E_t and j_n must be continuous, then as $B \rightarrow \infty$, $j_n \rightarrow 0$. This means that the current lines, flowing in a direction transverse to the rod axis, in the limit avoid the rod as if it were an insulator. The current⁴⁰ distortion may, in fact, be many times the diameter of the inclusion, with the associated resistive dissipation involved, increasing the sample resistance. As the magnetic field is increased from zero the sample resistance approaches a finite limit depending on the extent to which the current lines are

squeezed in their avoidance of the rod. It follows that in a sample containing a dilution of inclusions the Hall coefficient would be reduced and the sample resistance would be increased, as the volume fraction of inclusions or the magnetic field are increased.

2.3. THERMOELECTRIC POWER.

Consider a circuit made up of elements AB, BC and CA', where AB and CA' are both constructed of the same homogeneous material 2, while BC is constructed from another homogeneous material 1. Maintaining the junctions B and C at constant temperatures T_1 and T_2 respectively, where $T_2 > T_1$, and the terminals A and A' at a temperature T_3 , results in the generation of a steady e.m.f. of a magnitude which can be measured by connecting a potentiometer across AA'.

Experience has shown that the measured e.m.f. depends on the particular materials chosen and the difference in the junction temperatures. By convention, the measured thermo-e.m.f., V_{12} , is regarded as positive when the terminal which is connected to the low temperature junction, B, becomes positive. The thermoelectric power of material 1 with respect to material 2 is defined as the thermo-e.m.f. obtained for unit temperature difference between the junctions, i.e.

$$\alpha_{12} = \lim_{\Delta T \rightarrow 0} \frac{V_{12}}{\Delta T} \quad (2.48)$$

where $\Delta T = T_2 - T_1$.

By using the "Thompson Relations" it is possible to separate the contributions of the two materials to the thermoelectric power. The absolute thermoelectric powers α_1 and α_2 due to the materials 1 and 2 respectively, may then be shown to be linked to in the form

$$\alpha_{12} = \alpha_1 - \alpha_2. \quad (2.49)$$

The absolute value of the thermoelectric power for metals is generally a few microvolts per unit temperature difference and this is usually at least one order of magnitude less than that of semiconductors.

Therefore, in such a semiconductor (1) - metal (2) system,

$\alpha_{1,2} = \alpha_1 = \alpha$ to a good degree of approximation and a measurement yields effectively the absolute thermoelectric power of the semiconductor.

For an intrinsic semiconductor the absolute thermoelectric power, α , is given by

$$\alpha = \frac{k}{e} \left[\frac{\sigma_n}{\sigma} \cdot \frac{\zeta_n - Q_n^*}{kT} - \frac{\sigma_p}{\sigma} \cdot \frac{\zeta_p - Q_p^*}{kT} \right] \quad (2.50)$$

In (2.50) k is Boltzmann's constant and e is the electronic charge giving $k/e = 86.3 \mu\text{V}^\circ\text{K}^{-1}$; σ_n and σ_p are the electron and hole contributions of the electrical conductivity, σ , while ζ_n and ζ_p are the fermi levels and Q_n^* and Q_p^* are the kinetic energies transported by the electrons and holes respectively at temperature T . Equation (2.50) clearly indicates that the thermoelectric power is made up of an electron contribution and a hole contribution. From the orders of magnitude involved it is evident that the thermoelectric power is negative in n-type and positive in p-type semiconductors. In the intrinsic range the sign is governed by the carrier with the higher mobility. The large mobility ratio of InSb ensures that $\sigma_n/\sigma \doteq 1$ and $\sigma_p/\sigma \doteq 10^{-2}$, so that, to a good approximation, the hole mobility may be neglected.

$$\therefore \alpha = \frac{k}{e} \left[\eta^* - \frac{Q_n^*}{kT} \right] \quad (2.51)$$

In (2.51), $\eta^* = \zeta_n/kT$, the reduced Fermi level of the electrons. The value of Q_n^*/kT depends on the scattering mechanisms present, the shape of the energy bands and the degeneracy. If a degree of degeneracy is present the value of this parameter increases with temperature under any scattering indicating that a larger fraction of the current is carried by more energetic electrons as the temperature rises.

For a specimen having parabolic energy bands and undergoing

thermal acoustic scattering

$$\frac{Q_n^*}{kT} = \frac{2F_1(\eta^*)}{F_0(\eta^*)} \quad (2.52)$$

where F_1 and F_0 are Fermi integrals of order 1 and 0. The value of these integrals may be found from the Fermi integral of order m , where

$$F_m(\eta^*) = \int_0^\infty \frac{\eta^m d\eta}{1 + \exp(\eta - \eta^*)}$$

and $\eta = E/kT$.

Substituting from (2.52) in (2.51) gives for the intrinsic range

$$\left| \frac{\alpha}{86.3} \right| = 2 \frac{F_1(\eta^*)}{F_0(\eta^*)} - \eta^*$$

Therefore a plot of $2F_1(\eta^*)/F_0(\eta^*)$ against η^* allows the reduced Fermi level η^* to be determined from the experimental values of $|\alpha/86.3|$.

For a semiconductor with parabolic energy bands the reduced Fermi level is linked to the intrinsic carrier concentration by the formula

$$n_i = n = N_c \frac{2}{\sqrt{\pi}} F_{\frac{1}{2}}(\eta^*) \quad (2.53)$$

where $N_c = 2(2\pi m_{nd} kT/h^2)$ and represents the effective number of states in the conduction band and m_{nd} is the "density of states" effective mass, averaged over all occupied energy states, of the electrons. The values of the Fermi integral of order $\frac{1}{2}$ have been tabulated by McDougall and Stoner,⁴¹ while those of order 1 and 0 have been tabulated by Wright and Madelung⁴² respectively.⁴³

Using the reduced Fermi levels and the electron concentrations obtained at various temperatures from thermoelectric power and Hall measurements respectively, values of m_{nd} may be calculated over a temperature range.

2.4. THERMAL CONDUCTIVITY.

The application of a temperature differential, along a solid of length, Δx (cm) and cross sectional area A (cm²) promotes a flow of thermal energy, H (cal.sec⁻¹), down the temperature gradient. The relationship between these quantities may be expressed in the form

$$H = KA \frac{\Delta T}{\Delta x} \quad \text{cal.sec}^{-1} \quad (2.54)$$

$$\text{or} \quad K = \frac{H}{A \frac{\Delta T}{\Delta x}} \quad \text{cal.sec}^{-1} \text{cm}^{-1} \text{K}^{-1} \quad (2.55)$$

where K is called the thermal conductivity of the solid.

The thermal energy may be transferred through vibrations of the crystal lattice, or by the free charges it contains, or by a combination of these two mechanisms.

In an insulator, since the number of free carriers is extremely small, heat is conducted through the solid almost entirely by the vibrations of the lattice atoms. Conversely, in a metal the quantity of heat transported by the high concentration of free electrons present dwarfs the lattice contribution. In semiconductors, however, although more heat is generally transferred by the lattice, the contribution due to free carriers may be considerable. The free carriers, electrons and holes, may transport their kinetic energies directly by diffusing down the temperature gradient. During this process there is also a possibility that electrons and holes may recombine and give up their potential energies to the lattice, in the procedure known as ambipolar diffusion. A further mechanism of heat conduction by weakly bound electron-hole pairs, which remain associated so that they can carry energy but no charge, has also been suggested. This process is known as exciton-transport but its quantitative

importance has not yet been experimentally established.

The total thermal conductivity, K , of a semiconductor may, therefore, be expressed as the sum of a "lattice" component, K_L and a "charge carrier" or "electronic" component, K_e , so that

$$K = K_L + K_e \quad (2.56)$$

The relative magnitudes of the two components depends on the temperature and the purity of the sample. For a semiconductor of high purity and crystalline perfection the electronic contribution may be appreciable in the intrinsic range but negligible in the extrinsic range. In a doped semiconductor, however, the carrier concentration may be enhanced to such a degree that the electronic contribution is appreciable at all temperatures.

2.4.1. The Lattice Component.

In the presence of an applied temperature gradient the phonon distribution in each mode of vibration is different to that existing in thermal equilibrium, as described by (1.2).

⁴⁴ Peierls concluded that phonon-phonon collisions tend to restore thermal equilibrium, the rate of the restoring process determining the thermal resistance.

Selection rules govern the collision processes that are possible between phonons, allowing them to be classified as "Normal" and "Umklapp" processes. In both types of process the total energy is unchanged throughout the collision process. For Normal processes the total momentum is also unchanged, so that they do not contribute to the thermal resistance. For Umklapp processes the total momentum changes, so that the energy flow changes its direction on collision. The Umklapp processes are, therefore, responsible for the thermal resistance in Peierl's theory.

Since the scattering is approximately random, drawing from the analogous collisions between gas molecules, thermal conductivity may be described by the relation

$$K = \frac{1}{3} C U \lambda_p \quad (2.57)$$

where C is the specific heat of the phonon gas, U is the velocity of sound in the lattice and λ_p is the phonon mean free path.

The phonon mean free path may be limited by phonon-phonon interactions, scattering by lattice imperfections and boundary scattering. Peierls suggested that above the Debye temperature, the phonon mean free path is limited by interactions involving three phonons. In these, a single phonon may split up into two, or two phonons may combine to form a third. Such interactions lead to a thermal conductivity that is inversely proportional to the absolute temperature.

⁴⁵ Pomeranchuk postulated that interactions also occur where one, two, or three phonons produce three, two, or one phonon respectively, leading to a thermal conductivity that is inversely proportional to the square of the absolute temperature.

Above the Debye temperature but below the onset of intrinsic conduction ⁴⁶Abeles, ⁴⁷Stuckes and ⁴⁸Danielson found that $K_L \propto T^{-1}$ for Ge and Si, confirming the predominance of three phonon processes, as predicted by Peierls. At higher temperatures the thermal conductivity was found to have a more rapid temperature variation by Stuckes, who suggested that four phonon processes, with their associated $K \propto T^{-2}$ dependence, were also present in an admixture of three and four phonon processes. This was later confirmed by Slack and Glassbrenner ⁴⁹who invoked both three and four phonon processes in accounting for their experimental results.

The presence of impurities and lattice imperfections in a semiconductor tends to reduce the lattice thermal conductivity

since the variation in density and elastic forces produced by them may scatter phonons. Peierls qualitatively concluded that the additional thermal resistance produced in this way should be independent of temperature. At higher temperatures this increase in resistance should be small, particularly in fairly pure materials where the separations of such scattering agencies becomes large compared with the mean free path of phonon-phonon processes.

The scarcity of phonons brought about by lowering the temperature results in an increase in the mean free path, which, according to Peierls, should lead to an exponential increase in the thermal conductivity, tending to infinity at absolute zero. It was shown by Casimir,⁵⁰ however, that at very low temperatures phonons are scattered by the sample boundaries and that this mechanism predominates as the temperature approaches absolute zero. Under these conditions the thermal conductivity is controlled by the specific heat of the sample and is, therefore, proportional to the cube of the absolute temperature, tending to zero at absolute zero. This type of variation has been observed by White and Woods⁵¹ and Curruthers et al⁵² in Ge and Si establishing the importance of boundary scattering at very low temperatures.

2.4.2. The Electronic Component.

By solving the Boltzmann equation under the assumptions that no current flows in the semiconductor and that isotropic scattering processes occur,⁵³ Madelung deduced a general expression for the electronic component of the thermal conductivity.

By postulating a relaxation time $\tau_{n,p}$ for electron and holes of the form

$$\tau_{n,p} = a T^{-1} E_{n,p}^{q/2} = a' T^{(q-2)/2} \eta_{n,p}^{q/2} \quad (2.57)$$

where a and a' are constants, T is the absolute temperature,

$\eta_{n,p} = E_{n,p}/kT$ and q depends on the scattering mechanism of the

carriers, Madelung's expression reduces to

$$K_e = \frac{k^2}{e^2} \sigma T \left[A_n \frac{\sigma_n}{\sigma} + A_p \frac{\sigma_p}{\sigma} + \frac{\sigma_n \sigma_p}{\sigma^2} \left(\frac{E_g}{kT} + B_n + B_p \right)^2 \right] \quad (2.58)$$

Where $E_g = 0.26 - 2.7 \times 10^{-4} T$ eV, and $A_{n,p}$ and $B_{n,p}$ are given by

$$A_{n,p} = \frac{7+q}{3+q} \cdot \frac{F_{(5+q)/2}(\eta^*)}{F_{(1+q)/2}(\eta^*)} - \left[\frac{5+q}{3+q} \cdot \frac{F_{(3+q)/2}(\eta^*)}{F_{(1+q)/2}(\eta^*)} \right]^2$$

and

$$B_{n,p} = \frac{5+q}{3+q} \cdot \frac{F_{(3+q)/2}(\eta^*)}{F_{(1+q)/2}(\eta^*)}$$

Also $q = q_{n,p}$, $\eta^* = \xi_{n,p}/kT$, $\xi_n = \xi - E_L$ and $\xi_p = E_V - \xi$, where ξ is the Fermi level and E_L , E_V define the bottom of the conduction band and top of the valence band, respectively.

In order to determine the Lorentz factors $A_{n,p}$ and $B_{n,p}$ the temperature variation of the mobility must be examined. By averaging the relaxation time over the carrier energies, the mobility $\mu_{n,p}$ may be written,

$$\mu_{n,p} = \frac{a'}{m_{n,p}} \cdot \frac{q+3}{3} \cdot T^{(q-2)/2} \cdot \frac{F_{(q+1)/2}(\eta^*)}{F_{1/2}(\eta^*)} = \text{const.} T^\gamma \quad (2.59)$$

At a given temperature the values of the scattering index, q and the reduced Fermi level η^* are constants.

Under the assumed conditions of parabolic bands, the effective mass $m_{n,p}$ and the reduced Fermi level η^* vary with temperature. Therefore, for a given value of q the temperature dependence of the mobility can only be predicted if the temperature variation of effective mass and Fermi level are known. For this purpose the information furnished by the thermoelectric power data discussed in section 2.3 may be used.

Inserting the appropriate temperature dependences in (2.59) enables a single value of γ to be obtained for a given value of q . By drawing tangents to the curve of a logarithmic plot of

mobility against temperature the values of γ appropriate to various temperatures may be found. Hence the relationship between q and T may be deduced. Knowing the value of q corresponding to a particular temperature and the appropriate value of η^* from the thermoelectric power measurements the values of $A_{n,p}$ and $B_{n,p}$ may be enumerated. The electronic component of the thermal conductivity may then be calculated using (2.58). By repeating this process at different temperatures the electronic component may be calculated for the range over which the thermal conductivity has been measured.

CHAPTER 3

3.1. ELECTRICAL METHODS.

3.1.1. Operation of the Electrical Circuit.

In Section 2.2 it was shown that if a sample carrying a direct current is suitably orientated with respect to a magnetic field, a transverse voltage is obtained which is the sum of the transverse voltages resulting from the Hall effect, the Ettinghausen effect, the Nernst effect and the Righi-Leduc effect. The transverse voltage is primarily due to the Hall contribution, with the Ettinghausen contribution forming the greater part of the remainder, and the Nernst and Righi-Leduc contributions together providing an extremely small increment to make up the sum.

Therefore, in order to accurately determine the value of the Hall voltage, the Ettinghausen voltage, which may be of third order magnitude, must be removed. Since the Ettinghausen voltage is derived from the flow of charge brought about by a lateral temperature gradient, it must disappear if this temperature gradient is removed. By choosing a circuit in which the Hall voltage is set up by a sample current which is frequently reversed, so that no temperature gradients can be set up in the sample, the three subsidiary voltage contributions can be eliminated.

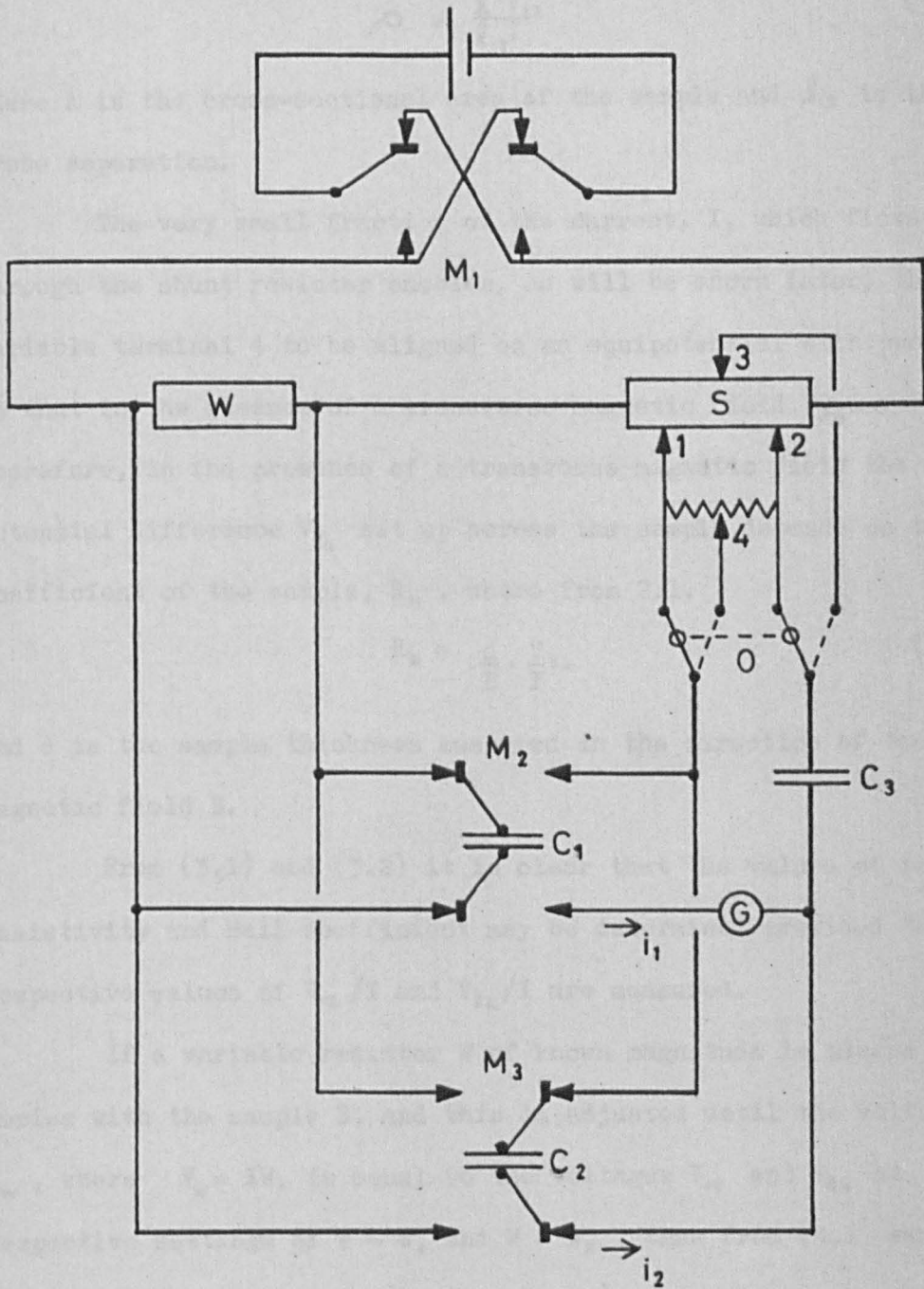
54

The circuit designed by Dauphinee and Mooser incorporates this feature and provides an accurate method for determining the Hall coefficient and the electrical resistivity of a given material. A simplified version of the circuit is shown in fig.8. This provides a means of discussing the principles involved in the experimental method.

In fig.8, the sample, S, is shown to be in contact with the potential probes, 1, 2, and 3. A high resistance shunt, of order 10^1 or 10^3 times the sample resistance, connects terminals 1 and 2.

Fig. 8

SIMPLIFIED ELECTRICAL CIRCUIT



This is provided with a variable terminal 4, which acts as a fourth potential probe.

If a current, I , flows through the sample and its shunt, then a potential difference, V_{12} , is set up of a magnitude which depends on the sample resistivity, ρ , given by

$$\rho = \frac{A V_{12}}{l_{12} I} \quad (3.1)$$

where A is the cross-sectional area of the sample and l_{12} is the probe separation.

The very small fraction of the current, I , which flows through the shunt resistor enables, as will be shown later, the variable terminal 4 to be aligned on an equipotential with probe 3, so that in the absence of a transverse magnetic field $V_{34} = 0$. Therefore, in the presence of a transverse magnetic field the potential difference V_{34} set up across the sample depends on the Hall coefficient of the sample, R_H , where from 2.1.

$$R_H = \frac{d}{B} \cdot \frac{V_{34}}{I} \quad (3.2)$$

and d is the sample thickness measured in the direction of the magnetic field B .

From (3.1) and (3.2) it is clear that the values of the resistivity and Hall coefficient may be determined provided the respective values of V_{12}/I and V_{34}/I are measured.

If a variable resistor W of known magnitude is placed in series with the sample S , and this is adjusted until the voltage V_w , where $V_w = IW$, is equal to the voltages V_{12} and V_{34} at respective settings of $W = W_1$ and $W = W_2$, then from (3.1) and (3.2), and using practical units (C.G.S. e.m.u.),

$$\rho = \frac{A}{l_{12}} W_1 \quad \Omega \text{ cm.} \quad (3.3)$$

$$\text{and } R_H = \frac{d}{B} \cdot 10^8 W_2 \quad \text{coul. cm.}^3 \quad (3.4)$$

The function of the circuit shown in Fig.8 is to provide a means of isolating the potential difference V_{12} and V_{34} and comparing them with V_w .

The double-pole, double-throw chopper, M_1 , set to make-before-break, converts the direct current in the primary circuit into a square wave alternating current in the secondary circuit containing W and S. The make-before-break adjustment ensures that the electrical connections of M_1 are reversed before the current direction in the secondary circuit is reversed, so that sparking is prevented.

Two more choppers, M_2 and M_3 , with their moving contacts bridged by capacitors C_1 and C_2 respectively, are set to break-before-make and driven synchronously with chopper M_1 . Choppers M_2 and M_3 are phased with respect to chopper M_1 so that when the current flows in one direction, say I^+ , capacitor C_1 is connected to W and C_2 is simultaneously connected to S. The break-before-make adjustment of M_2 and M_3 ensures that C_1 and C_2 are only connected to W and S when I^+ is at a steady value. Capacitor C_1 disconnects from W and capacitor C_2 simultaneously disconnects from S before the current I^+ is reduced to zero when the contacts of M_1 are shorted by the make-before-break action. The current flowing through W and S is then reversed by M_1 and reaches a steady value I^- before C_1 connects to S and C_2 connects to W. Later M_2 disconnects C_1 from S and M_3 disconnects C_2 from W, before I^- falls to zero and reverses to I^+ , with the complete cycle repeating itself at 35 cycles/sec., the frequency at which all three choppers are driven.

Before proceeding to discuss the currents i_1 , and i_2 set up in the circuit, it must be pointed out that the purpose of C is to act as a device for preventing any thermal e.m.f.'s generated in the sample from being communicated to the direct current galvanometer G. Suppose the potential difference across C_3 is V_{C3} . If any difference

exists between V_w^+ and $-V_s^-$, where the superscripts denote the directions of currents I^+ and I^- , a pulsing direct current i_1 , generated by the voltage ΔV_1 , flows through G_v every even half cycle, where

$$\begin{aligned}\Delta V_1 &= V_w^+ - (-V_s^-) - V_{c3} \\ &= V_w^+ + V_s^- - V_{c3} \\ &= I^+W + I^-S - V_{c3}\end{aligned}$$

For $I^+ = -I^-$ this becomes

$$\Delta V_1 = I^+(W - S) - V_{c3} \quad (3.5)$$

If the capacitor C_2 were not included, then ΔV_1 and i_1 would decrease in successive cycles and vanish when

$$V_{c3} = I^+(W - S)$$

By including the capacitor C_2 any difference between V_w^- and $-V_s^+$ is reflected by a pulsing direct current i_2 , generated by a voltage ΔV_2 , which flows through the sample every odd half cycle.

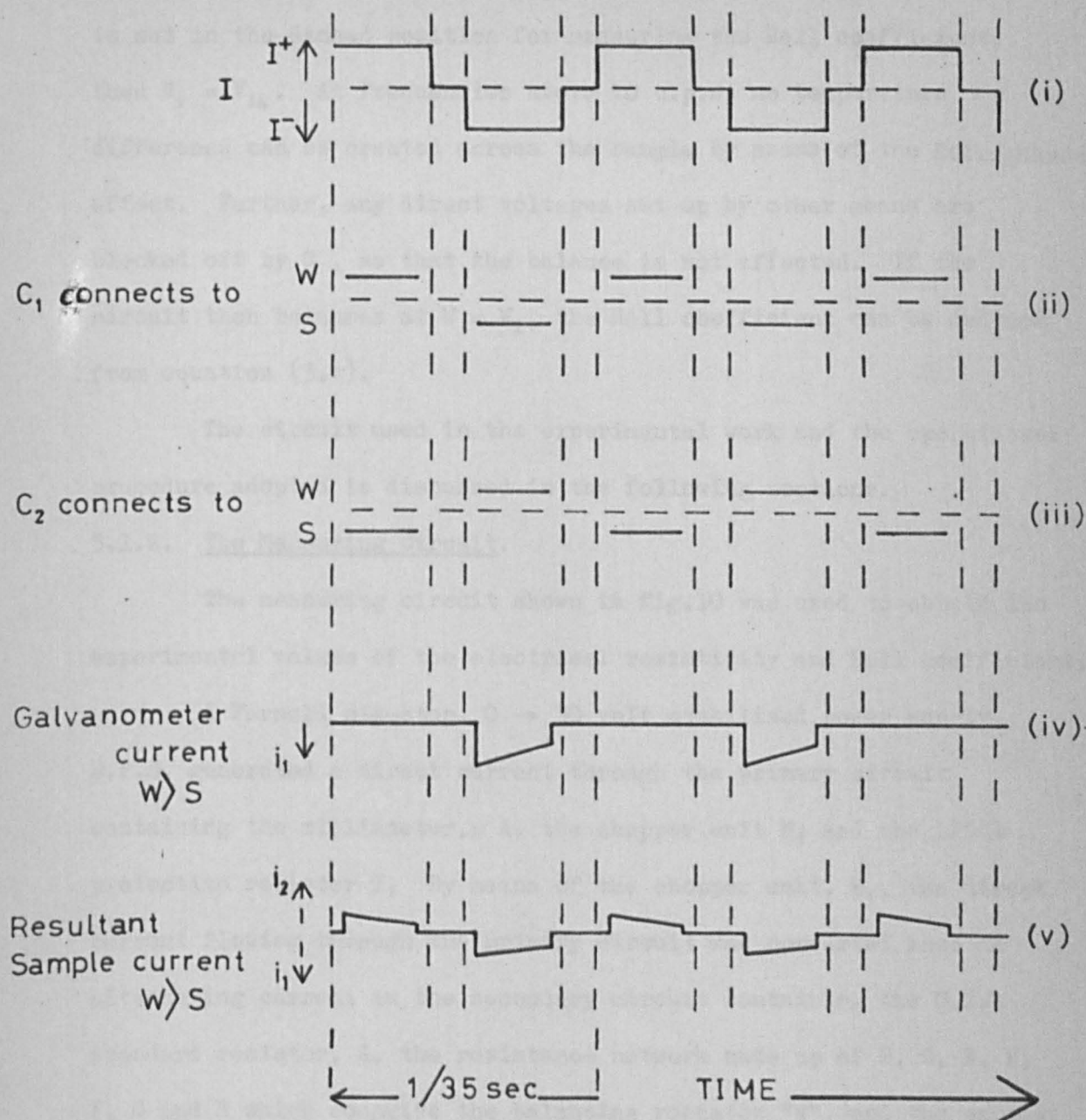
$$\begin{aligned}\therefore \Delta V_2 &= V_w^- + V_s^+ + V_{c3} \\ &= I^+(S - W) + V_{c3} \\ &= -\Delta V_1\end{aligned} \quad (3.6)$$

The size of the pulsed currents i_1 and i_2 is maximised by keeping the resistance of the circuit as low as possible and making the time constants as large as possible by maximising C_1 , C_2 and C_3 .

The pulsed currents i_1 and i_2 , therefore, flow through the sample in opposite directions, with a phase difference of $\pi/2$ in the chopper cycle, forming a resultant alternating current which is not impeded by C_3 , as shown in fig.9.

Therefore, the galvanometer current i_1 does not decrease in successive cycles but produces a steady deflection whenever $I^+(W-S) \neq 0$. When $W = S$, V_{c3} decays to zero and $\Delta V_1 = \Delta V_2 = 0$, so that $i_1 = i_2 = 0$ and a null deflection indicates that the circuit is balanced.

Fig.9



In the circuit shown in fig.8, $V_s = V_{12}$ and a resistive balance is obtained when $W = W_1$. The resistivity can then be deduced from equation (3.3). If the two-pole, two-position switch 0 is set in the dashed position for measuring the Hall coefficient, then $V_s = V_{34}$. At frequencies above 10 c.p.s. no temperature difference can be created across the sample by means of the Ettinghausen effect. Further, any direct voltages set up by other means are blocked off by C, so that the balance is not affected. If the circuit then balances at $W = W_2$, the Hall coefficient can be deduced from equation (3.4).

The circuit used in the experimental work and the operational procedure adopted is discussed in the following sections.

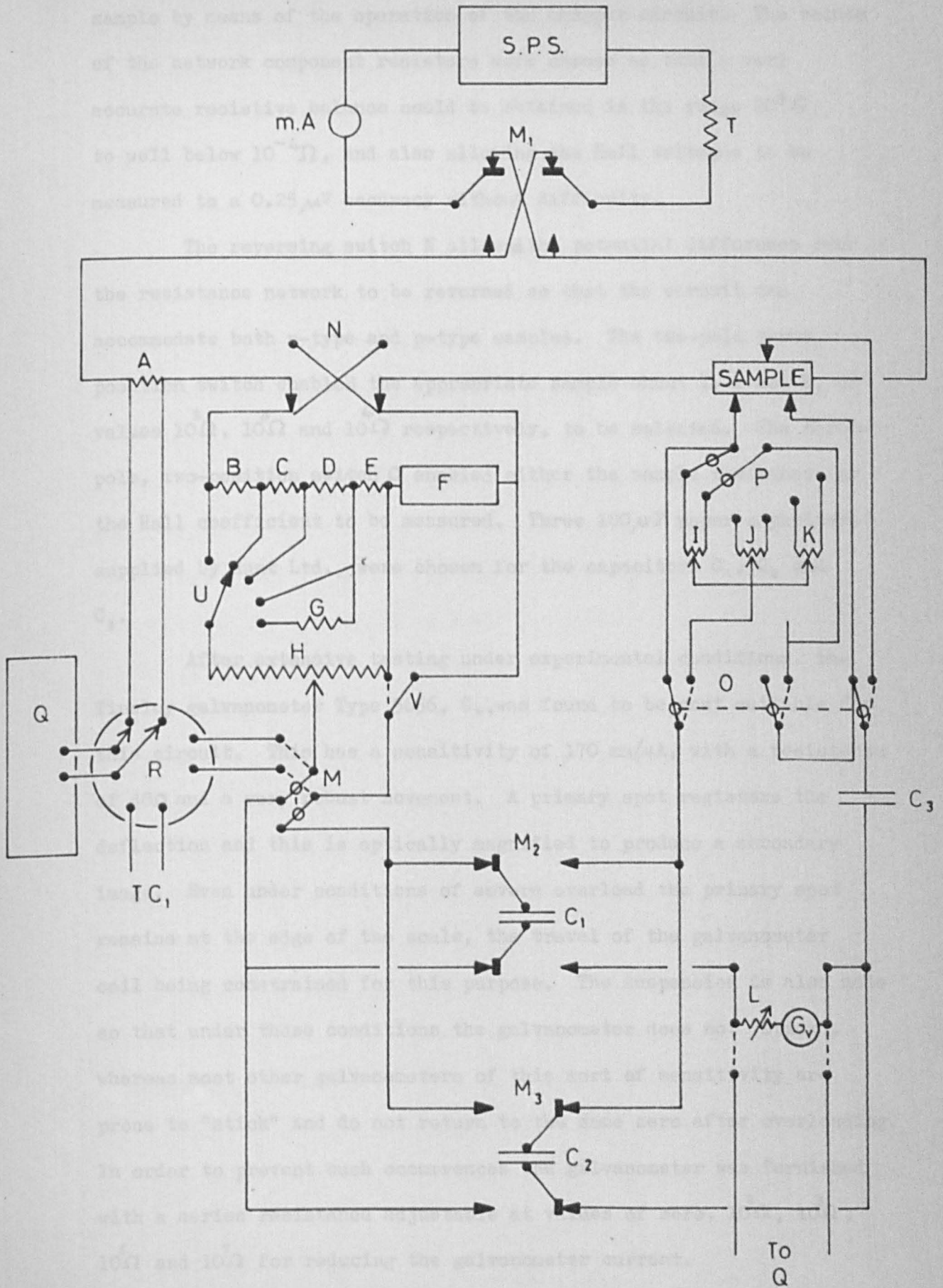
3.1.2. The Measuring Circuit.

The measuring circuit shown in fig.10 was used to obtain the experimental values of the electrical resistivity and Hall coefficient.

A Farnell six-step, 0 → 30 volt stabilised power supply, S.P.S. generated a direct current through the primary circuit containing the milliammeter, $m A$, the chopper unit M_1 , and the 125Ω protective resistor T. By means of the chopper unit, M_1 , the direct current flowing through the primary circuit was converted into an alternating current in the secondary circuit containing the 0.1Ω standard resistor, A, the resistance network made up of B, C, D, E, F, G and H which comprise the balancing resistor "W", and the sample. Resistors B and C were high stability Muirhead resistors having values of 10Ω and 1Ω respectively. Resistors D and E were laboratory made Kanthal resistors having nominal values of 0.1Ω and 0.01Ω respectively, while resistor G was given a value of 100Ω . The remaining three-terminal, ten-turn non-inductive, 25Ω Helipot H and the five-dial (10×10^{-1} , 1, 10, 10^2 , $10^3\Omega$) resistance box then completed the balancing resistor network.

Fig.10

THE MEASURING CIRCUIT



By suitably setting switches U and V the potential difference across the network could be matched against that derived from the sample by means of the operation of the chopper circuit. The values of the network component resistors were chosen so that a very accurate resistive balance could be obtained in the range $10^3 \Omega$ to well below $10^{-4} \Omega$, and also allowing the Hall voltages to be measured to a $0.25 \mu V$ accuracy without difficulty.

The reversing switch N allowed the potential difference over the resistance network to be reversed so that the circuit can accommodate both n-type and p-type samples. The two-pole three position switch enabled the appropriate sample shunt I, J and K, of values $10^2 \Omega$, $10^3 \Omega$ and $10^4 \Omega$ respectively, to be selected. The three-pole, two-position switch O enabled either the sample resistance or the Hall coefficient to be measured. Three $100 \mu F$ paper capacitors supplied by Hunt Ltd., were chosen for the capacitors C_1 , C_2 and C_3 .

After extensive testing under experimental conditions, the Tinsley galvanometer Type 5656, G_v , was found to be most suitable for this circuit. This has a sensitivity of $170 \text{ mm}/\mu A$, with a resistance of 48Ω and a very robust movement. A primary spot registers the deflection and this is optically magnified to produce a secondary image. Even under conditions of severe overload the primary spot remains at the edge of the scale, the travel of the galvanometer coil being constrained for this purpose. The suspension is also made so that under these conditions the galvanometer does not "stick", whereas most other galvanometers of this sort of sensitivity are prone to "stick" and do not return to the same zero after overloading. In order to prevent such occurrences the galvanometer was furnished with a series resistance adjustable at values of zero, $10^2 \Omega$, $10^3 \Omega$, $10^5 \Omega$ and $10^7 \Omega$ for reducing the galvanometer current.

By measuring the potential difference developed across the terminals of a chromel-alumel thermocouple, TC_1 , with the potentiometer, Q , the sample temperature could be deduced. The choppers M_1 , M_2 and M_3 may be given appropriate settings in the following manner. In the Tinsley Low Thermal Chopper used for this work, the three choppers M_1 , M_2 and M_3 are all operated by eccentric bearings screwed to the arm of an electric motor driven at 35 c.p.s. The relative orientations of the eccentric bearings determine the relative phase angles at which the choppers make and break contact in the chopper cycle. The lengths of time for which a given chopper makes and breaks electrical contact is governed by setting screws. By adjusting these the period of contact may be increased or reduced as desired. Therefore, in order to produce the required chopping patterns, shown in fig.9, the eccentrics must be reorientated on the rotor arm and the setting screws must be suitably adjusted. This can conveniently and accurately be done by attaching a pointer to the rotor arm which can rotate over a fixed concentric protractor scale. If an avometer is connected across the two terminals under investigation, turning the rotor arm causes a small resistance to be registered when contact is made and an infinite resistance to be registered when contact is broken. Using the protractor, the angles at which contact is made and broken for chopper M_1 may be measured. The period of contact may then be adjusted by means of setting screws. By repeating this procedure with the second chopper, M_2 , the phase relationship between the two choppers may be found. The eccentric bearings and set screws may then be used to establish the correct phase patterns and contact periods for this chopper. By repeating the same process for the third chopper, M_3 , the process may be completed.

3.1.3. Measurement Procedure and Accuracy.

After switching on the chopper and power supply the resistance of the network BCDEFGH was altered until a null deflection was recorded on the galvanometer, G_v . The resistance of the network was then equal to the resistance of the sample. The value of this resistance was then obtained by stopping the chopper so that a steady direct current flowed through the 0.1Ω standard resistor, A, the balancing resistor BCDEFGH and the sample. After switching the galvanometer G_v into the circuit of the potentiometer, Q, and setting switch R as shown, the potential difference across the standard resistance, A, was measured. By means of Ohm's Law the current flowing through A, the balancing resistance BCDEFGH and the sample was deduced. By then setting switch M to the dotted position and using switch R, the potential difference across the balancing resistance was also obtained. Knowing the potential difference across the balancing resistance and the current flowing through it, a further application of Ohm's Law gave the resistance of both the balancing network and the sample.

The accuracy of this circuit was tested using a series of standard resistances to simulate the sample resistance. For each standard resistance the circuit was balanced several times and the average value deduced is given in the table below.

Standard Resistance (Sample) Ω	Balancing Resistance $W \Omega$	Accuracy $\frac{\Delta W}{W}$ (+) (-)	Mean Deviation
10^{-3}	1.003×10^{-3}	0.003	0.004
10^{-2}	0.9985×10^{-2}	0.002	0.003
10^{-1}	1.001×10^{-1}	0.001	0.008
1	1.004	0.004	0.005
10	0.9997×10	0.0003	0.001
10^2	0.997×10^2	0.003	0.005
10^3	0.960×10^2	0.041	0.042

Plates 1 and 2 show general views of the apparatus used in the present work. Plate 3(a) shows the sample holder, a description of which is given below.

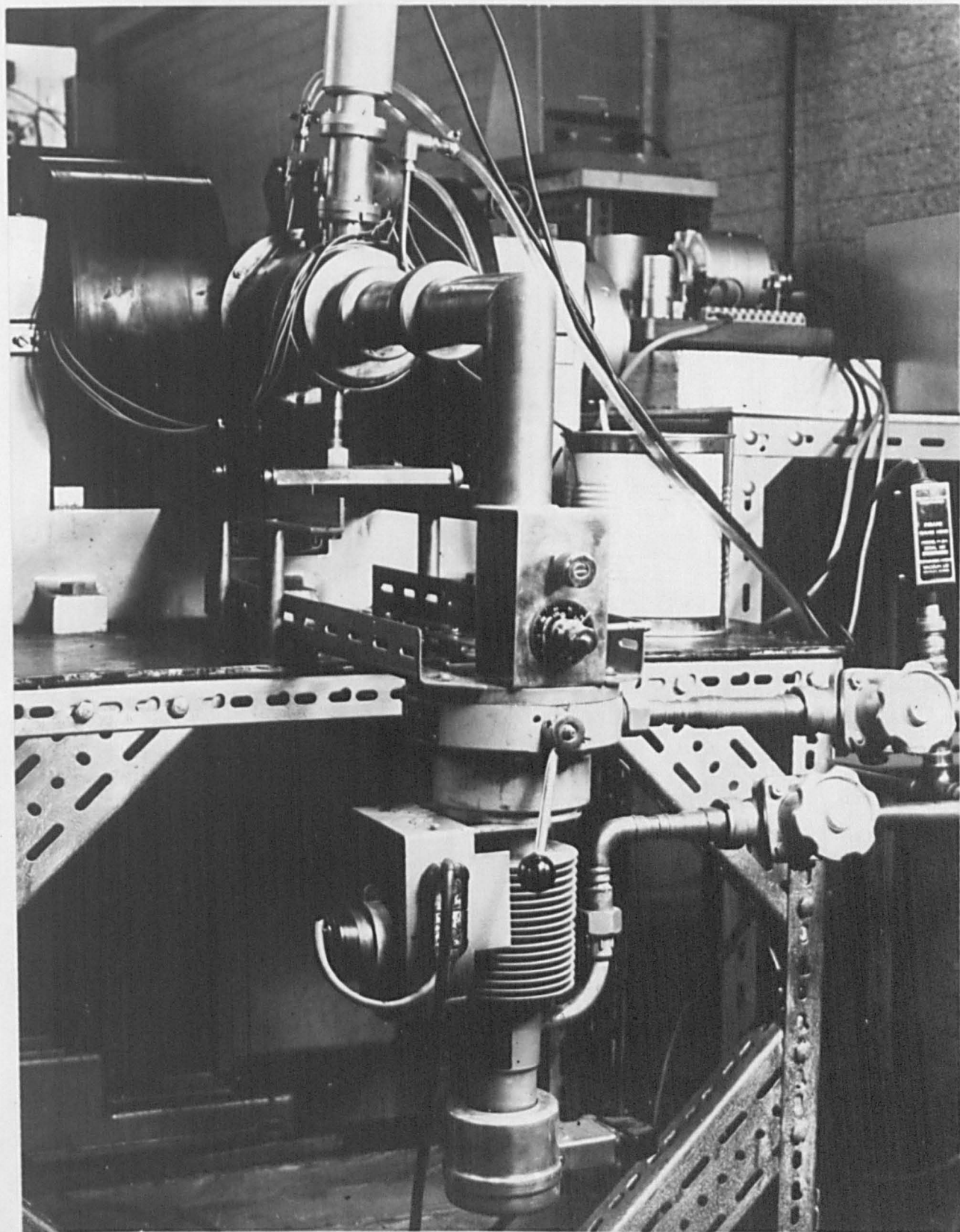
3.1.4. The Sample Holder.

The material chosen for the sample holder was pyrophyllite, a naturally occurring mineral. This is a machinable electrical insulator capable of withstanding a wide range of temperature. The material is machined in its soft, raw state and then heat treated at 1200°C when it becomes a hard ceramic.

The pyrophyllite was initially shaped into an "I" section. A groove was sunk into the middle part of the "I" section, parallel to the long edges of the sample holder. A central portion of this groove, long enough to accommodate the sample, was given a rectangular section, while the rest of the groove was given a dovetail section. Three metal blocks, fashioned in chromel, were given dovetail base sections to fit in the dovetail sections of the groove, two on one side and one on the other side of the sample. Eight B.A. threads were cut into two of these blocks to take small lock nuts which were used to secure current leads and form current contacts on either side of the sample. A chromel-alumel thermocouple TC₁, brazed deep into a hole drilled in the third block was used to record the sample temperature. An elliptical spring was placed between the thermocouple block and the current contact block to ensure that good electrical contact was maintained between the current contacts and the sample. Since molybdenum retains its spring properties over a very wide range in temperature, the elliptical spring, of width 0.06" and thickness 0.005", was constructed from this material.

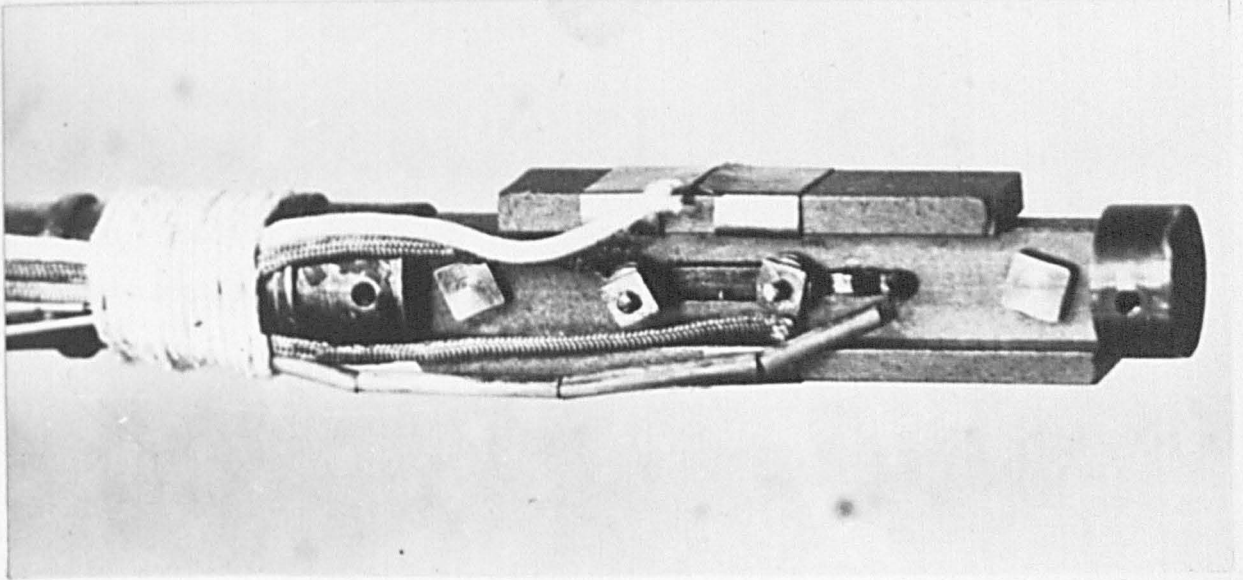
Molybdenum wire of diameter 0.039" was used to make the three potential probes. The stock of each probe was of the full diameter

Plate 2.

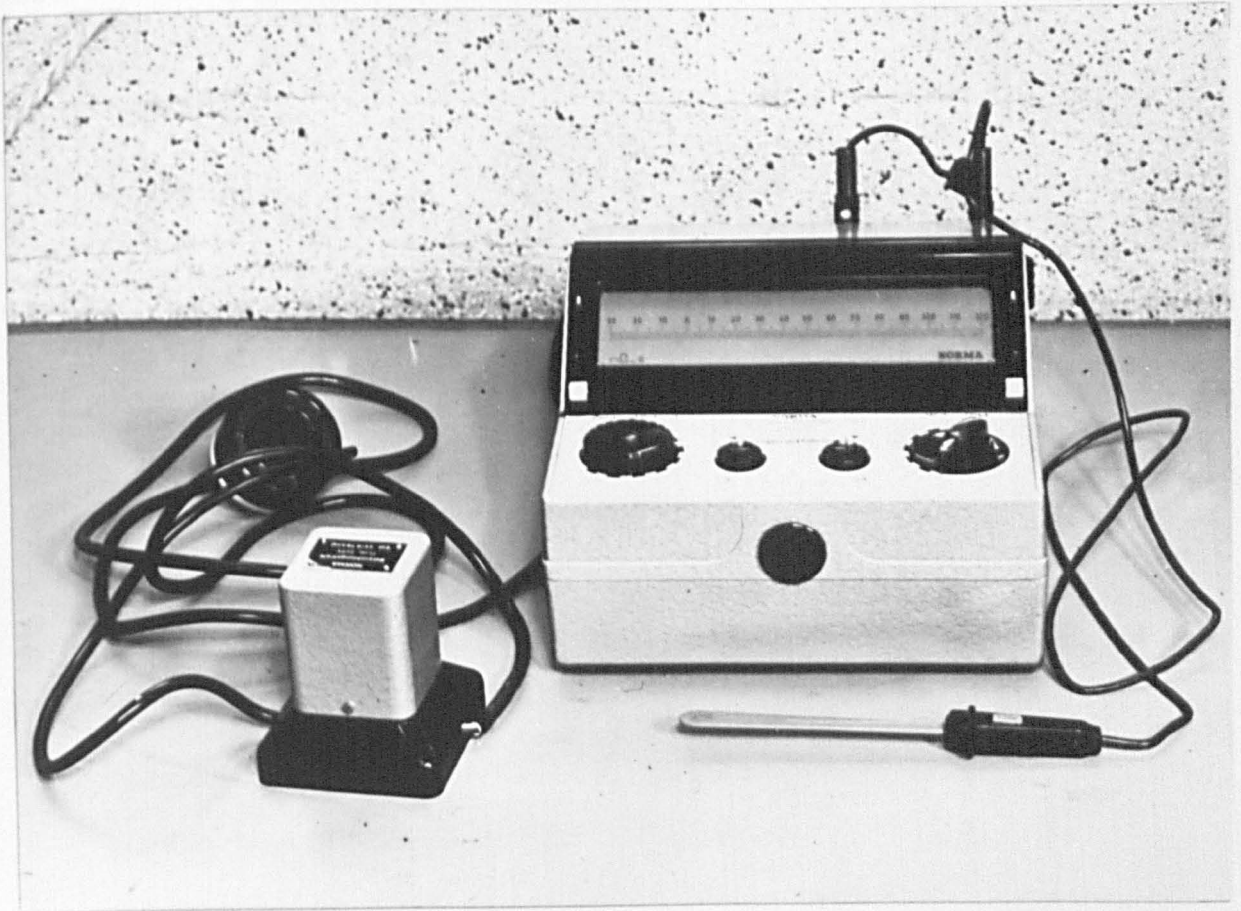


HALL - CONDUCTIVITY APPARATUS : REAR VIEW.

Plate 3.



(a) SAMPLE HOLDER



(b) FLUXMETER

of the wire and the point contact was produced by reducing the diameter to 0.003" at one end. Chromel leads were welded to the other end of each probe connecting to the electrical circuit.

The probes were led through 0.040" diameter holes, drilled in the top and bottom faces of the sample holder, to the sample. The length of the probes was such that, in place, their welded ends stood above the top and bottom faces of the sample holder. Pressure was applied on the probes, ensuring good electrical contact with the sample, by means of molybdenum springs. These were shaped to slide over the top and bottom faces of the sample holder and press on the probes. The pressure exerted on the sample by the probes then depended on the extent by which they are overlapped by their springs.

A simple tool was constructed which enabled these springs to be simply pressed out of 0.005" thick, 0.875" wide molybdenum strip. Thicker material was found to be unsuitable as the pressure adjustment became less sensitive, increasing the likelihood of sample fracture. The general features of the sample holder described above are readily recognisable in Plate 3(a).

3.1.5. The Furnace.

In order to obtain large magnetic fields the separation of the poles of the magnet must be kept as small as possible. This sets an upper limit on the diameter of the furnace tube which must fit between the poles. Accordingly, a 1" inside diameter, $1\frac{1}{4}$ " outside diameter, 2' long cylinder of impervious Mullite was selected for the furnace tube. A 30 Ω heating element of 0.05" thick, 0.20" wide Kanthal tape was wound on the centre 10" section of the furnace tube and cemented in place using alumina cement. A quartz fibre layer, bound with Refrasil tape was then used to thermally and electrically insulate the furnace.

The ends of the Mullite tube were initially uneven and were ground flat, using finely divided silicon carbide, to form part of a vacuum seal. The seal was completed by clamping the ends of the furnace tube against flat gasket neoprene valves, mounted in water cooled copper and brass end caps. The latter were connected to the pumping line as shown schematically in Fig.11.

The larger of the furnace end caps was fitted with a bracket enabling it to support a long $\frac{1}{4}$ " diameter Chromel bar to which the sample holder could be bolted. The bar, which carried polished molybdenum radiation shields on either side of the sample holder, allowed the latter to be supported clear of the furnace walls at the centre of both the furnace and the magnetic field.

The same end cap was supplied with a Penning Gauge to measure the pressure of the system and a glass/metal seal by which the electrical and thermocouple leads were brought out of the vacuum system. A further small tube seal, shown blanked off, was included to enable the end cap to perform its dual function as the outer container of a simple cryostat, described later.

The pumping line attached to the larger end cap was connected to the Metrovac GB2 diffusion pump, the roughing and backing valves, the Pirani Gauge and the Metrovac GDR1 rotary pump. After evacuating the system with the rotary pump, the Pirani Gauge was then used to ensure that the pressure was sufficiently low before the diffusion pump and Penning Gauge were activated. The pumping line also contained a needle valve by which nitrogen could be introduced to the evacuated system in order to prevent sample oxidation at high temperatures and an air inlet valve for releasing the vacuum.

The circuit in Fig.12 shows the Smith Temperature Controller which governed the heater current to the furnace. The temperature controller was set to the desired furnace temperature and the circuit

Fig.11

THE FURNACE

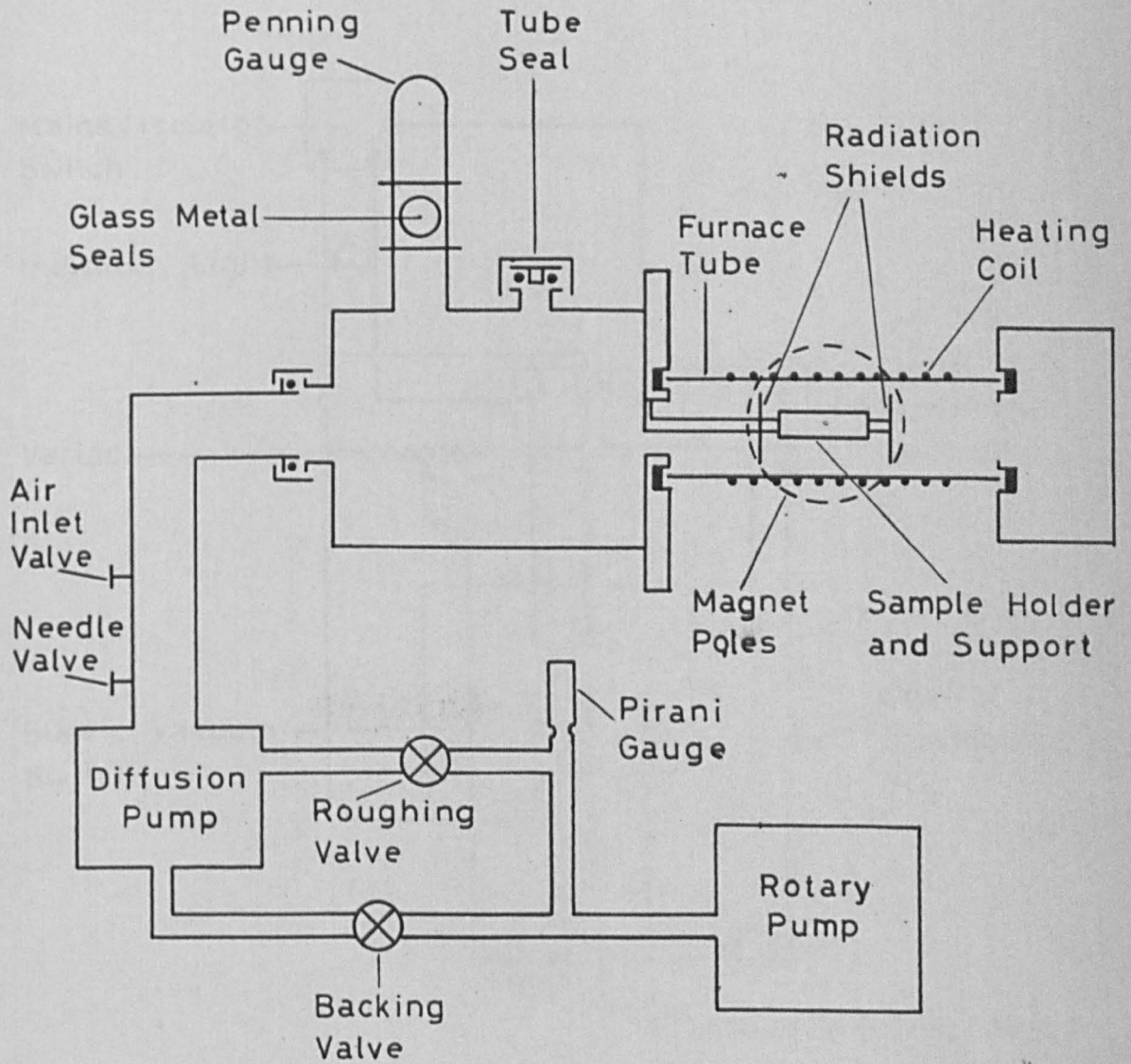
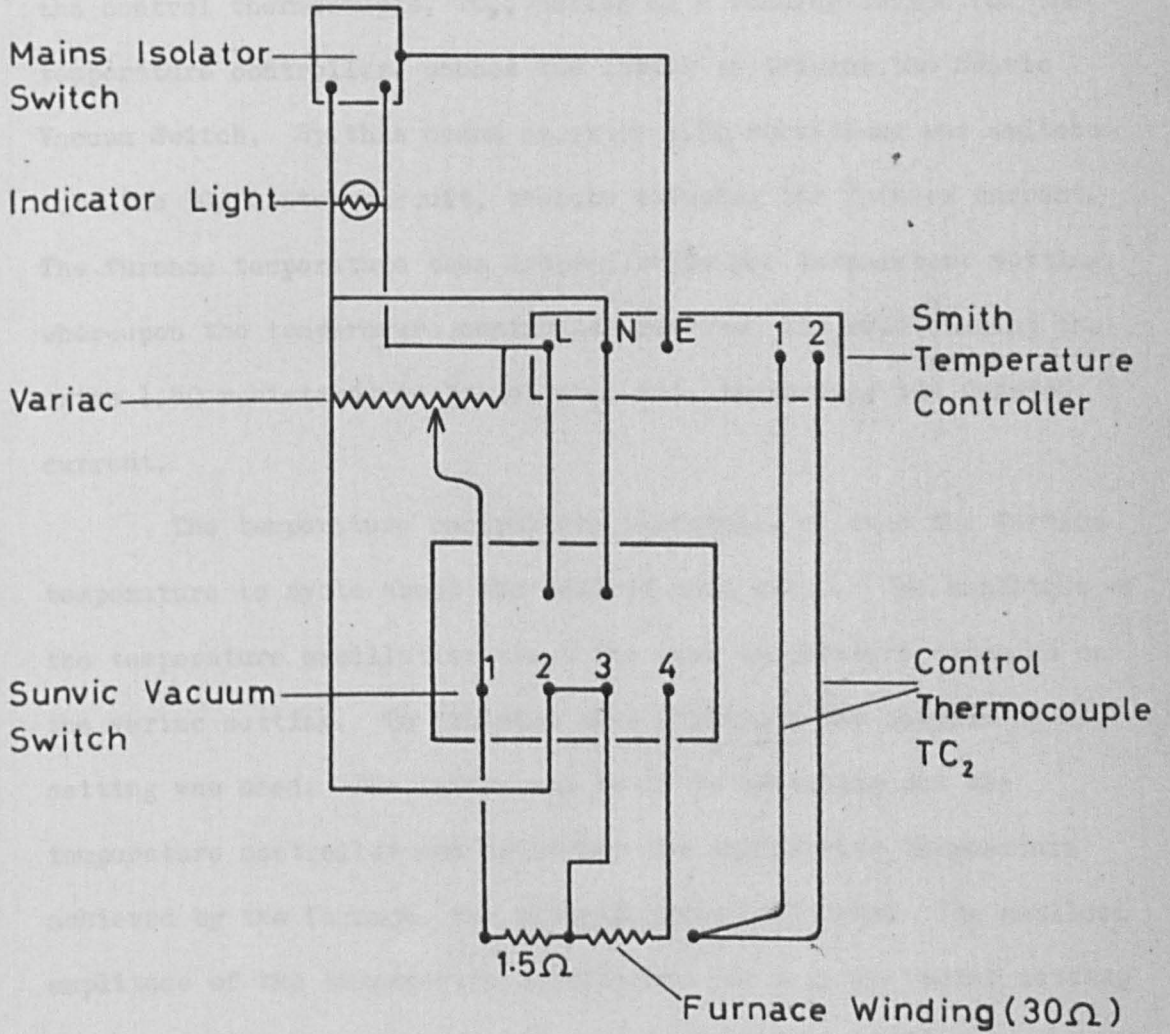


Fig.12

ELECTRICAL CIRCUIT OF THE FURNACE



was switched on so that the on/off indicator light was illuminated. The voltage supplied to the heating element was determined by the variac setting. The furnace temperature was communicated by the nitrogen gas to the control thermocouple, TC_2 , secured to the chromel bar near the sample.

If the furnace temperature exceeded the temperature setting, the control thermocouple, TC_2 , acting as a sensing device for the temperature controller, causes the latter to trigger the Sunvic Vacuum Switch. By this means an extra 1.5Ω resistance was switched into the 30Ω heater circuit, thereby reducing the furnace current. The furnace temperature then dropped below the temperature setting, whereupon the temperature controller reversed its role causing the extra 1.5Ω resistance to be switched out, increasing the furnace current.

The temperature controller, therefore, allowed the furnace temperature to cycle about the desired mean value. The amplitude of the temperature oscillation about the mean temperature depended on the variac setting. To minimise this amplitude the optimum variac setting was used. The latter was found by switching out the temperature controller and measuring the equilibrium temperature achieved by the furnace, for several variac settings. The smallest amplitude of the temperature oscillation for a given variac setting was then obtained by setting the temperature control 5% less than the equilibrium temperature. In this way the calibration graph of optimum variac settings against temperature control settings shown in Fig.13 was obtained. Using these values the amplitude of the temperature cycle at the highest temperature settings did not exceed $1^\circ K$.

By drawing a thermocouple through the furnace at equilibrium temperatures and recording the temperatures at variable points along

Fig. 13

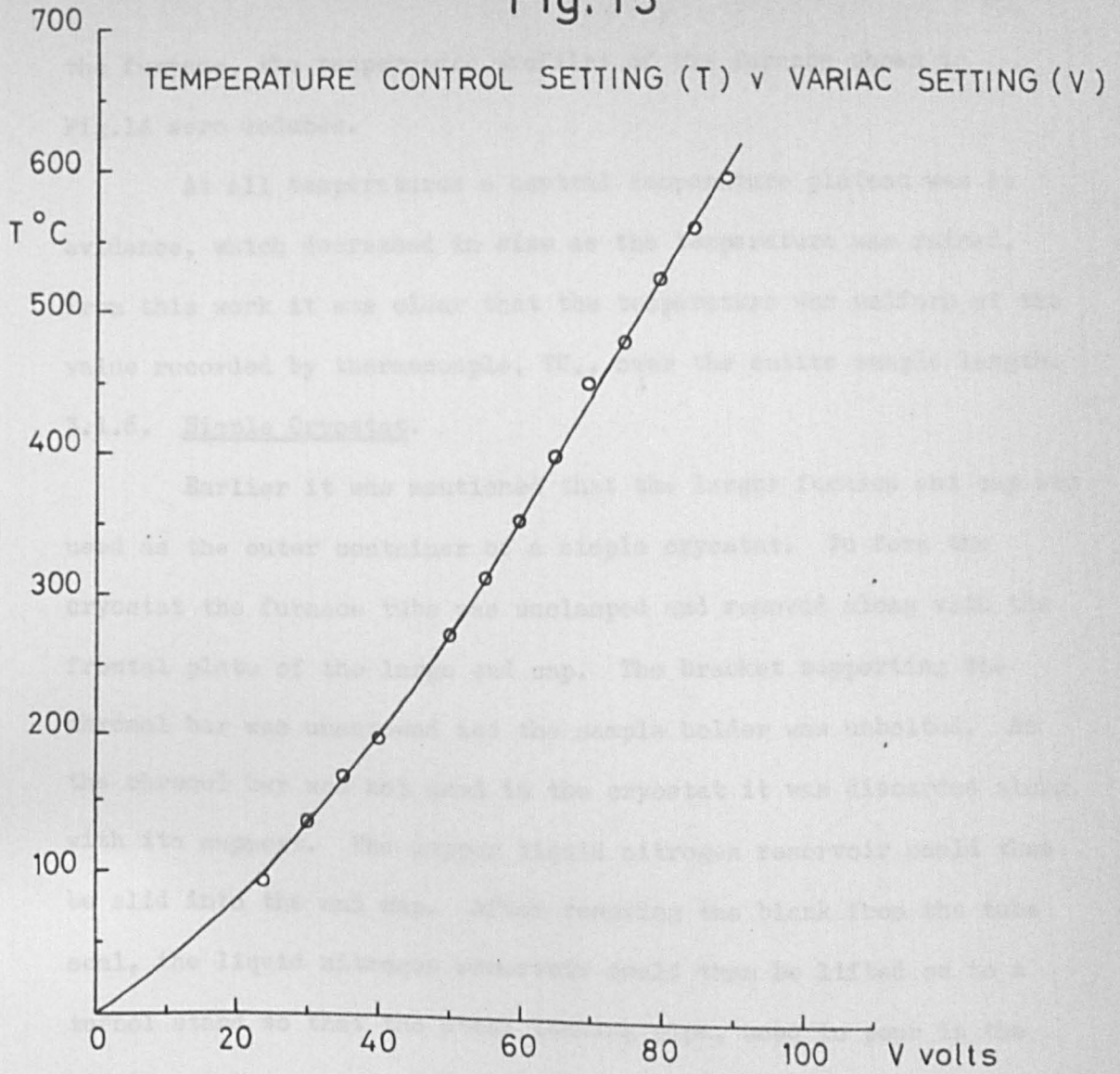
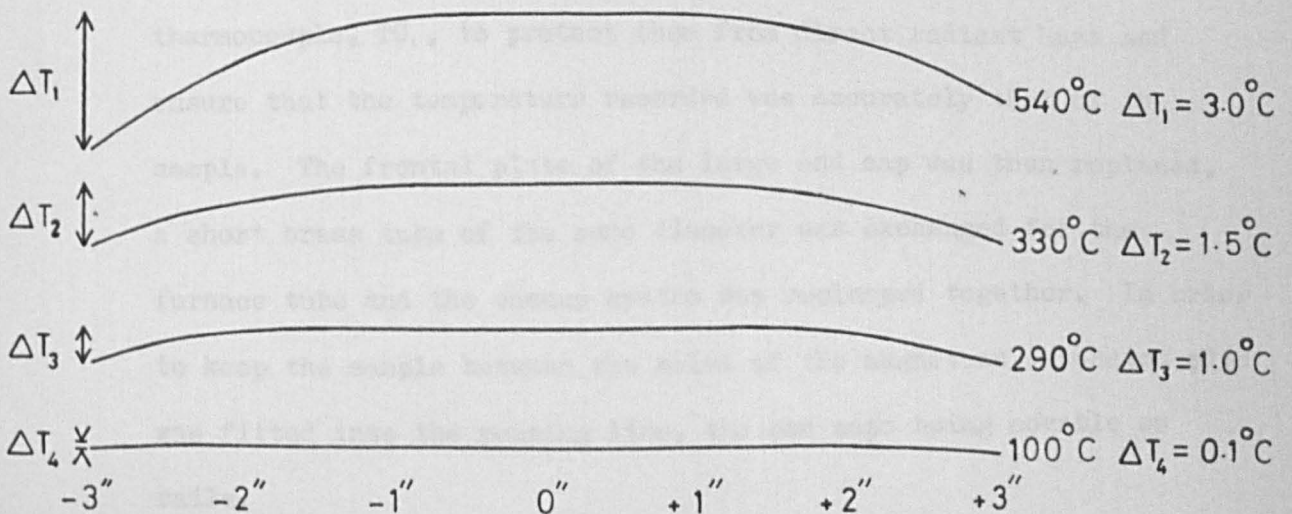


Fig. 14

TEMPERATURE PROFILE OF FURNACE

Zero indicates the sample location at the centre of the furnace.



the furnace, the temperature profiles of the furnace shown in Fig.14 were deduced.

At all temperatures a central temperature plateau was in evidence, which decreased in size as the temperature was raised. From this work it was clear that the temperature was uniform at the value recorded by thermocouple, TC,, over the entire sample length.

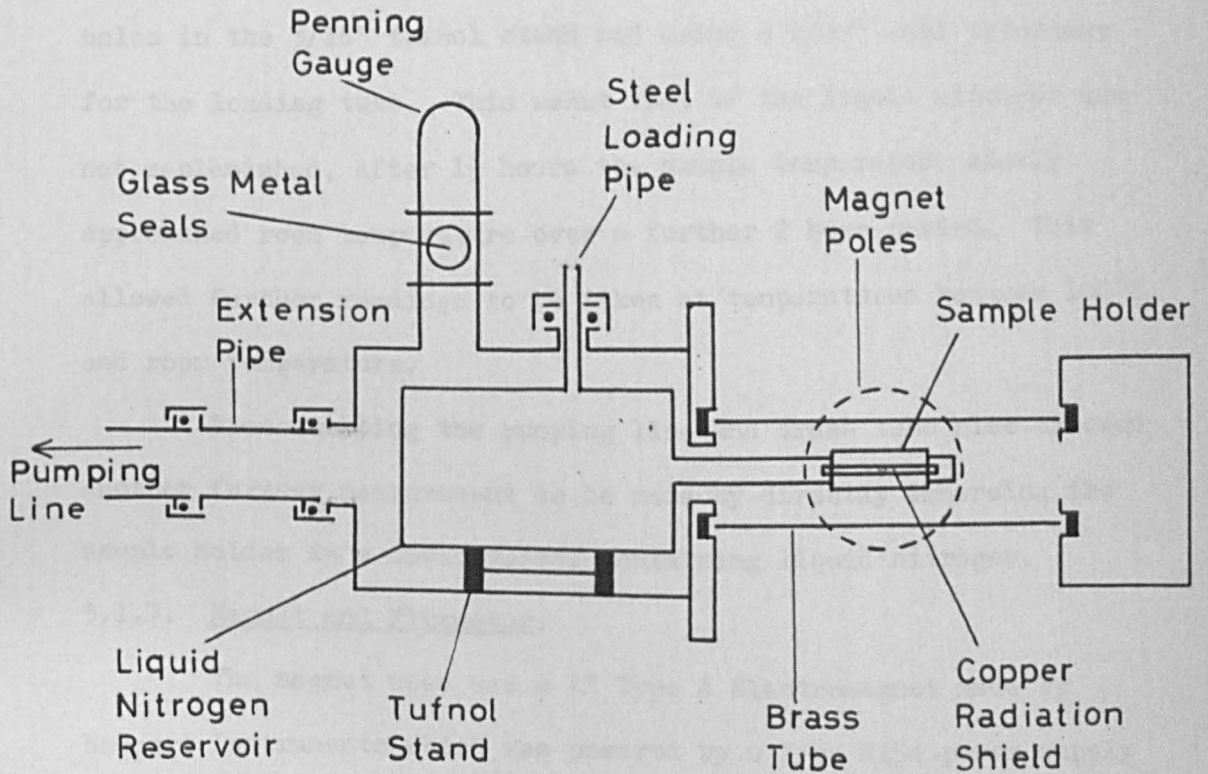
3.1.6. Simple Cryostat.

Earlier it was mentioned that the larger furnace end cap was used as the outer container of a simple cryostat. To form the cryostat the furnace tube was unclamped and removed along with the frontal plate of the large end cap. The bracket supporting the chromel bar was unscrewed and the sample holder was unbolted. As the chromel bar was not used in the cryostat it was discarded along with its support. The copper liquid nitrogen reservoir could then be slid into the end cap. After removing the blank from the tube seal, the liquid nitrogen reservoir could then be lifted on to a tufnol stand so that the steel loading pipe, used to pour in the liquid nitrogen, protruded through the seal. The seal could then be remade as shown in Fig.15.

The sample holder was then rebolted to a long copper bar brazed to the liquid nitrogen reservoir, as shown in Plate 3. A copper shield was then screwed to the copper bar over the sample and thermocouple, TC,, to protect them from direct radiant heat and ensure that the temperature recorded was accurately that of the sample. The frontal plate of the large end cap was then replaced, a short brass tube of the same diameter was exchanged for the furnace tube and the vacuum system was resealed together. In order to keep the sample between the poles of the magnet an extension pipe was fitted into the pumping line, the end caps being movable on rails.

Fig.15

THE CRYOSTAT



The pumping system allowed the pressures measured by the Penning Gauge to be reduced to 10^{-5} m.m.Hg. Fully charging the liquid nitrogen reservoir, then allowed the temperature of the sample to be reduced to a steady value of about 100°K for approximately $1\frac{1}{2}$ hours. The inward heat flow arose mainly through the walls of the steel loading tube, the tufnol stand and the electrical and thermocouple leads. This was minimised by drilling holes in the $3/16$ " tufnol stand and using a $1/32$ " wall thickness for the loading tube. This meant that if the liquid nitrogen was not replenished, after $1\frac{1}{2}$ hours the sample temperature slowly approached room temperature over a further 2 hour period. This allowed further readings to be taken at temperatures between 100°K and room temperature.

Disconnecting the pumping line and brass tube also allowed another further measurement to be made by directly immersing the sample holder in a dewar vessel containing liquid nitrogen.

3.1.7. Magnet and Fluxmeter.

The magnet used was a 4" Type A Electromagnet made by *Newport Instruments* which was powered by a Type H154 power supply of the same make. A feature of this power supply is its automatic current reversing facility. However, due to the design of the output current ammeter, accurate adjustment of the current is very difficult, making consistent adjustment to exactly the same magnetic field impossible. This difficulty was overcome by introducing a multi-range Cambridge Unipivot ammeter between the power supply and the magnet. This instrument allowed very accurate setting of the magnet current, at a cost of losing the automatic reversing facility. Using the Unipivot ammeter direct currents between 0.1A and 20A could be set to an accuracy which was usually less than 0.3%. After setting the current, the Type H154 power supply guaranteed the current

stability to ± 1 part in 10, over a period of $\frac{1}{2}$ hour.

A Norma Model 251F, shown in Plate 3(b) was used to calibrate the magnetic field. This instrument has 10 ranges varying from 5×10^{-6} to 5×10^{-3} Webers per scale division. The search coil which is also shown in Plate 3(b) was composed of 100.5×10^{-4} area turns M^{-2} . The magnetic induction, B, was then given by

$$B \text{ (Gauss)} = \frac{\text{Range} \times \text{deflection}}{\text{Coil Area Turns (cm)}}$$

The calibration was carried out in the following way. The magnet current was taken up to its maximum value and then lowered to desired setting. The search coil was placed in the centre of the magnetic field and then swiftly removed from the influence of the magnetic field. The deflection and range were then noted and the above formula was applied. This process was repeated three times before inverting the search coil and gaining three more deflections in the opposite direction. The magnet current was then reduced to zero and the current generator was switched off. The current leads on the Unipivot ammeter were then reversed and the direction of current flow from the power supply was also reversed. The current was then taken up to its maximum value and again lowered to the previous setting. Six further readings were then taken, so that the results shown in table 3.1 are an average of twelve results.

The homogeneity of the magnetic field was examined setting the magnet current at 12A, and taking measurement as above at two points on 8 cm. vertical and horizontal diameters, of the pole-pieces. Over a typical sample length (S.L.) of 1.0cm., the spread of magnetic field was

$$\Delta B_{S.L.} = 13 \text{ G. for } B \neq 7,300 \text{ G.}$$

$$\therefore \left(\frac{\Delta B}{B} \right)_{S.L.} = 1.7 \times 10^{-3} \text{ G.}$$

Over a typical sample width (S.W.) of 0.2cm., the spread

TABLE 3.1.

MAGNET CURRENT (AMPS)	RANGE x AVERAGE DEFLECTION W/SKT. mms	MAGNETIC INDUCTION (B) Gauss	(MAGNETIC INDUCTION) ² (B) ² Gauss ²
0.05	$9.5 \times 5 \times 10^{-6}$	47	0.221×10^4
0.10	$18.9 \times 5 \times 10^{-6}$	94	0.884×10^4
0.30	$55.6 \times 5 \times 10^{-6}$	277	7.64×10^4
0.50	$96.2 \times 5 \times 10^{-6}$	475	22.6×10^4
1.00	$119.6 \times 1 \times 10^{-5}$	1191	1.32×10^6
2.00	$112.7 \times 2 \times 10^{-5}$	2235	4.99×10^6
3.00	$65.77 \times 5 \times 10^{-5}$	3272	10.7×10^6
4.00	$84.52 \times 5 \times 10^{-5}$	4205	16.0×10^6
5.00	$100.2 \times 5 \times 10^{-5}$	4986	24.9×10^6
7.00	$120.8 \times 5 \times 10^{-5}$	6011	36.1×10^6
10.0	$139.2 \times 5 \times 10^{-5}$	6927	48.0×10^6
12.0	$73.65 \times 1 \times 10^{-4}$	7328	53.7×10^6
15.0	$78.35 \times 1 \times 10^{-4}$	7796	60.8×10^6

of magnetic field was

$$\begin{aligned} \Delta B_{s.w.} &= 7G. \\ \therefore \left(\frac{\Delta B}{B}\right)_{s.w.} &= 1 \times 10^{-4} \end{aligned}$$

The above results indicated that the magnetic field was very homogeneous and that the positioning of the sample between the pole-pieces was not critical.

3.1.8. Sample Preparation and Experimental Errors.

InAs.

A slitting wheel was used to cut a sample from a large ingot of pure InAs. The sample of length, $l = 1.0$ cm., average width $b = 0.165$ cm., and thickness $d = 0.141$ cm., was used in a preliminary investigation designed to examine the performance of the sample holder, furnace and cryostat, under operational conditions. In order to ensure that good electrical contact was maintained with the current contacts of the sample holder, the ends of the sample were plated with copper.

InSb/NiSb.

As InSb/NiSb is made up of unidirectionally orientated rod like inclusions of highly conducting NiSb in a matrix of InSb, there are three prime directions in which the Hall coefficient, electrical conductivity and "magnetoresistance" behaviour may be measured. The samples 1, 2 and 3 cut in these orientations are described in the table below.

<u>Sample</u>	<u>Orientation</u>	<u>Inclusion rods</u>	<u>(cm)</u>	<u>b(cm)</u>	<u>d(cm)</u>
1	A	$\parallel B, \perp I$	1.2	0.159	0.107
2	B	$\perp B, \perp I$	1.2	0.166	0.126
3	C	$\perp B, \parallel I$	1.2	0.143	0.119

The samples of length, l , width, b , and thickness, d , listed above were cut from a 1.2 cm. cube of InSb/NiSb. Each of these samples was also given copper plated large area end contacts.

Clearly, by reducing the magnetic field to zero the two orientations A and B became electrically identical. Therefore, only two prime electrical conductivities, σ_{\perp} for samples 1 and 2, and σ_{\parallel} for sample 3 are possible for inclusion rods respectively perpendicular and parallel to the direction of current flow. The Hall coefficients are designated R_H^A , R_H^B and R_H^C according to the orientation of the

inclusion rods with respect to the magnetic field and sample current. The system of notation was then completed by referring to the three prime relative resistances produced by InSb/NiSb in orientations A, B and C as r_A , r_B and r_C .

From the results given in section 3.1.3. it is clear that the error in measuring the resistance of the sample is very small. Due to the small sizes of the samples used, however, the resistivity given by (3.3) may be subject to a dimensional error of 3%. The Hall coefficient given by (3.4) may also be in error by 3% so that the mobility given by (2.34) is subject to an error of 6%.

CHAPTER 4.

4.1. THERMAL METHODS.

4.1.1. Thermal Conductivity and Thermoelectric Power.

The thermal conductivity of the InSb/NiSb eutectic was measured using the series comparative method of Stuckes and Chasmar.⁵⁵

A specimen in the shape of a rectangular block was formed into the central member of a seven layer stack as shown in Fig.16., This consisted of two identical upper and lower cylindrical parts in a copper, F/H steel, copper succession, on either side of the sample. The F/H steel layers, made from material supplied by Firth Brown Ltd., were alloyed to the copper layers in a permanent bond of negligible thermal resistance. The F/H steel layers then acted as standards of known thermal conductivity from which the relative value of the thermal conductivity of the sample could be calculated.

An insulated Nichrome heater, wound on a stainless steel former, was placed on top of the stack. A small pressure was applied to the heater by means of a low thermal conductivity steel ball and sliding bridge. The large copper base on which this assembly was mounted acted as a heat sink and drew preferentially downwards through the stack. When heat losses from the stack were equal to the heat supplied to the stack, by means of the heater an equilibrium state is achieved and steady temperature gradients are set up in each layer of the stack. These were measured using thermocouples 1→6 which were inserted in small holes drilled into the copper elements, near their boundaries. Accurate measurement of the position of each thermocouple in its layer enabled allowance to be made for the temperature drop between the thermocouple and the copper/steel or copper/sample interfaces.

Two copper leads, not shown in Fig.16, were attached to the copper layers near thermocouples 3 and 4. These were used to measure

Fig.16

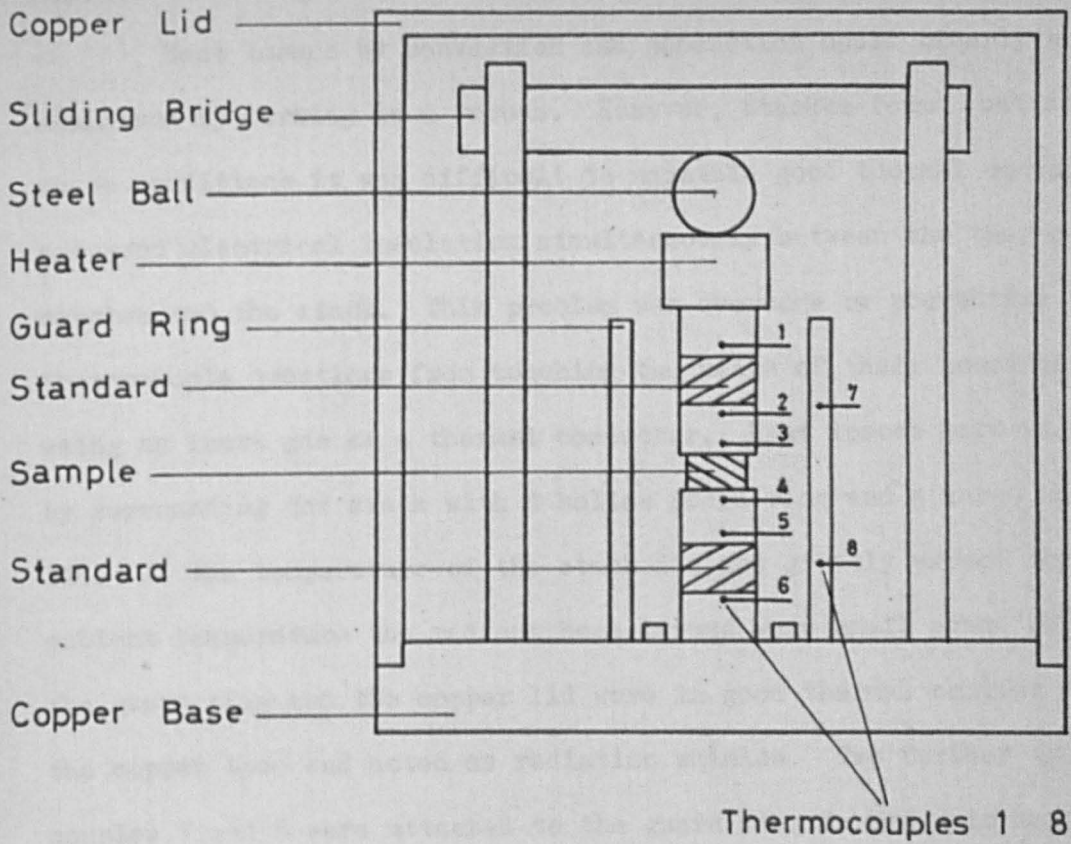
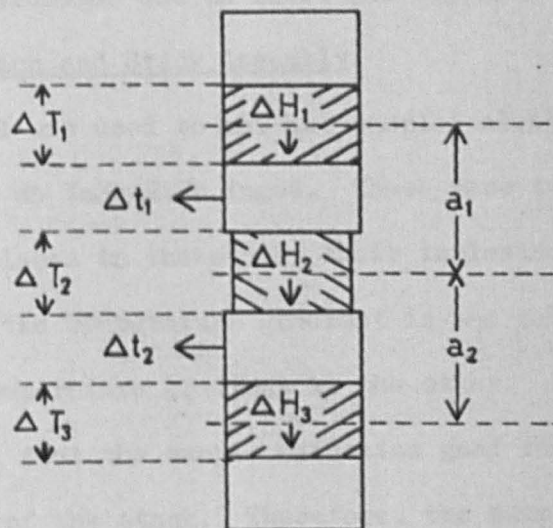


Fig.17



the thermoelectric voltage developed across the sample from the applied thermal gradient.

Heat losses by convection and conduction could clearly be minimised by working in a vacuum. However, Stuckes found that under these conditions it was difficult to maintain good thermal contact and good electrical insulation simultaneously between the thermocouples and the stack. This problem was overcome by preventing the thermocouple junctions from touching the walls of their housings and using an inert gas as a thermal conductor. Heat losses were reduced by surrounding the stack with a hollow guard ring and a large copper lid. If the temperature of the stack did not greatly exceed the ambient temperature the radiant heat losses were small since both the guard ring and the copper lid were in good thermal contact with the copper base and acted as radiation shields. Two further thermocouples 7 and 8 were attached to the guard ring in order to measure the ambient temperature.

The thermal conductivity apparatus described above was supported in a large capacity furnace fitted with a pumping system, a temperature control pyrometer and an inert gas supply.

4.1.2. Sample Preparation and Stack Assembly.

A slitting wheel was used to cut two samples along the principle directions of an InSb/NiSb ingot. These were such that when the samples were placed in the stack, their inclusion rods were orientated parallel to the temperature gradient in one case and perpendicular to the temperature gradient in the other. In this method, it is essential that the sample maintains good thermal contact with the other members of the stack. Therefore, the samples were ground flat, initially using fine carborundum powder with an iron lap and finally using optical grade aluminium oxide powder and a glass lap. The samples were then thoroughly cleaned with water, alcohol and

ether before being nickel plated. Nickel was used in preference to copper since the latter diffuses slowly into InSb on prolonged exposure to high temperatures. It was found, however, that the application of a very thin preliminary layer of copper greatly assisted the adhesion of the Nickel plating. After removing the plating from all save the top and bottom surfaces, the lengths, widths and thicknesses of the samples given in the above order were (0.766, 0.647, 0.218) cm. and (0.747, 0.675, 0.136) cm. respectively.

Using Baker's fluid and pure indium solder, the top and bottom surfaces of the samples were then "tinned" with a soldering iron. Similar grinding, cleaning and tinning processes were also applied to the copper faces which were placed adjacent to the sample in the stack. After washing off excess flux, the stack was assembled on a hot plate which was heated until the solder was again molten. The thermocouple holes were then aligned and the position of the sample was altered until it was co-axial with the stack. A small weight was then placed on top of the stack which was allowed to cool slowly with the hot plate.

The quality of the contacts produced in this way was assessed at room temperature by passing a known alternating current through the stack and measuring the alternating voltage produced between the copper layers bridging the sample, using a valve voltmeter. The resistance of the sample and its contacts was calculated by using Ohm's Law. From the previously measured resistivity and sample dimensions, the resistance of the sample was also calculated. A close correspondence between this and the above value suggested that good electrical contact, hence good thermal contact, had been attained.

Six Chromel-Alumel thermocouples, made of 0.005" wire were used in the stack and two further thermocouples were fitted into the

guard ring. The thermocouple wires were insulated from their housings by fine, double-bore alumina tubing placed near their welded hot junctions. Small lengths of single bore alumina tubing were then used on each separate wire, followed by woven glass sleeving which led to a glass/metal vacuum seal through which the wires passed. Copper leads were brazed to the other ends of the thermocouple wires to form the cold junctions of the thermocouple. Since the temperature differences between adjacent thermocouples were small, it was essential that the cold junctions of all the thermocouples were maintained at the same temperature. This was assured by deeply inserting the insulated cold junctions into equidistantly spaced holes drilled on a concentric radius of a massive copper cylinder. A mercury in glass thermometer was then used to determine the temperature of the cold junctions.

The output leads of the thermocouples were wired to a thermoelectric free multiway switch leading to a Diesselhorst type thermoelectric free potentiometer supplied with a galvanometer and photocell amplifier. This enabled the e.m.f.'s and differential e.m.f.'s of successive thermocouples to be measured. The measurements permitted the temperature drop across each layer to be determined with great accuracy and also allowed the average temperature of the layer to be measured at the same time.

The six hot junctions of the thermocouples, insulated from the copper housings by their alumina sleeving, were threaded just over half way through the stack. Small radial copper bolts were then used to fix the thermocouples in position. The six thermocouples used in the stack had been specially chosen from a large batch that had previously been calibrated. This had been done by annealing the thermocouples in a copper block similar to that used for the cold junction. Their voltage outputs were then recorded at various

temperatures when the furnace was in equilibrium. The six thermocouples giving closest agreement over the whole temperature range were then selected for use in the stack.

4.1.3. Measurement Procedure.

After evacuation, the furnace was sealed off and filled with nitrogen maintained at a pressure slightly greater than atmospheric pressure. The gas then communicated the temperature of the copper blocks to their respective thermocouples and also prevented sample oxidation.

An "Electroflo" temperature control pyrometer, which allowed the furnace to be preset to a given temperature and the stack heater were then switched on at the same time. When a state of thermal equilibrium was attained the direct and differential e.m.f.'s produced in the thermocouples were then measured to an accuracy of $0.1\mu\text{V}$. The readings were taken in ascending and descending order so that any slight variation of stack temperature could be taken into account. The heater was then switched off and the temperature was reset to the previously measured sample temperature. When thermal equilibrium was restored another series of readings was taken in the same manner. All thermocouples were observed not to read identically, partly due to the presence of a small thermal gradient down the stack and partly due to slight differences in calibration. The second series of readings constituted a set of "zero errors" by which the first series of readings was corrected. This correcting process was repeated at each temperature at which the thermal conductivity was measured, since the magnitude of the "zero errors" altered with temperature.

A similar correction was also applied to the thermoelectric power measurements so that the corrected thermoelectric voltage directly related to corrected thermal gradient from which it originated.

Room temperature measurements were taken before and after each

furnace run to check that the eutectic samples had not been changed by the thermal treatment and also to check that the indium contacts were still sufficiently good.

4.1.4. Theory of the Comparative Method.

An expression for the thermal conductivity of the sample is derived in the following manner. Let the sample and two standard layers of the stack have thermal conductivities, K , cross-sectional areas, A , and thicknesses t , which may be distinguished by the appropriate subscripts 1, 2 and 3, proceeding down the stack.

The application of a thermal gradient, ΔT , across each layer causes a flow of heat, ΔH , through the central plane of the layer as shown in Fig.17.

Let Δt_1 be the temperature difference between the average temperature of layers 1 and 2 and the surrounding temperature acquired by the guard ring. Further, let a_1 be the surface area between the centres of 1 and 2 and a_2 be the surface area between 2 and 3, and h be the heat loss per unit surface area per degree excess over the surrounding temperature. Then

$$\Delta H_1 = \Delta H_2 + a_1 h \Delta t_1,$$

$$\Delta H_2 = \Delta H_3 + a_2 h \Delta t_2 \text{ and}$$

$$\Delta H_1 = \Delta H_3 + (a_1 \Delta t_1 + a_2 \Delta t_2) h$$

$$\therefore \Delta H_2 = \Delta H_1 - a_1 \Delta t_1 \left[\frac{\Delta H_1}{a_1 \Delta t_1} - \frac{\Delta H_3}{a_2 \Delta t_2} \right]$$

From (2.55),

$$K = \frac{t \Delta H}{A \Delta T} \text{ giving}$$

$$K_2 = \frac{t_2}{A_2 \Delta T_2} \left\{ \frac{K A_1 \Delta T_1}{t_1} - a_1 \Delta t_1 \left[\frac{K A_1 \Delta T_1 / t_1}{a_1 \Delta t_1} - \frac{K A_3 \Delta T_3 / t_3}{a_2 \Delta T_2} \right] \right\} \quad (4.1)$$

For the eutectic samples, K_2 becomes K_{11} and K_1 for the respective cases of inclusion rods parallel and perpendicular to the temperature gradient ΔT_2 .

If the temperature gradient ΔT_2 , produces a corrected

thermoelectric voltage ΔV_2 , and the thermoelectric power of the copper is neglected, then the absolute thermoelectric power of the eutectic is given by

$$\alpha = \frac{\Delta V_2}{\Delta T_2} \quad (4.2)$$

The thermoelectric powers of the two samples are then denoted by $\alpha_{||}$ and α_{\perp} , according to the above convention.

4.1.5. Experimental Errors.

The absolute thermal conductivity of Armco Iron was measured by Powell at the N.P.L. up to 720^oK. Identical material was used by Stuckes to form the standards necessary for comparative measurement of the thermal conductivity of F/H steel, over the same range. The values obtained were compared with the absolute thermal conductivities also obtained by Powell from a material of the same composition and heat treatment as F/H steel. Agreement was obtained to 1%. However, since the experimental error in Powell's measurements was of order 2%, a similar error must be assigned to the thermal conductivities obtained by Stuckes. As the same F/H steel was used to form the standards of the present apparatus, their thermal conductivities are taken from Powell's results and are subject to a 2% error.

Errors estimated at 1% also appear due to the sample dimensions and the errors in temperature measurement, so that an overall error of 3% may be present in both $K_{||}$ and K_{\perp} .

The absolute thermoelectric power of the eutectic was deduced by ignoring the absolute thermoelectric power of the copper in the copper-eutectic system. This introduces an error of order 2% in the measured values of $\alpha_{||}$ and α_{\perp} .

CHAPTER 5.

5.1. STEREOSCAN ELECTRON MICROSCOPY

5.1.1. Structure of InSb/NiSb.

On completing the thermal measurements the two samples of InSb/NiSb were cleaned and polished with diamond grit. After etching the polished surfaces for a short time with a concentrated mixture of nitric acid, hydrochloric acid and acetic acid, the samples were mounted and placed in a Stereoscan Electron Microscope. A series of photographs at various magnifications was then taken, showing sections of InSb/NiSb perpendicular and parallel to the growth direction.

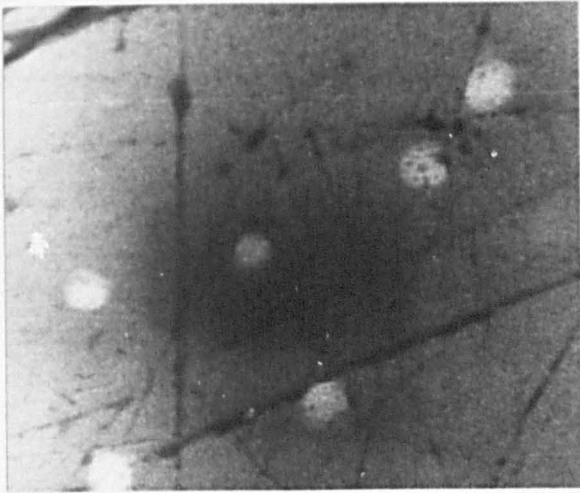
In plate 4 the roughly circular transverse cross sections of the NiSb inclusions are contrasted against the darker background of the InSb matrix. In plate 5 the longitudinal cross-sections of the inclusions are similarly contrasted against the background matrix.

These photographs clearly show that the inclusions are rod-like in appearance and that the lengths and diameters of the rods varied appreciably. Further low magnification photographs enabled the distribution curves shown in Fig.18 to be plotted. The average length and diameter of the inclusions was established to be 2.20μ and 0.72μ respectively. Using this information and matching the photographs, the ratio of inclusion volume fraction/matrix volume fraction has been estimated at 0.008. Since, however, the photographs showed that the separations of the rods was not regular and also that the density of rods altered considerably over the sample so that this figure is an order of magnitude value. This clearly implies that the volume fraction of NiSb is not necessarily the same for all samples extracted from the InSb/NiSb ingot.

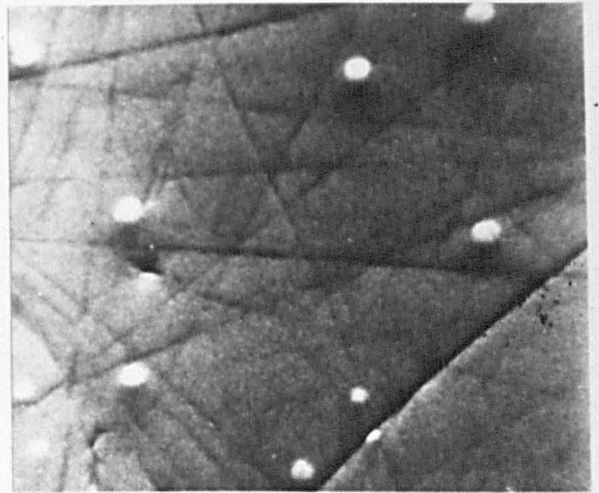
The microstructure described above differs in several respects from the microstructures drawn from various melts, by Wilhelm and Weiss. They found that a sample drawn from a melt of 3% NiSb and

Plate 4.

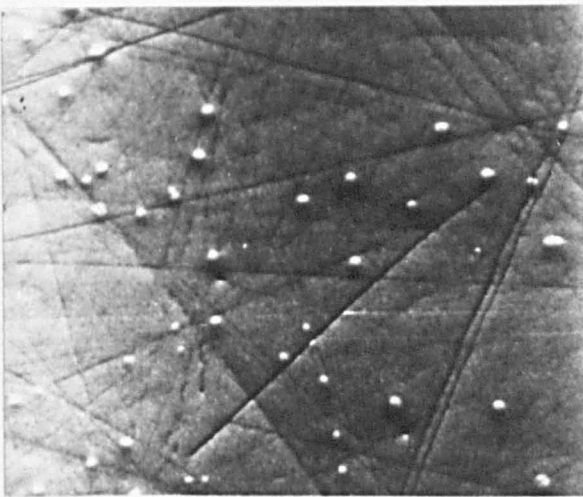
Sections of InSb/NiSb perpendicular to the growth direction, at various magnifications.



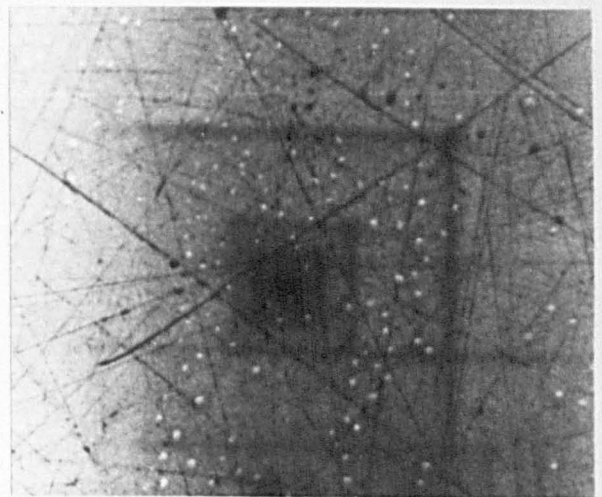
X 7100



X 5500



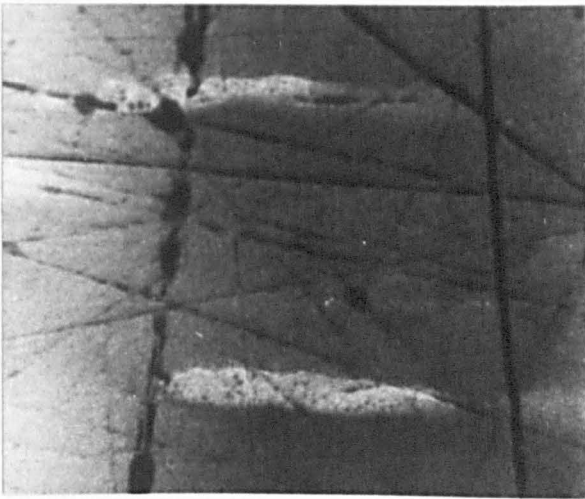
X 2200



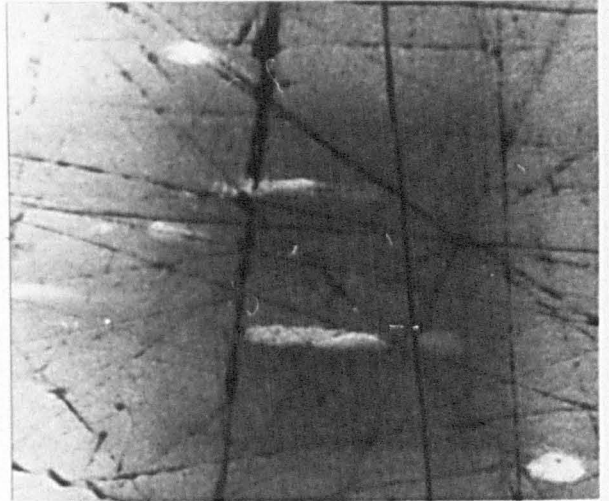
X 1200

Plate 5.

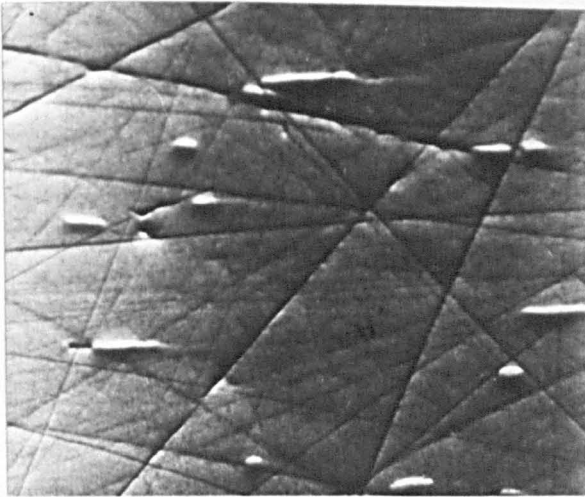
Sections of InSb NiSb parallel to the growth direction, at various magnifications.



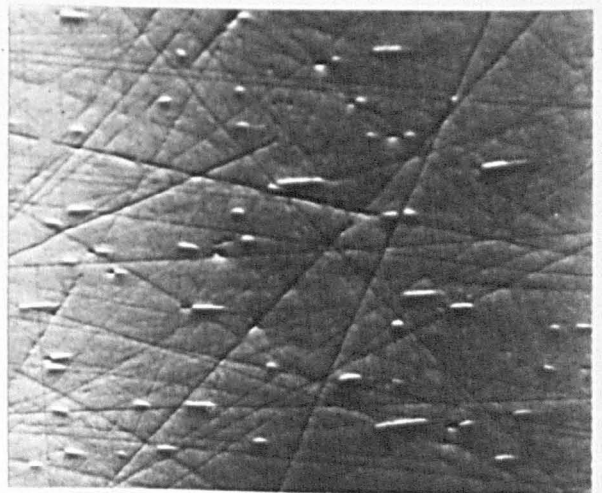
X 6700



X 3500



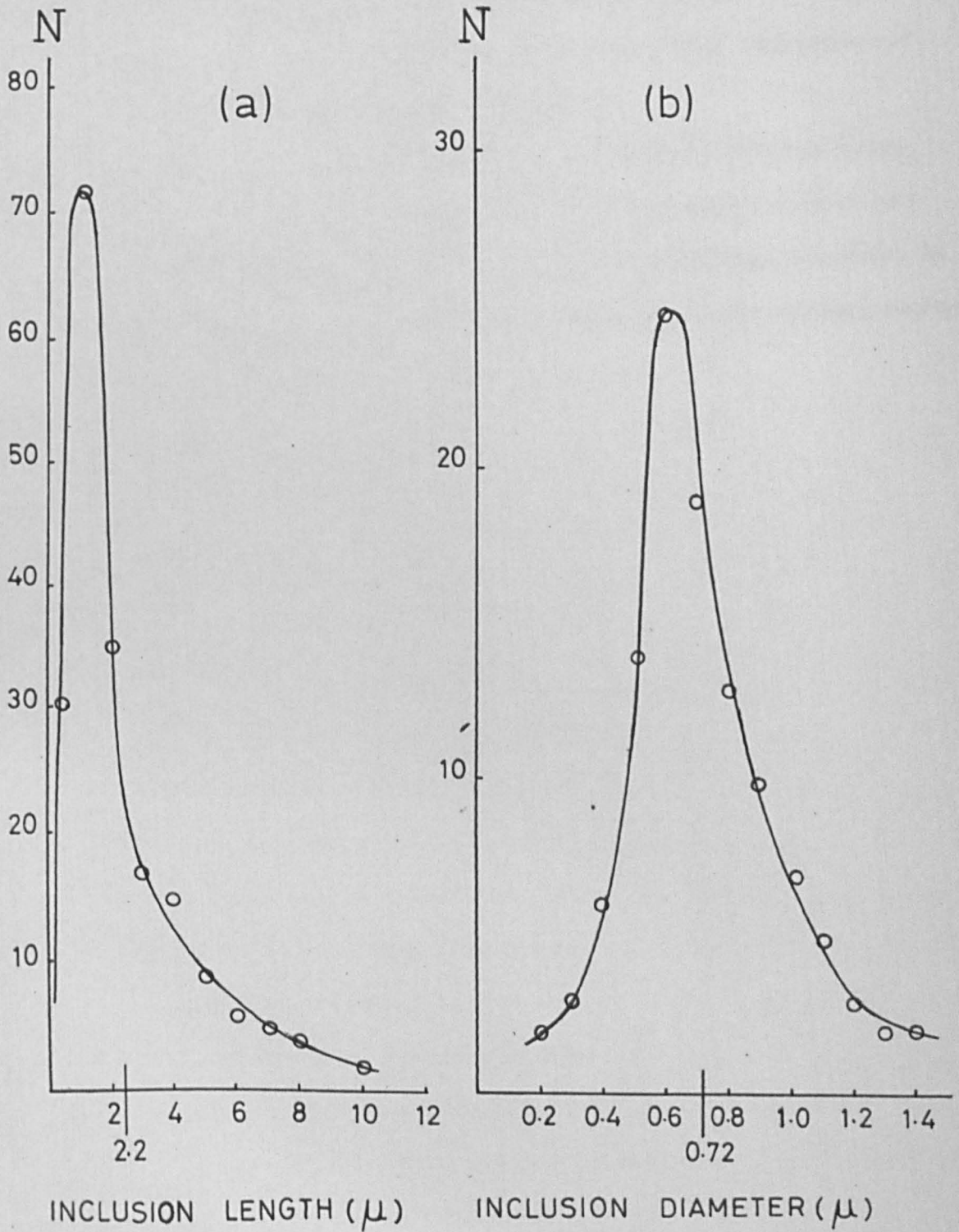
X 1340



X 670

Fig.18

NUMBER OF INCLUSIONS, N . v. (a) INCLUSION LENGTH
(b) INCLUSION DIAMETER



97% InSb by weight, possessed coarse grained crystallites of NiSb in addition to a fine grained microstructure of InSb/NiSb. Samples containing as little as 0.3%, by weight, may be formed in this way. They also found that a very uniform fine grained eutectic microstructure could be obtained from a melt of 98.2% InSb and 1.8% NiSb, by weight. This material contained regularly placed inclusions of average length 50μ and average diameter 1μ .

The ingot of InSb/NiSb used in the present work was drawn, from a melt of the latter proportions, at a pulling rate of $\frac{1}{2}$ " per hour. Since, however, the pulling rate used by Wilhelm and Weiss is unpublished, the reasons for the differences in microstructure cannot be assessed.

CHAPTER 6

6.1. Electrical Properties of InAs.

The Hall coefficient of the InAs sample, shown in Fig.19 remains negative over the complete range of measurement and indicates that donor impurities are present. If the concentration of donor atoms present is N_D and all donors are ionised, then in the mixed conduction range $c = n/p = (N_D + n)/p$. Substitution of this expression into equations (2.25) and (2.28), remembering that InAs, like InSb, has a high mobility ratio, the equations (6.1) and (6.2) are obtained.

$$R_H = -1/(N_D + n)e \quad (6.1)$$

$$\sigma = (N_D + n)e\mu_e \quad (6.2)$$

In the extrinsic range $N_D \gg n$ so that the Hall coefficient takes a constant value given by $R_H = -1/N_D e$. Fig.19 clearly shows that the sample is extrinsic at and below room temperature and that $N_D = 1.40 \times 10^{16}$ donors/cc.

At very high temperatures in the intrinsic range $n, p \gg N_D$, so that $R_H = -1/ne = -1/n_i e$. The variation of intrinsic carrier concentration with temperature may, therefore, be deduced from the temperature dependence of R_H and from this the energy gap, E_g , at absolute zero, may be calculated. Following this procedure a value of $E_g = 0.44$ eV was found from the present measurements. This is in reasonably good agreement with the value of (0.47 ± 0.02) eV. obtained by Folberth, Madelung and Weiss.⁵⁷

The electrical conductivity of the InAs sample, as shown in Fig.20, falls slightly from the lower temperature values. Over this range of temperature, $\sigma = N_D e \mu_e$ and the reduction in electrical conductivity arises directly from the reduction in electron mobility.

Equations (6.1) and (6.2) show that the electron mobility is given by $\mu_e = R_H \sigma$ at all temperatures. The experimental plot of $\mu_e v T$

Fig. 19

HALL COEFFICIENT (R_H) V TEMPERATURE (T)

FOR InAs

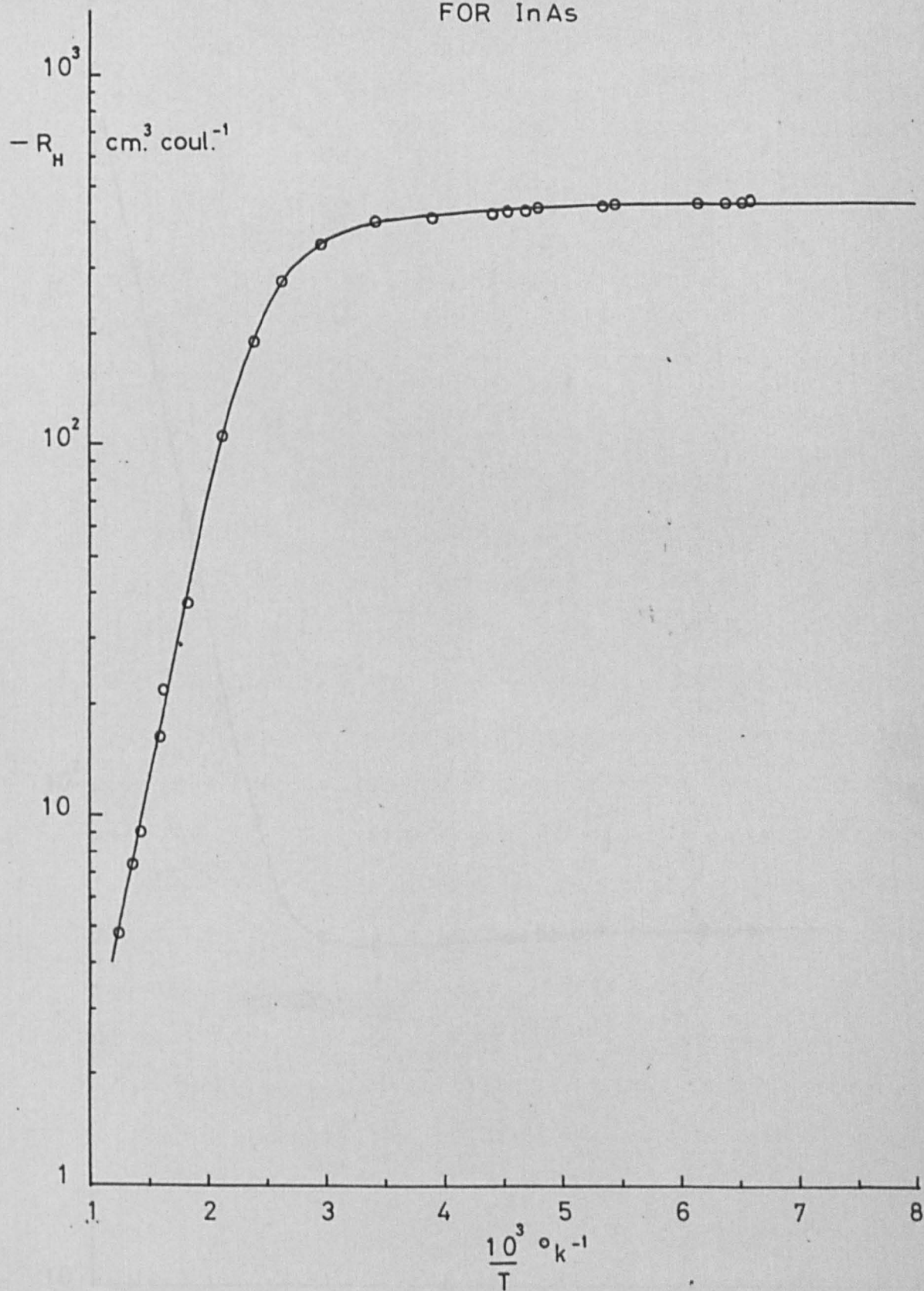
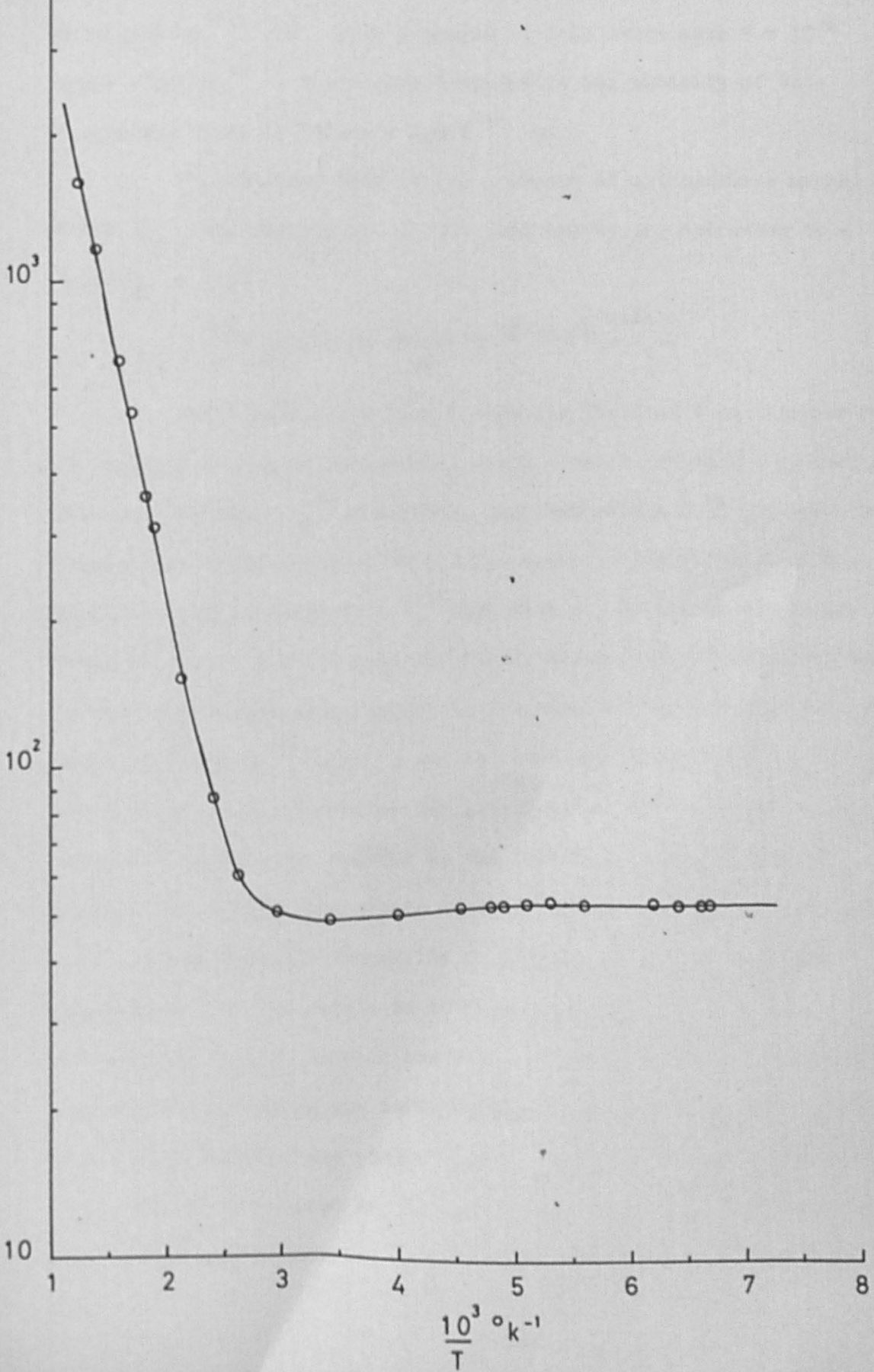


Fig. 20

ELECTRICAL CONDUCTIVITY (σ) V TEMPERATURE (T)
FOR InAs

σ $\Omega^{-1} \text{cm}^{-1}$



based on this equation is given in Fig.21. The value of the room temperature mobility is shown to be 20,00 cm.² V⁻¹.s⁻¹. Above room temperature the mobility follows an approximately $\mu_e \propto T^{-1.0}$ relation. Chasmar has recorded a similar room temperature mobility of 21,000 cm.² V⁻¹.s⁻¹ with a sample of InAs containing 5 x 10¹⁶ donor atoms cm.⁻³. Above room temperature the mobility of this sample was found to follow a $\mu_e \propto T^{-1.1}$ law.

Fig.22 shows that in the presence of a transverse magnetic field, B_z, the resistivity of the InAs sample, ρ, increases to a value ρ_B, so that

$$\rho_B \frac{\rho - \rho}{\rho} = \frac{\Delta \rho_B}{\rho} = 0.114 B_z^{1.64}$$

This graph shows that a magnetic field of 7 Kg produces a 7% increase in sample resistance. Using a sample of aspect ratio 8, Chasmar obtained a B_z^{1.65} dependence, together with a 1.2% increase in sample resistance measured in a 7 Kg. magnetic field. Weiss also confirmed the presence of a B_z^{1.65} law with a 1.4% change in sample resistance in a similar magnetic field. Weiss also demonstrated that by moving the resistance probes to the ends of the sample, (of aspect ratio 25) the B_z^{1.65} relation was retained and the increase in resistance was 8%. Therefore, it is suggested that most of the 7% change in resistance observed in the present measurements is of geometrical origin. The aspect ratio of the sample used in this work was 6. Since InAs has a mobility of 20,000 cm.² V⁻¹.s⁻¹ at room temperature and the sample is extrinsic, it cannot be regarded as an extended sample. Weiss's sample of aspect ratio 25 must, however, approximate better to the infinitely extended case, so that the 6% discrepancy between the present measurements and those of Chasmar and Weiss can be attributed to the sample geometry. The theoretical basis of the B^{1.65} dependence is, however, not understood at present.

Fig. 21

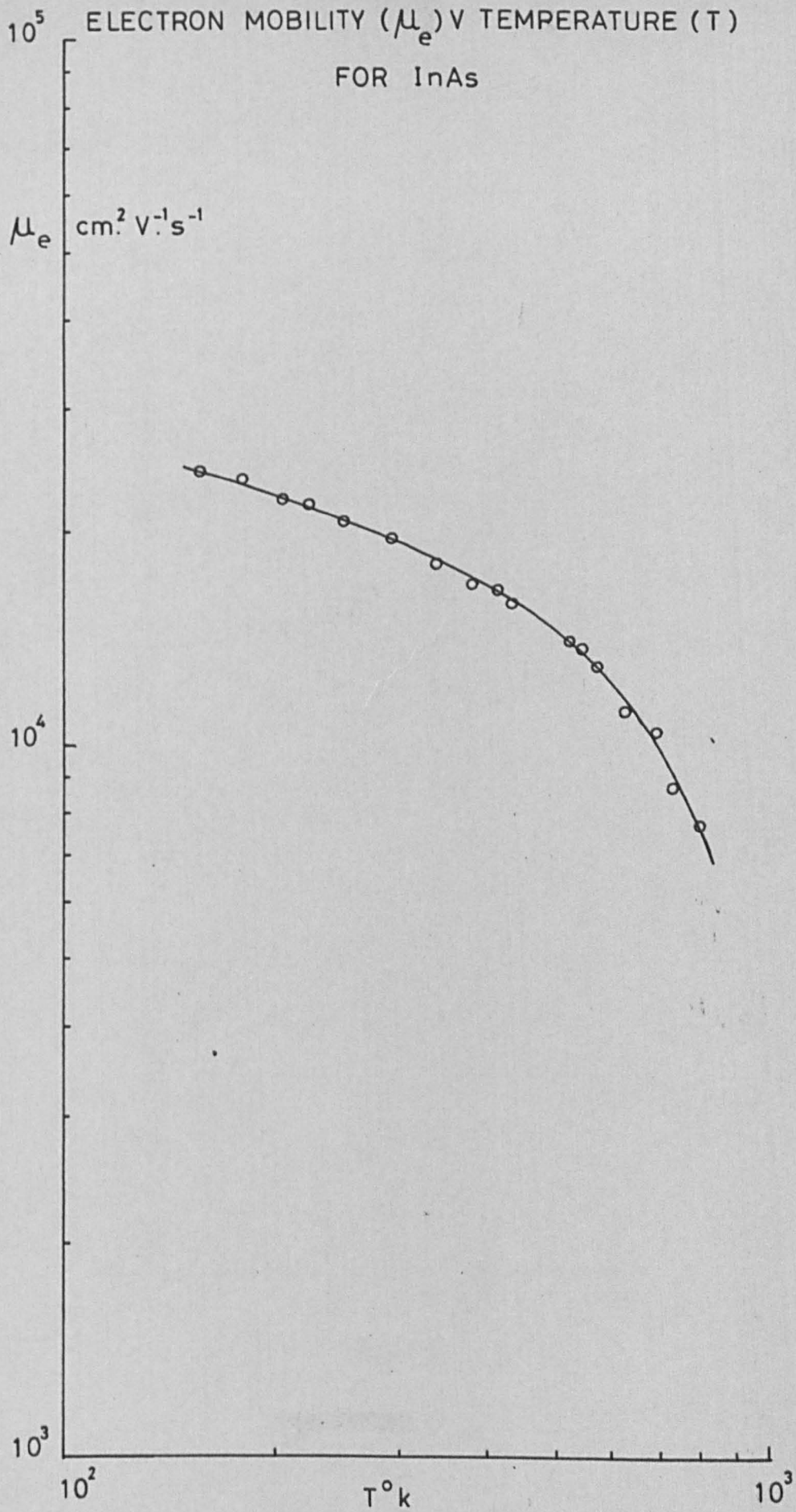
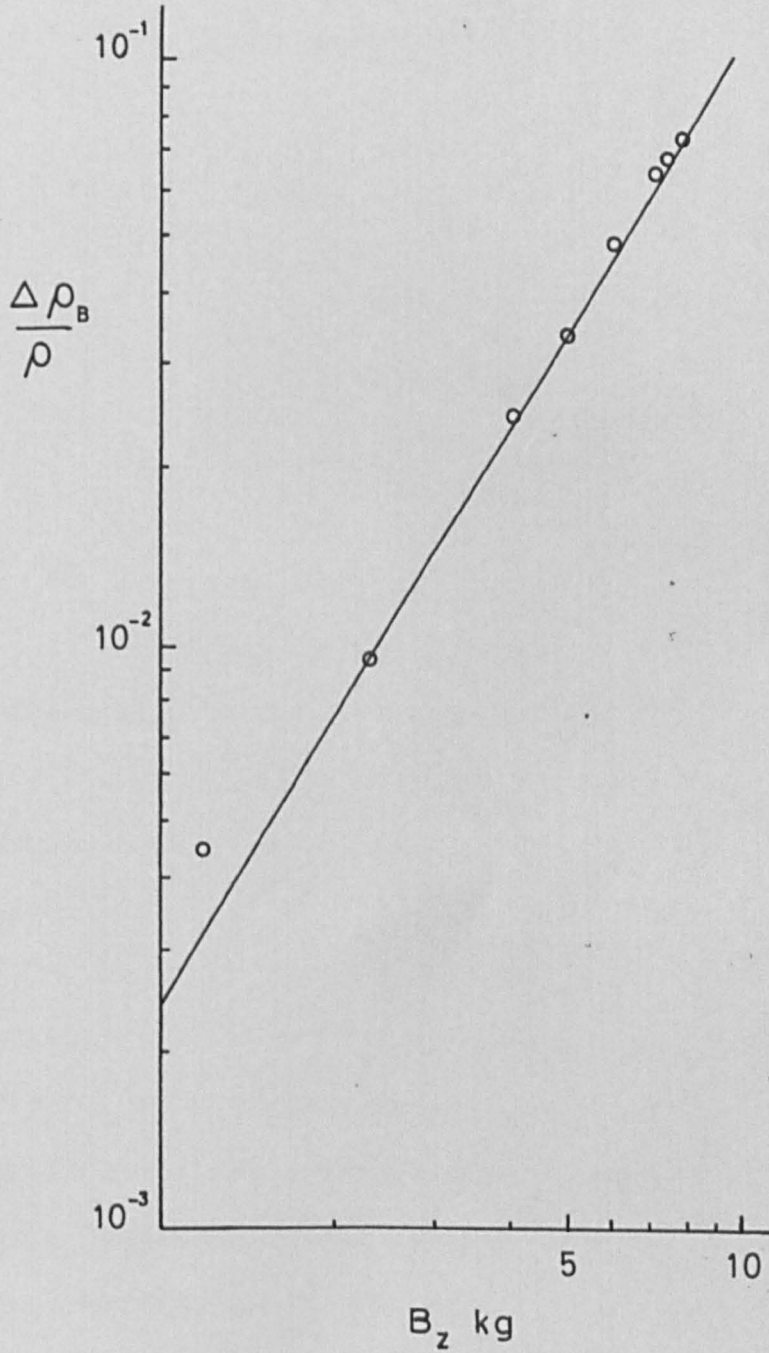


Fig. 22

CHANGE IN RESISTIVITY $\left(\frac{\Delta \rho_B}{\rho}\right)$ V MAGNETIC FIELD (B_z)
RESISTIVITY

FOR InAs AT 21°k



The agreement between the present results on InAs and results published by other workers, however, suggests that the sample holder, furnace and cryostat are all functioning correctly.

Sample	1	2	3
Resistance (Ω)	1	1	1
ρ (Ω-cm)	24	27	24
ρ (Ω-cm)	27	24	27
ρ (Ω-cm)	24	27	24

4. Discussion

In samples 1 and 2 only present calculations have the perpendicular to the direction of current flow, their calculated resistivity values are nearly the same. However, in sample 3, the value of ρ is 27 Ω-cm, the same value for sample 1, which is calculated.

Sample 3, in which the direction of the parallel to the direction of current flow, calculated resistivity is 24 Ω-cm, which is nearly the same as ρ . This agreement in calculated resistivity values, which are of the order of 10% being stated, are by the likely occurrence of the following. Effectively, such an agreement will be a function of the resistivity of the material, which is a function of the temperature of the sample. The value of the resistivity of the material is a function of the

CHAPTER 7

INTERPRETATION OF EXPERIMENTAL RESULTS.

7.1. Electrical Properties of InSb/NiSb.

The room temperature (294°K) parameters are summarised in Table 7.1 below. They provide a useful reference in discussing the directional anisotropies of the electrical conductivity, Hall coefficient and "magnetoresistance" behaviour of samples 1, 2 and 3.

TABLE 7.1.

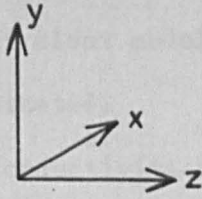
Sample	1	2	3
Orientation (x)	A	B	C
$\sigma \ \Omega^{-1}\text{cm}^{-1}$	214	210	256
$R_H^x \ \text{Coul}^{-1}\text{cm}^3$	327	190	223
$r_x \ (7.3 \ \text{Kg.})$	1.44	9.25	2.84

7.1.1. Electrical Conductivity.

As samples 1 and 2 both possess inclusions that lie perpendicular to the direction of current flow, their electrical conductivities should, in theory, be identical. Therefore, an average value of σ_1 of $212 \ \Omega^{-1}\text{cm}^{-1}$ has been taken for purposes of calculation.

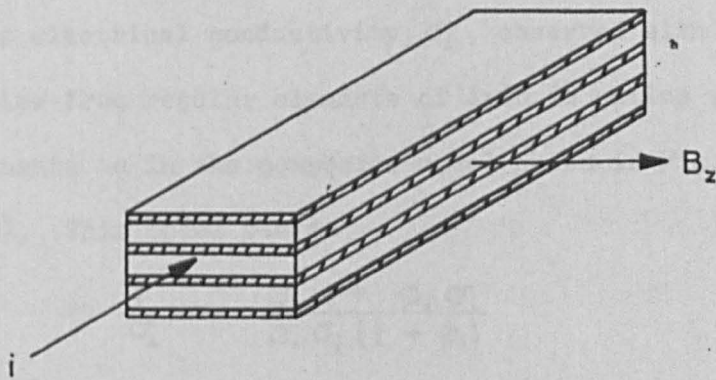
Sample 3, in which the inclusions lie parallel to the direction of current flow, possesses an electrical conductivity, σ_u , of $256 \ \Omega^{-1}\text{cm}^{-1}$ which is considerably greater than σ_1 . This improvement in electrical conductivity emerges through part of the InSb matrix being shorted out by the highly conducting NiSb inclusions. Theoretically, such an improvement could be attained by adding a small amount of NiSb in parallel to a sample of pure InSb, so that a parallel combination of resistors is formed as shown in Fig.23(a). If the ratio of the volume of inclusions to the volume of matrix

Fig.23



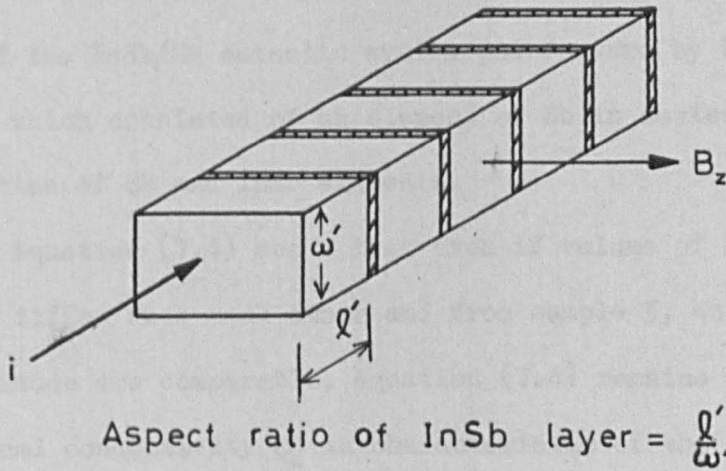
(a)

SAMPLE 3 IN ORIENTATION C



(b)

SAMPLE 2 IN ORIENTATION B



is ψ , then a smaller volume ratio, ϕ_1 , is necessary to produce by means of this simple equivalent model, in which matrix-inclusion-matrix current flow is eliminated.

If the electrical conductivities of InSb and NiSb are σ_i and σ_N respectively, then for sample 3,

$$\sigma_{||} = \frac{\sigma_i}{1 + \phi_1} + \frac{\sigma_N \phi_1}{1 + \phi_1} \quad (7.1)$$

For $\phi_1 \ll 0.02$

$$\sigma_{||} \approx \sigma_i + \sigma_N \phi_1 \quad (7.2)$$

The other electrical conductivity, σ_{\perp} , observed with samples 1 and 2 may arise from regular elements of InSb in series with very thin NiSb elements as in the composite model shown in Fig.7 and in Fig.23(b). This model yields

$$\frac{1}{\sigma_{\perp}} = \frac{\sigma_N + \phi_1 \sigma_i}{\sigma_N \sigma_i (1 + \phi_1)} \quad (7.3)$$

Putting $\sigma_N/\sigma_i = M$, this gives

$$\sigma_{\perp} = \frac{\sigma_i (1 + \phi_1)}{(1 + \phi_1/M)}$$

For $\phi_1 \ll 0.02$ and $M > 10$

$$\sigma_{\perp} = \sigma_i (1 + \phi_1) \approx \sigma_i \quad (7.4)$$

This is essentially the same result as that obtained from the model of the InSb/Sb eutectic system put forward by Liebmann & Millar, which consisted of an element of Sb in series with a parallel combination of Sb and InSb elements.

Equation (7.4) shows that even if volume of NiSb in samples 1 and 2 differ from each other and from sample 3, so long as the orders of magnitude are comparable, equation (7.4) remains true, so that the electrical conductivity σ_{\perp} is characteristic of the InSb matrix.

From (7.2) and (7.4),

$$\frac{\sigma_{||}}{\sigma_{\perp}} \approx 1 + M\phi_1 \quad (7.5)$$

Equation (7.5) links the two principal electrical conductivities obtainable by the addition of a small amount of unidirectionally orientated inclusions of NiSb to InSb.

The experimentally obtained electrical conductivities of InSb/NiSb samples 1, 2 and 3 are shown in Fig.24. The two values of σ_{\perp} were observed to fall progressively, even when the temperature was reduced below 100°K. This reduction in electrical conductivity occurs as a result of the removal of intrinsic carriers. The electrical conductivity of semiconductors generally, however, reaches a minimum value and then starts to increase when the temperature is lowered into the extrinsic range. The increase in electrical conductivity arises from the increase in carrier mobility that occurs when ionised impurity scattering replaces lattice scattering as the dominant scattering mechanism. An electrical conductivity of similar temperature dependence to that observed with InSb/NiSb samples 1 and 2 (i.e., σ_{\perp}) below 100°K, has, however, been reported by Putley⁶¹ from work carried out on a sample of InSb containing 2×10^{15} acceptors cm^{-3} .

The electrical conductivity of sample 3, namely σ_{\parallel} , coincided with σ_{\perp} at very high temperatures but diverged to a much higher value as the temperature was lowered. This can be explained using equation (7.5) by calculating the ratio M using electrical data for NiSb published by Wagini for the range 100°K to 500°K, extrapolating up to 528°K and assuming (7.4) to be true. From the values of M, σ_{\perp} and σ_{\parallel} , the most appropriate value of ϕ_1 may be deduced for the range above room temperature. A set of theoretical values for σ_{\parallel} may then be calculated as in Table 7.2.

Fig. 24

ELECTRICAL CONDUCTIVITY (σ) V TEMPERATURE⁻¹ (T⁻¹)
FOR InSb/NiSb

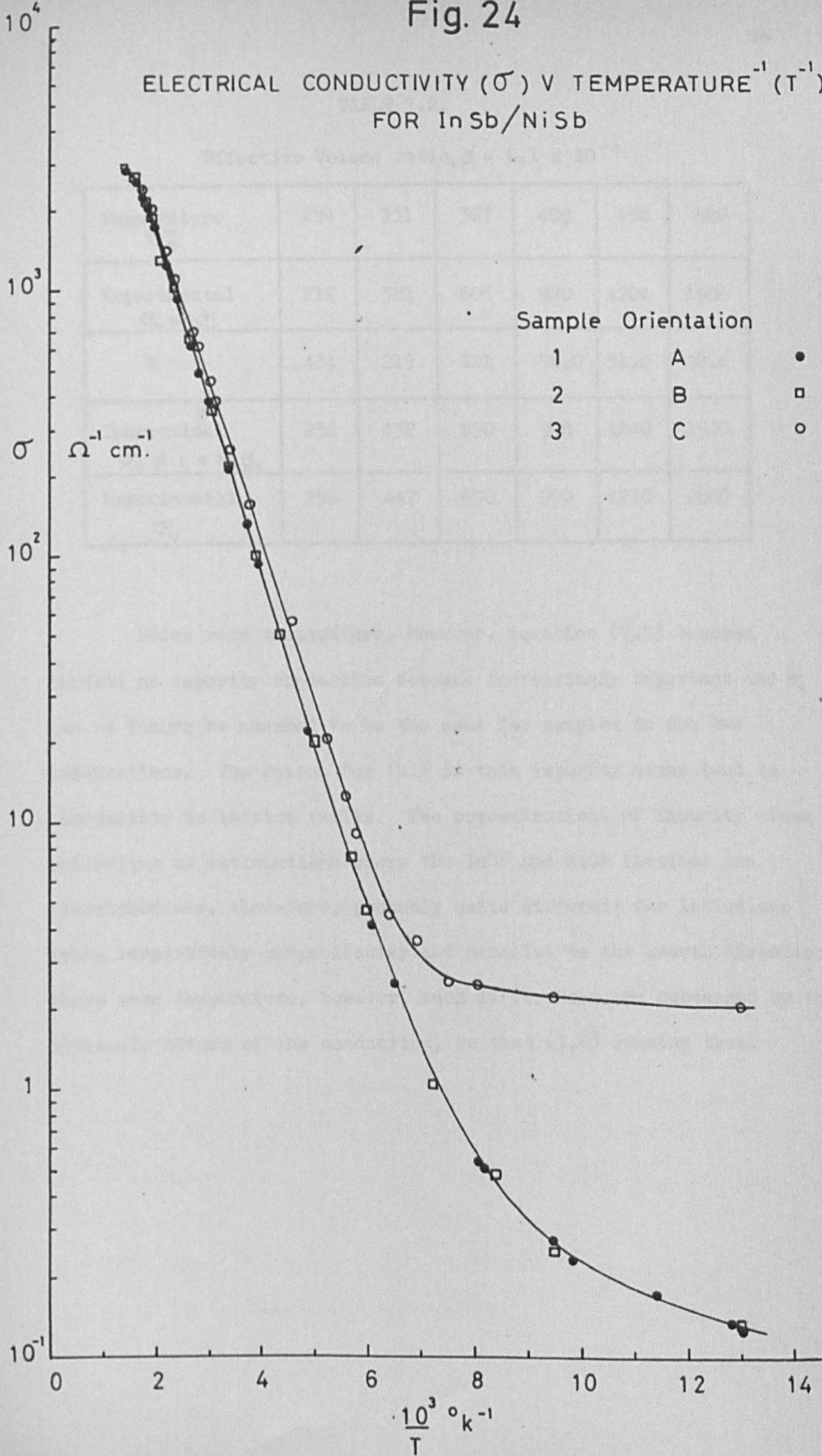


TABLE 7.2.

Effective Volume ratio, $\phi_i = 6.1 \times 10^{-4}$

Temperature $T^{\circ}\text{K}$	294	331	367	409	450	528
Experimental $\sigma_{\perp} \approx \sigma_i$	212	381	605	920	1204	1906
M	434	219	121	76.0	51.0	28.6
Theoretical $\sigma_{\parallel} \approx 1 + M\phi_i$	256	432	650	970	1240	1940
Experimental σ_{\parallel}	256	447	690	950	1270	2000

Below room temperature, however, equation (7.5) becomes invalid as impurity conduction becomes increasingly important and σ_i can no longer be assumed to be the same for samples in the two orientations. The reason for this is that impurity atoms tend to accumulate in lattice faults. The concentrations of impurity atoms collecting at dislocations where the InSb and NiSb lattices are mismatched are, therefore, probably quite different for inclusions lying respectively perpendicular and parallel to the growth direction. Above room temperature, however, such differences are submerged by the intrinsic nature of the conduction, so that (7.4) remains true.

7.1.2. Hall Coefficient.

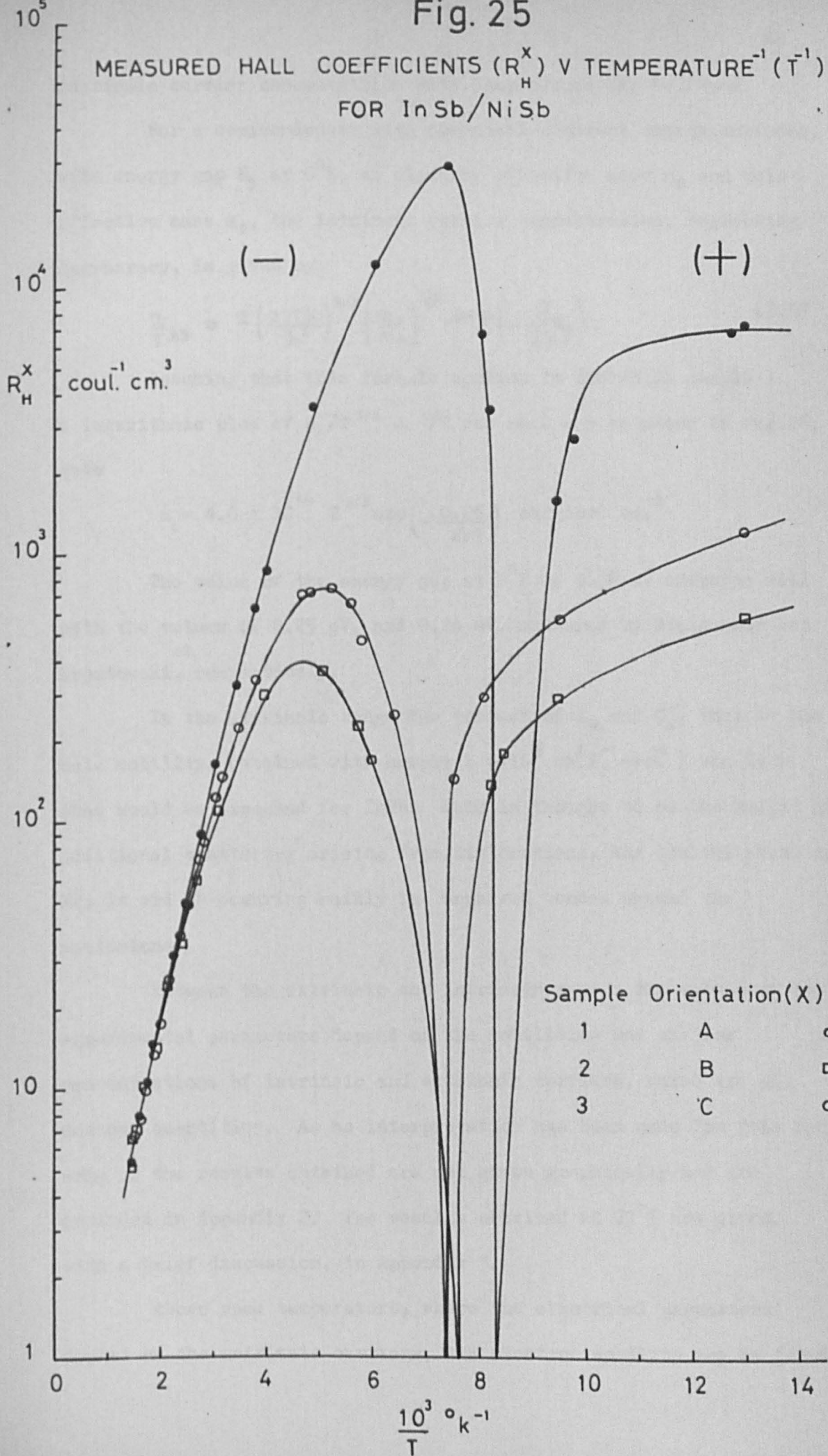
At low temperatures the Hall Coefficients of all three samples of InSb/NiSb, R_H^A , R_H^B and R_H^C , take values which differ radically with orientation, as shown in Fig.25. The Hall coefficient measured with sample 1 in orientation A was observed to change sign at a lower temperature than either sample 2 in orientation B, or sample 3 in orientation C, suggesting that it was the purest sample. This figure also shows that the inclusion rods in samples 2 and 3 cause substantial shorting of the Hall voltage. As the temperature increased, however, and σ_i approaches σ_n , less shorting was present and the values of R_H^A , R_H^B and R_H^C tended to converge.

Bearing these conclusions in mind, it is clear that the results obtained from sample 1 in orientation A are most characteristic of the InSb matrix. Since the aspect ratio of this sample is approximately eight, then in the intrinsic range, the sample approximates to the extended case. Therefore, $G(\ell/\omega, \theta_m) = 1$ and $R_H^A = R_H$, the Hall coefficient of the InSb matrix. Henceforth, R_H^A and R_H are regarded as synonymous, the low field value being taken for purposes of calculation, as this represents the case of minimal current distortion in sample 1 (See 2.2.8). Following this procedure makes little difference, however, as the Hall coefficient varies little with magnetic field as shown by Figs. 28(a) to 31(a).

Using equation (2.26) and the extrinsic Hall coefficient at 77°K the acceptor concentration $N_A = 10^{15-3} \text{ cm}^{-3}$ was deduced. Substitution of the low field Hall coefficient into equation (2.32) allows the electron concentration, n , to be deduced at any temperature in the intrinsic range. Since $c = n/p = n/(n + N_A)$, the concentration ratio can also be calculated. Further, as $n_i = n/\sqrt{c}$, the variation of

Fig. 25

MEASURED HALL COEFFICIENTS (R_H^X) V TEMPERATURE⁻¹ (T^{-1})
FOR InSb/NiSb



intrinsic carrier concentration with temperature can be found.

For a semiconductor with spherical constant energy surfaces, with energy gap E_g at 0°K , an electron effective mass m_e and hole effective mass m_p , the intrinsic carrier concentration, neglecting degeneracy, is given by

$$\frac{n_i}{T^{3/2}} = 2 \left(\frac{2\pi k}{h^2} \right)^{3/2} \left(\frac{m_e}{m_p} \right)^{3/2} \exp\left(-\frac{E_g}{2kT}\right) \quad (7.6)$$

Assuming that this formula applies to InSb/NiSb sample 1 a logarithmic plot of $n_i/T^{3/2}$ v. $1/T$ was made and as shown in Fig.26, gave

$$n_i = 4.8 \times 10^{14} T^{3/2} \exp\left(-\frac{0.26}{2kT}\right) \text{ carriers cm.}^{-3}$$

The value of the energy gap at 0°K of 0.26 eV compares well with the values of 0.25 eV. and 0.26 eV. measured by Steigmeier and Hrostowski, respectively.

In the extrinsic range the product of R_H and σ_L , that is the hole mobility, obtained with sample 1 ($\sim 10^3 \text{ cm}^2 \cdot \text{V}^{-1} \cdot \text{sec}^{-1}$) was less than would be expected for InSb. This is thought to be the result of additional scattering arising from dislocations, and ionised atoms of Ni, In and Sb occurring mainly in unpaired bonds, around the inclusions.

Between the extrinsic and intrinsic ranges the values of the experimental parameters depend on the mobilities and carrier concentrations of intrinsic and extrinsic carriers, which are all unknown quantities. As no interpretation has been made for this range, some of the results obtained are not given graphically but are included in Appendix 2. The results obtained at 77°K are given, with a brief discussion, in Appendix 3.

Above room temperature, where the electrical parameters depend on the intrinsic carriers, the electron mobility may be found

Fig. 26

INTRINSIC CARRIER CONCENTRATION ($n_i T^{-3/2}$) V TEMPERATURE⁻¹ (T^{-1})
 TEMPERATURE^{3/2}

FOR InSb/NiSb

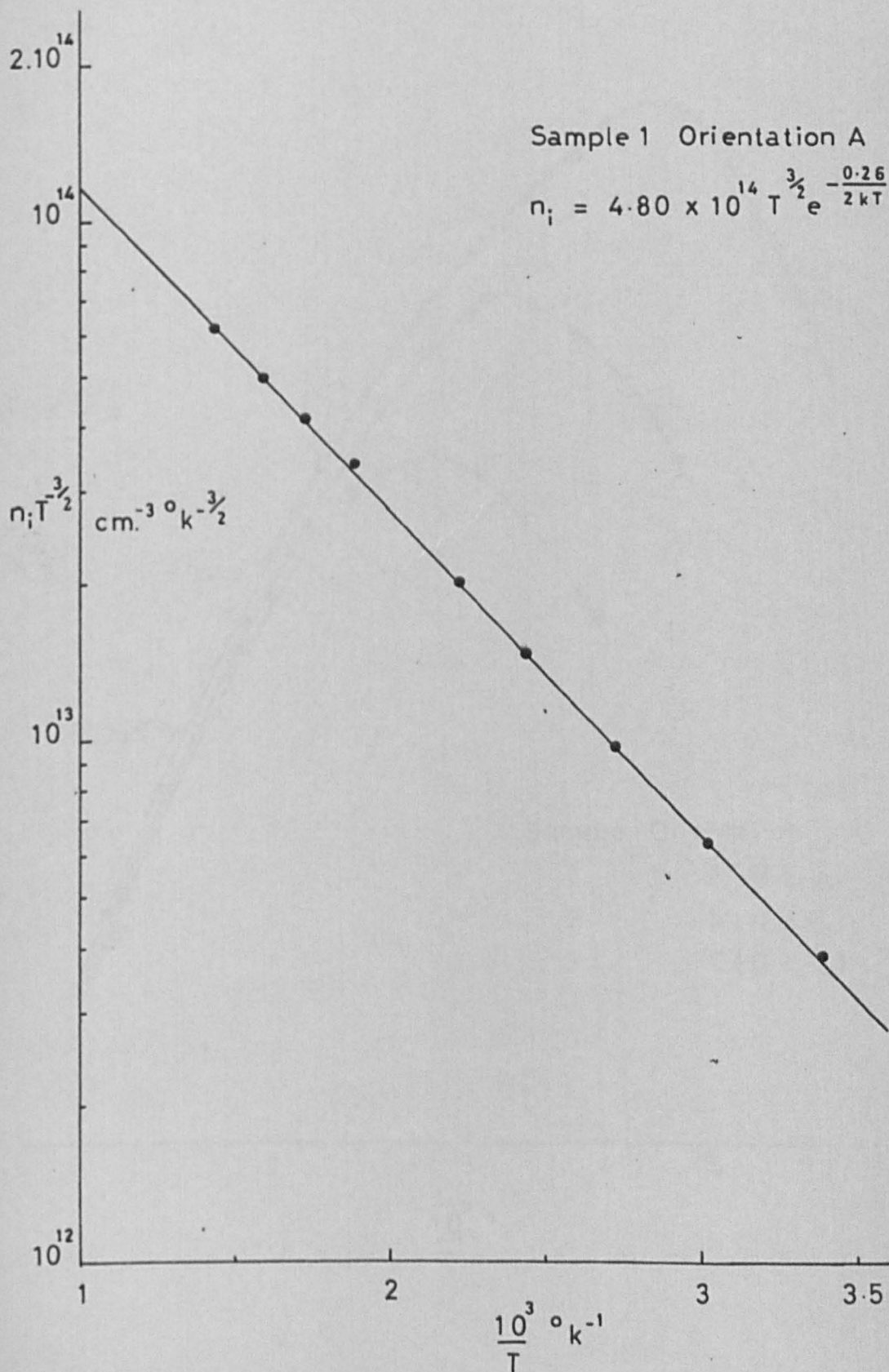
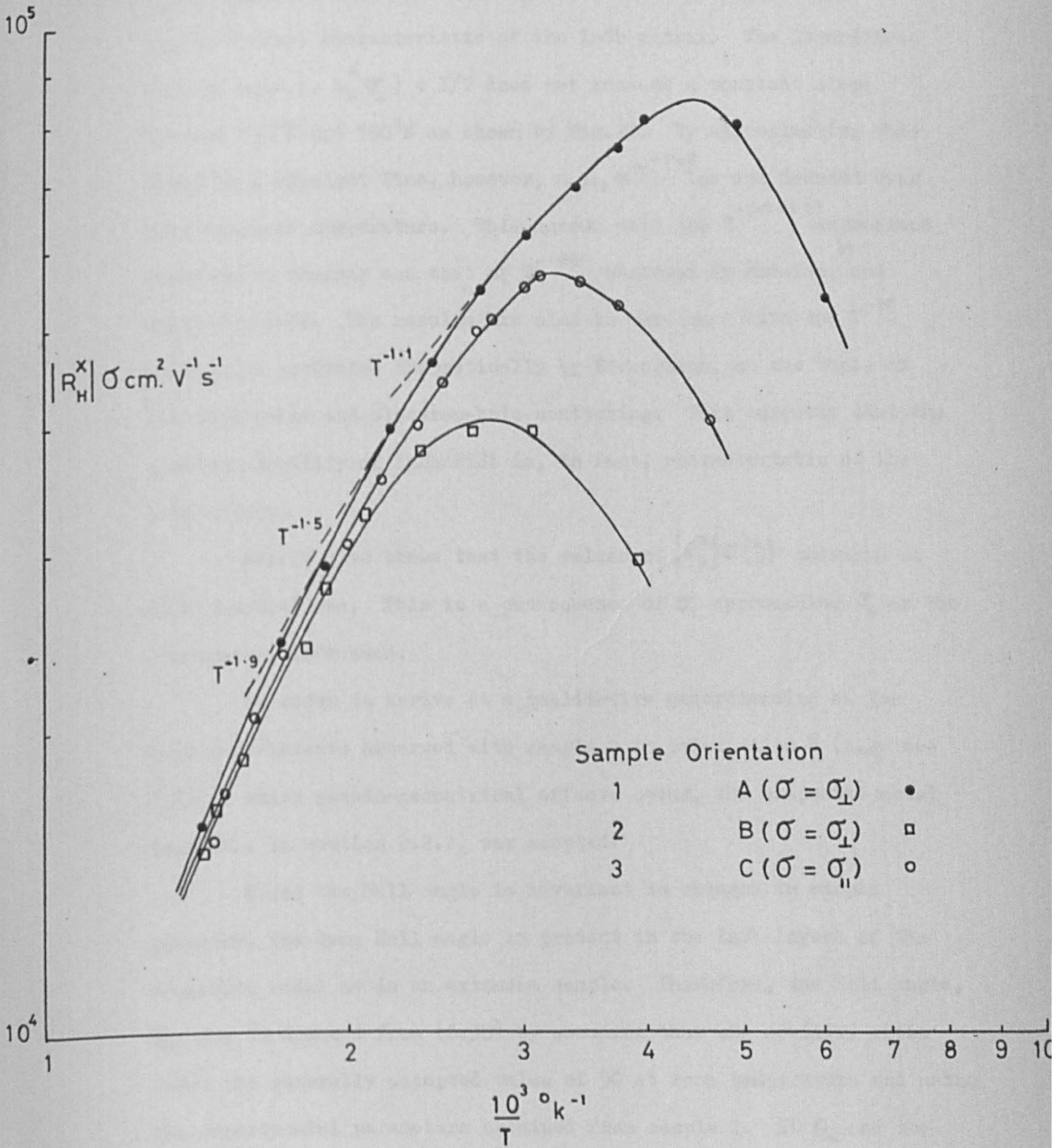


Fig. 27

$|R_H^x| \sigma \nu T^{-1}$
FOR InSb/NiSb



from equation (2.33). From the previous discussion of Hall coefficient and electrical conductivity it follows that this equation may only be applied to sample 1 in orientation A, so that $R_H^A \sigma_1 = \mu_e$, the electron mobility of InSb/NiSb, and that μ_e is, in theory, characteristic of the InSb matrix. The logarithmic plot of μ_e (i.e. $R_H^A \sigma_1$) v $1/T$ does not possess a constant slope between 290°K and 700°K as shown by Fig.27. By approximating this curve to a straight line, however, a $\mu_e \propto T^{-1.68}$ law was deduced over this range of temperature. This agrees with the $T^{-(1.7 \sim 1.8)}$ dependence observed by Chasmar and that of $T^{-1.66}$ observed by Madelung and Weiss for InSb. The results are also in agreement with the $T^{-1.7}$ dependence predicted theoretically by Ehrenreich, on the basis of combined polar and electron-hole scattering. This suggests that the electron mobility of InSb/NiSb is, in fact, characteristic of the InSb matrix.

Fig.27 also shows that the values of $|R_H^x| \sigma(\frac{+}{-})$ converge at high temperatures. This is a consequence of σ_i approaching σ_n as the temperature increases.

In order to arrive at a qualitative understanding of the Hall coefficients observed with sample 2 in orientation B (e.g. see 7.1) in which pseudo-geometrical effects occur, the composite model described in section 2.2.2. was adopted.

Since the Hall angle is invariant to changes in sample geometry, the same Hall angle is present in the InSb layers of the composite model as in an extended sample. Therefore, the Hall angle, θ_m , may be deduced from (2.38) by assuming that the mobility ratio takes the generally accepted value of 90 at room temperature and using the experimental parameters obtained from sample 1. If θ_m and the value of R_H^B/R_H^A obtained from samples 1 and 2 are substituted into

(2.46) a unique value $G(l/\omega, \theta_m)$ is defined at a specific Hall angle. From Fig.6(b) it may be seen that this value of $G(l/\omega, \theta_m)$ corresponding to the Hall angle, θ_m , is satisfied by a single value of l/ω i.e. l'/ω' . This value of l'/ω' then constitutes the aspect ratio of the InSb layers in the composite model shown in Fig.23(b) and Fig.7.

If l'/ω' remained constant with decreasing magnetic field the Hall coefficient R_H^B would vary in such a way that R_H^B/R_H followed a single curve of Fig.6(b). The results contained in Figs.32(a) to 35(a) however, show that R_H^B and therefore R_H^B/R_H remains fairly constant for the range $2kG < B_z < 8kG.$, but is lower for $B_z < 2kG.$ Therefore, as the magnetic field is reduced less of the Hall voltage is shorted out than is predicted by Fig.6(b). This is thought to be the result of some inclusion misorientation which would tend to reduce the variation of R_H^B with magnetic field. However, since the Hall angle tends to saturate as B_z increases, a single value of l'/ω' may be approximated to the sample for the larger of the above ranges of B_z , at a fixed temperature.

By assuming that the same mobility ratio prevails for the range $300^\circ K$ to $700^\circ K$, calculating the Hall angles and evaluating R_H^B/R_H experimentally, other values of l'/ω' may also be associated with the composite model at higher temperatures. These show that as the temperature is increased, $\tan \theta_m$ and therefore θ_m decrease and l'/ω' increases as σ_i approaches σ_n . If σ_n/σ_i remained constant with increasing sample temperature the composite model would retain the same aspect ratio l'/ω' and the experimentally deduced value of $G(l'/\omega', \theta_m)$ would follow a single curve of Fig.6(b). Since, however, σ_n/σ_i reduces with increasing temperature, less shorting of the Hall voltage occurs so that l'/ω' must increase and consequently

R_H^6 and R_H must converge at high temperatures.

Sample 3, in orientation C, contains inclusions which lie parallel to the direction of current flow and, therefore, perpendicular to the Hall voltage. Sample 1, in orientation A, contains inclusions which also lie perpendicular to the Hall voltage. Therefore, at first glance it might be expected that no more transverse voltage shorting would occur in sample 3 than in sample 1, and that the same undisturbed Hall coefficient would be observed. The room temperature measurements in section 7.1., however, show that R_H^C is strikingly low compared with $R_H (= R_H^A)$. In order to explain this disparity, a closer examination of the real significance of the parameter denoted as R_H^C is required.

The model representing sample 3 in orientation C is shown in Fig.23(a). In this model the cross-sectional areas of InSb and NiSb (shown shaded) are A and a respectively. The parallel resistances of InSb and NiSb are R_1 and R_2 respectively, where

$$R_1 = \frac{L}{\sigma_1 A} \text{ and } R_2 = \frac{L}{\sigma_2 a}$$

and L is the length of sample 3.

If current i_1 flows in R_1 and current i_2 flows in R_2 , the total sample current i is given by

$$i = i_1 + i_2 \quad (7.7)$$

$$\text{and } i_1 R_1 = i_2 R_2. \quad (7.8)$$

Since from (7.5), (7.7) and (7.8),

$$i_1 = \frac{i}{(1 + M\phi_1)} \quad (7.9)$$

Recalling that the expressions deduced for the Hall coefficient in Chapter 2 were based on the assumption that the sample was perfectly homogeneous and that all the sample current, i , contributed to the Hall voltage, then clearly R_H^C does not represent

the true value of the Hall coefficient of sample 3. The transverse voltage in sample 3 is built up in the InSb component only. This component carries current i_1 , which is related to i by equation (7.9). Consequently, the experimentally observed Hall coefficient, R_H^c , is underestimated by a factor $(1 + M\phi_1)$. The correct value of the Hall coefficient, R_H^{ct} , is given by

$$\begin{aligned} R_H^{ct} &= R_H^c (1 + M\phi_1) \\ &= R_H^c \frac{\sigma_{||}}{\sigma_{\perp}} \quad \text{from (7.5)}. \end{aligned} \quad (7.10)$$

Therefore, provided that the electrical conductivities $\sigma_{||}$ and σ_{\perp} are known, the correct value of the Hall coefficient may be calculated for all temperatures from (7.10).

Proceeding to correct the room temperature value of $R_H^c = 223 \text{ coul.}^{-1} \text{ cm.}^3$, a value of $R_H^{ct} = 270 \text{ coulomb}^{-1} \text{ cm.}^3$ is obtained. Comparison of the latter value with $R_H^A = R_H^A = 327 \text{ coul.}^{-1} \text{ cm.}^3$, obtained with sample 1, shows that a substantial part of the Hall voltage is shorted out in sample 3. This infers that some of the inclusions in sample 3 possess a small degree of misorientation.

As with sample 2, a "geometry" may be assigned to sample 3 from the value of the ratio R_H^{ct}/R_H and Fig.6(b), provided the Hall angle is known. The value of this parameter may be determined in the following manner.

The current i_1 arises from the application of a longitudinal electric field E_x , where

$$E_x = \frac{i}{(A + a)\sigma_{||}} \quad (7.11)$$

The effect of applying the same electric field E , to a pure sample of InSb, having the same values of L and $(A + a)$ as sample 3, will now be considered. If the pure sample of resistance R_p and conductivity σ_{\perp} carries a current i_p , then

$$R_p = \frac{L}{(A + a)} \quad (7.12)$$

$$\text{and } i_p = j_x (A + a) \quad (7.13)$$

$$\text{where } j_x = \sigma_i E_x \quad (7.14)$$

From (7.13) and (7.14),

$$E_x = \frac{i_p}{(A + a)\sigma_i} \quad (7.15)$$

Equation (7.15) and (7.11) yield

$$i = \frac{\sigma_{ii}}{\sigma_i} i = (1 + M\phi_i) i_p \quad (7.16)$$

For the pure specimen the transverse electric field is given by

$$\begin{aligned} E_y &= R_H j_x B_z \\ \therefore E_y &= \frac{R_H i_p B_z}{(A + a)} \end{aligned} \quad (7.17)$$

The transverse electric field E_y' arising from the current density j_x' in the InSb component of sample 3, is given by

$$\begin{aligned} E_y' &= R_H j_x' B_z \\ &= \frac{R_H i}{A} B_z. \end{aligned} \quad (7.18)$$

Substituting from (7.9),

$$E_y' = \frac{R_H i B_z}{A(1 + M\phi_i)} \quad (7.19)$$

From (7.16),

$$E_y' = \frac{R_H i_p B_z}{A} \quad (7.20)$$

Comparison of (7.20) and (7.17) shows that

$$E_y' = E_y \text{ when } a \ll A, \text{ as in sample 3.}$$

Therefore, the Hall angle, $\theta_m = \tan(E_y/E_x)$, present in an extended sample of pure InSb, is conserved in the InSb component of InSb/NiSb sample 3 in orientation C. This means that the Hall angle obtained from sample 1 may also be used with R_H^{ct}/R_H and Fig.6(b) to determine the "geometry", l'/ω' associated with the shorting

produced in sample 3.

Figs. 36(a) to 39(a) show the experimentally observed Hall coefficients, R_H^c , obtained at various temperatures with sample 3. In common with sample 2 the values below 2kG are relatively low compared with those in the range $2kG < B_2 < 8kG$. Further, as in the case of sample 2, the value of l'/ω' also increases with temperature, so that R_H^{ct} and therefore R_H^c converges with R_H^g and $R_H^A (=R_H^A)$ at high temperatures.

7.1.3. Transverse "Magnetoresistance"

The term "Magnetoresistance" in the above section heading is applied loosely to describe the relative increases in the resistivity of InSb/NiSb specimens that are subjected to a transverse magnetic field.

The room temperature values of the relative resistances r_A , r_g and r_c , brought about by a 7.3 kG. magnetic field, shown in section 7.1., differ greatly with orientation as different "geometries" are created by the inclusions. The way in which each value arises will now be discussed.

As previously explained, the behaviour of the Hall coefficient and electrical conductivity of InSb/NiSb sample 1 in orientation A approximates closely to the behaviour of the InSb matrix. Samples of pure InSb of aspect ratio $l/\omega \gg 5$, however, show no appreciable geometrical effects, so that the relative resistance of pure InSb, from (2.46) is given by

$$r = r_m \text{ as } r_g = 1$$

For InSb/NiSb sample 1 the sample dimensions ensure that the criterion $l/\omega \gg 5$ is also obeyed, so that it would be expected that mixed conduction alone would be responsible for the increase in resistance, and that from (2.41),

$$r = r = 1 + \frac{\mu_c B^2}{bc} \quad (7.21)$$

Inserting the room temperature parameters into (7.21) gives $r_m = 1.30$, compared with the experimental value of $r_A = 1.44$ obtained in a magnetic field of 7.3 kG.

The discrepancy between these two values can arise either from current distortions present at the inclusion boundaries as described in 2.2.3., or through a very small reduction in Hall voltage due to slight inclusion misorientation. Whatever the source

of the discrepancy is, an essentially "geometrical" increase in resistance is present in sample 1 in orientation A. The discrepancy may be resolved by providing a suitable "geometrical" contribution, r_g , from which the corresponding "geometry" l''/ω'' may be calculated.

When, over the experimental range of magnetic fields, the necessary values of r_g are plotted against the corresponding values of $\tan \theta_m$ a linear dependence emerged of r_g increasing with $\tan \theta_m$. Extrapolating r_g to a large Hall angle ($\theta_m = \tan^{-1} 7$) as in Fig. 28(b) then allowed l''/ω'' to be determined from (2.41) i.e.

$$r = 1 + \frac{\omega''}{l''} \left[\frac{8 \cdot \tan \theta_m}{3\pi} - 4 \ln 2 \right]$$

The relative resistance of InSb/NiSb sample 1 in orientation A was then given theoretically by

$$r_A = r_m r_g$$

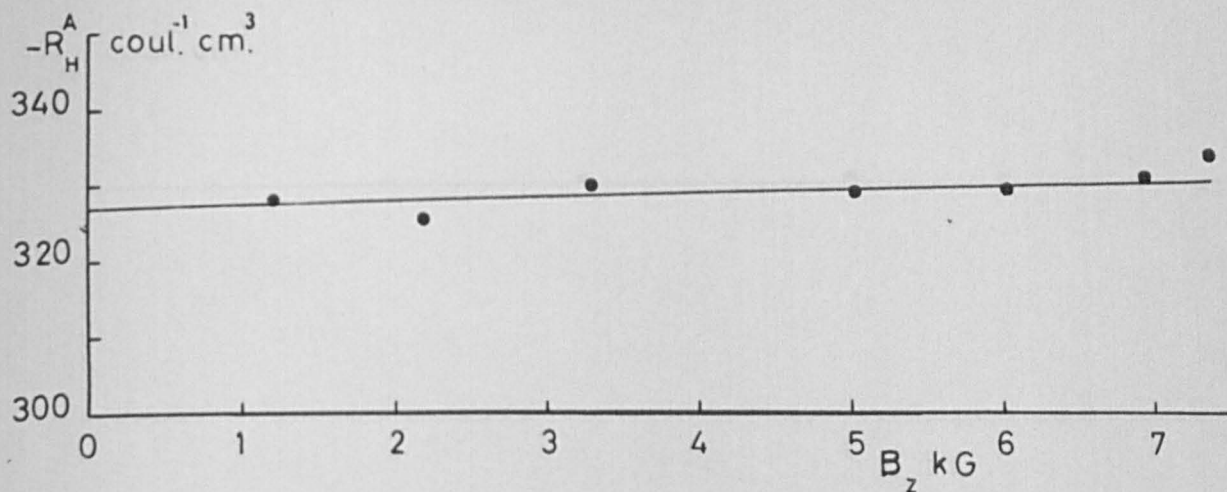
The theoretical and experimental values of r_A v B_z have been plotted for room temperature in Fig. 28(c). The values of r_g necessary give agreement with the experimentally observed values of r_A suggested that the theoretical sample geometry l''/ω'' was in this case approximately 24. Since, however, $l''/\omega'' > 5$ then from Fig. 6(a), the Hall coefficients measured with sample 1 in orientation A are not lowered by the presence of inclusions.

By following the process described above, other values of r_g and l''/ω'' were assigned sample 1 at higher temperatures, as shown in Figs. 29(b) to 31(b). The experimental values and the theoretical curves for r_A are then given in Figs. 29(c) to 31(c). The results show that with increasing temperature the geometrical contribution, r_g , falls and that the value of the parameter l''/ω'' shows a consequent increase. The comparatively low value of l''/ω'' obtained

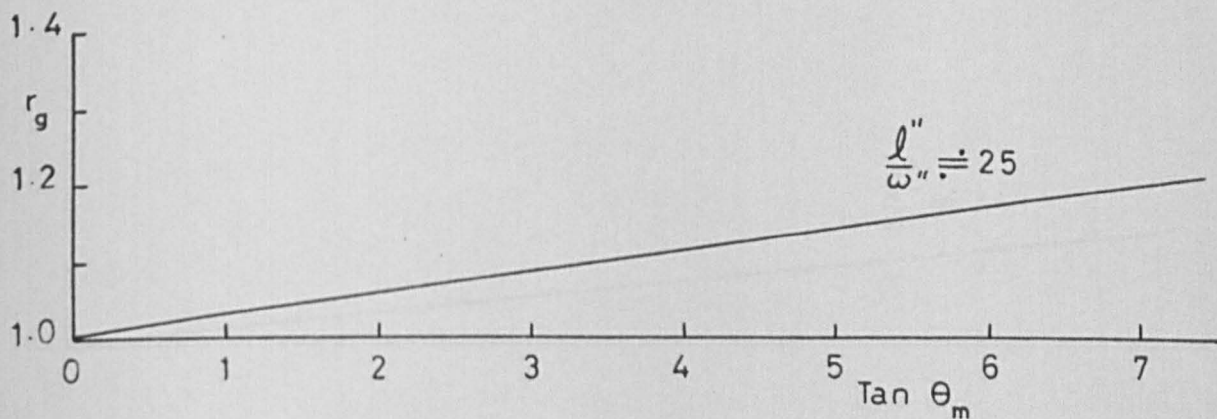
Fig.28

PROPERTIES OF InSb/NiSb SAMPLE 1 IN ORIENTATION A, AT 294°k

(a) Hall Coefficient (R_H^A) V Magnetic Field (B_z)



(b) Geometrical Resistance (r_g) V Tan Hall Angle ($\text{Tan } \theta_m$)



(c) Relative Resistance (r_A) V Magnetic Field (B_z)

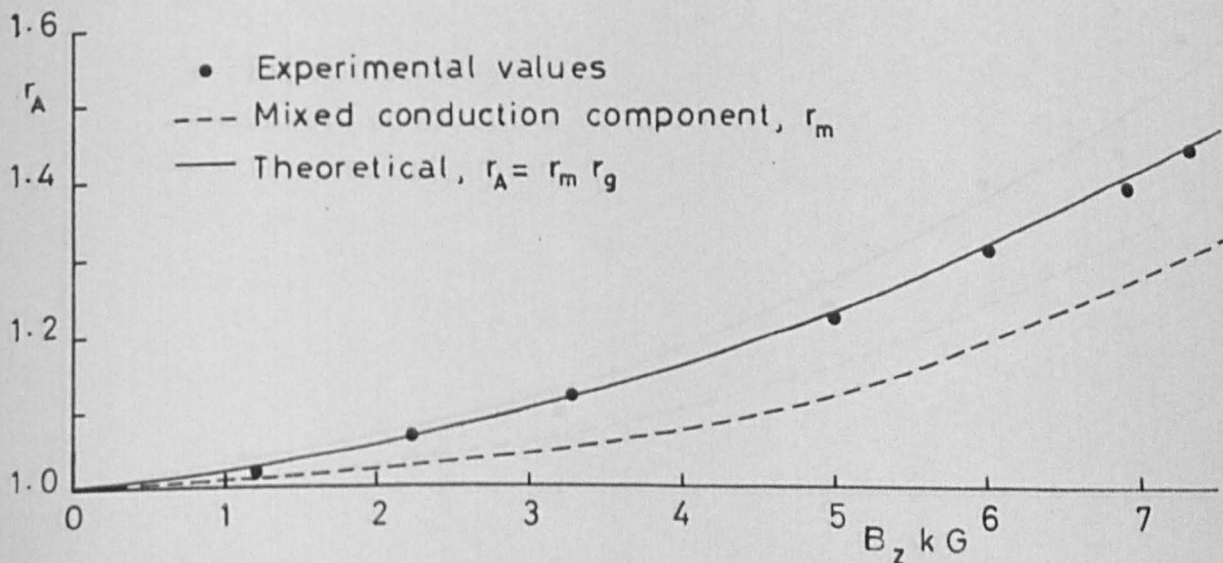
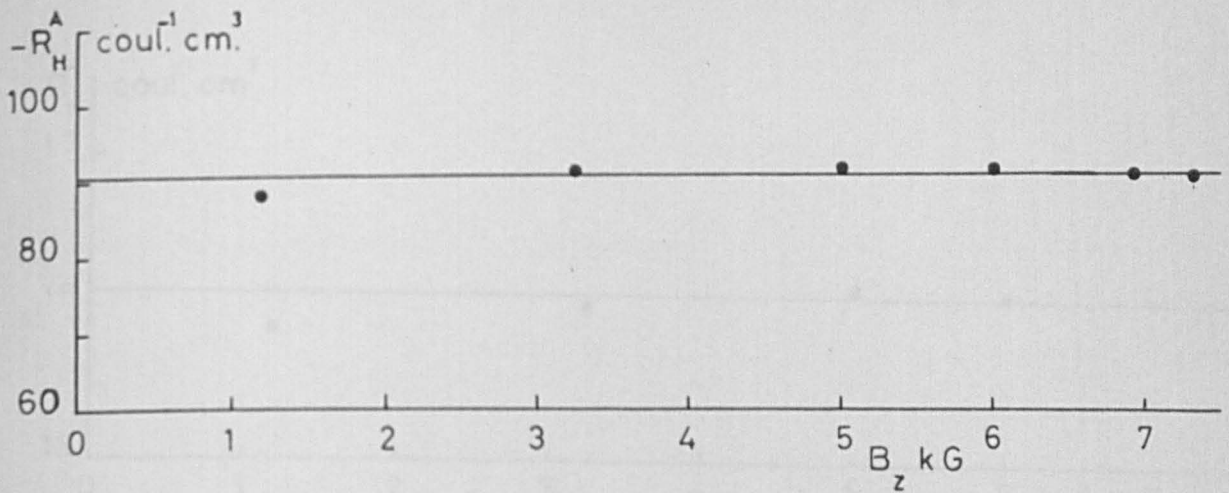


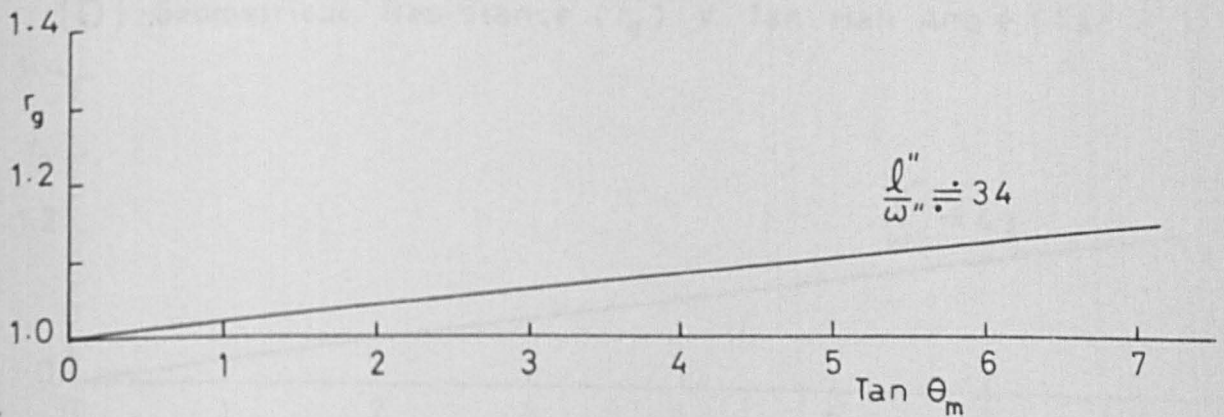
Fig.29

PROPERTIES OF InSb/NiSb SAMPLE 1 IN ORIENTATION A, AT 367° k

(a) Hall Coefficient (R_H^A) V Magnetic Field (B_z)



(b) Geometrical Resistance (r_g) V Tan Hall Angle ($\tan \theta_m$)



(c) Relative Resistance (r_A) V Magnetic Field (B_z)

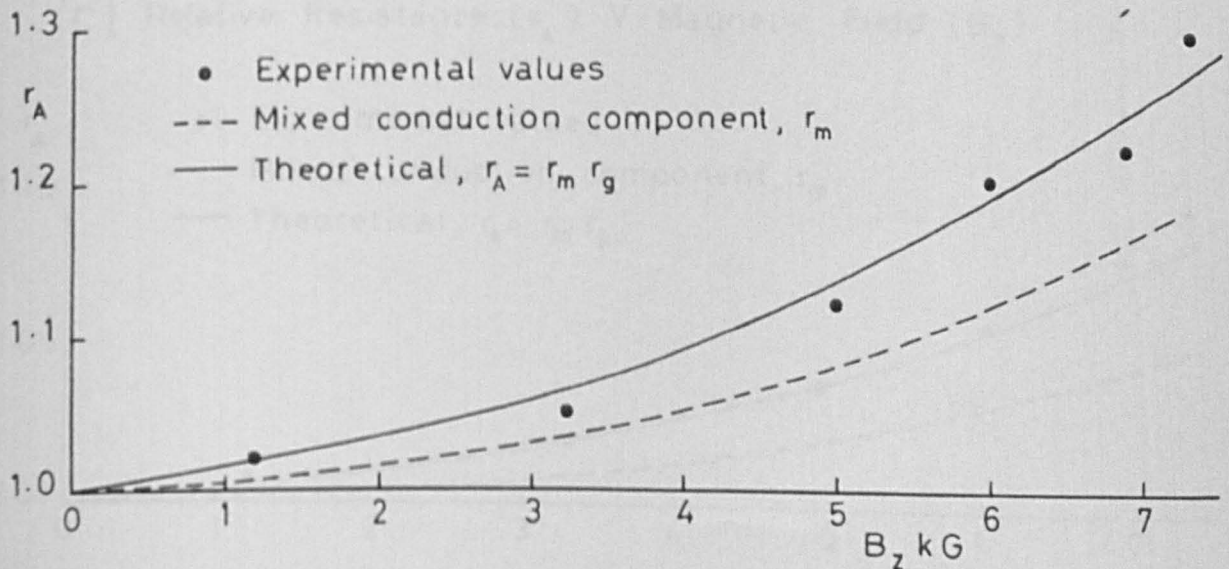
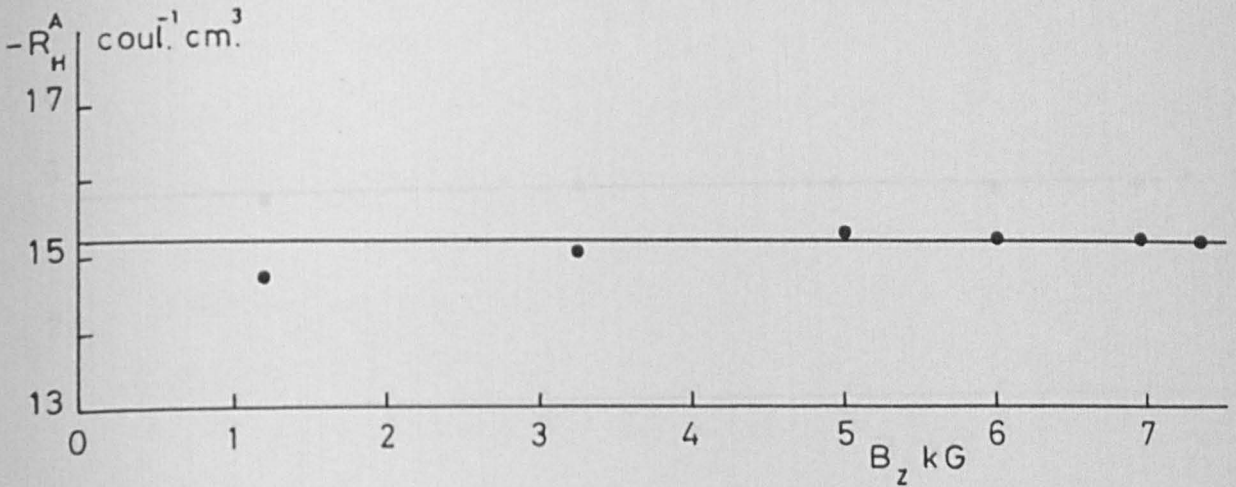


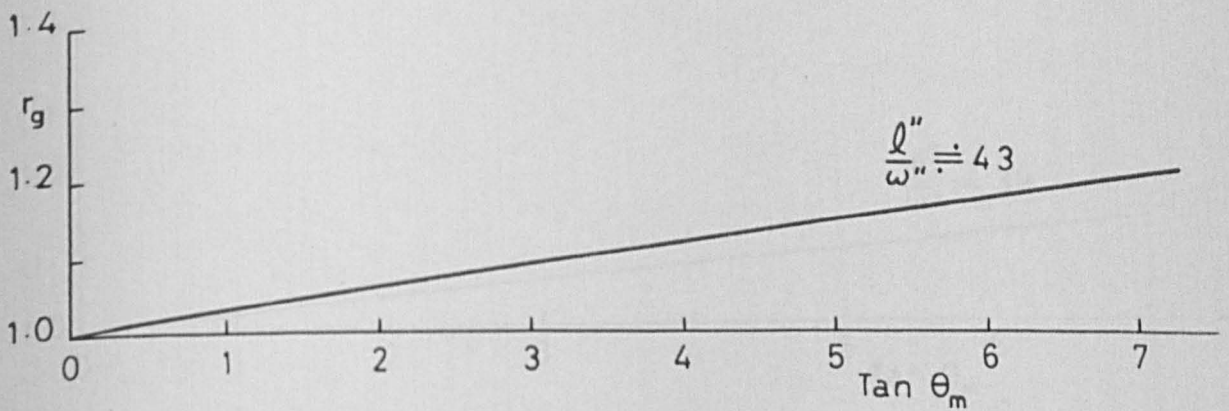
Fig. 30

PROPERTIES OF InSb/NiSb SAMPLE 1 IN ORIENTATION A, AT 528° K

(a) Hall Coefficient (R_H^A) V Magnetic Field (B_z)



(b) Geometrical Resistance (r_g) V Tan Hall Angle ($\tan \theta_m$)



(c) Relative Resistance (r_A) V Magnetic Field (B_z)

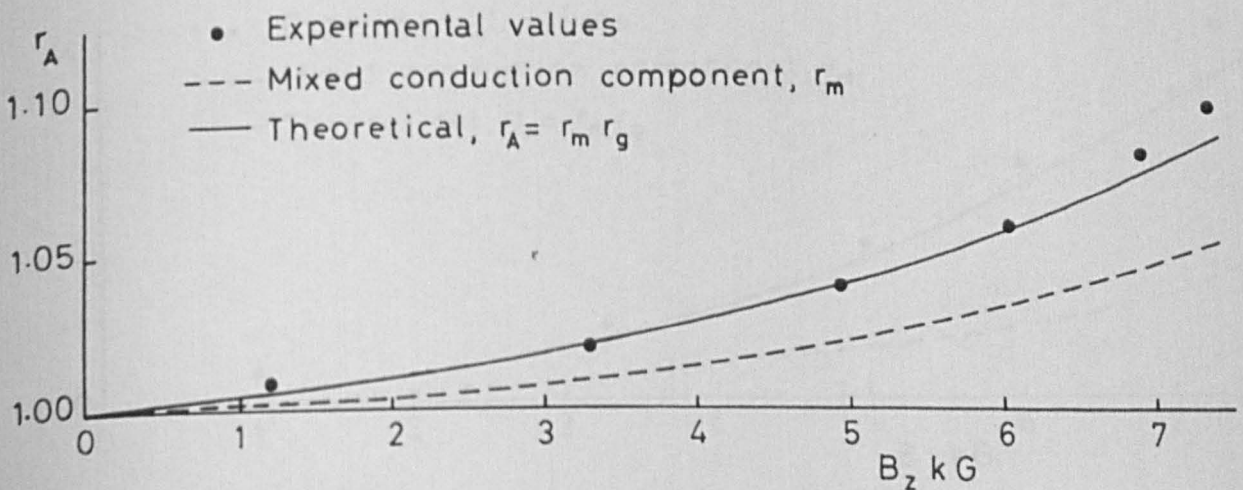
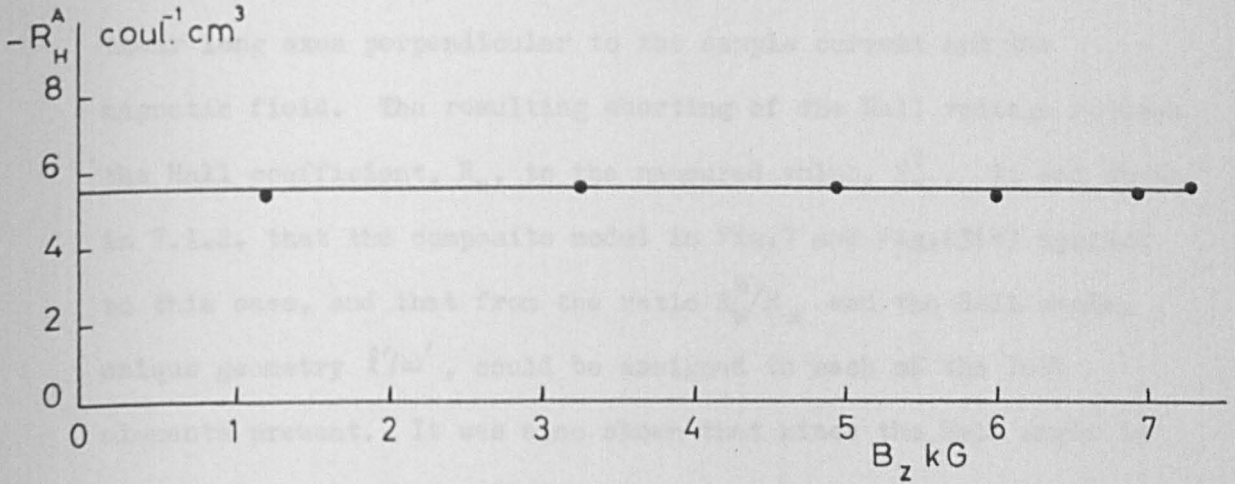


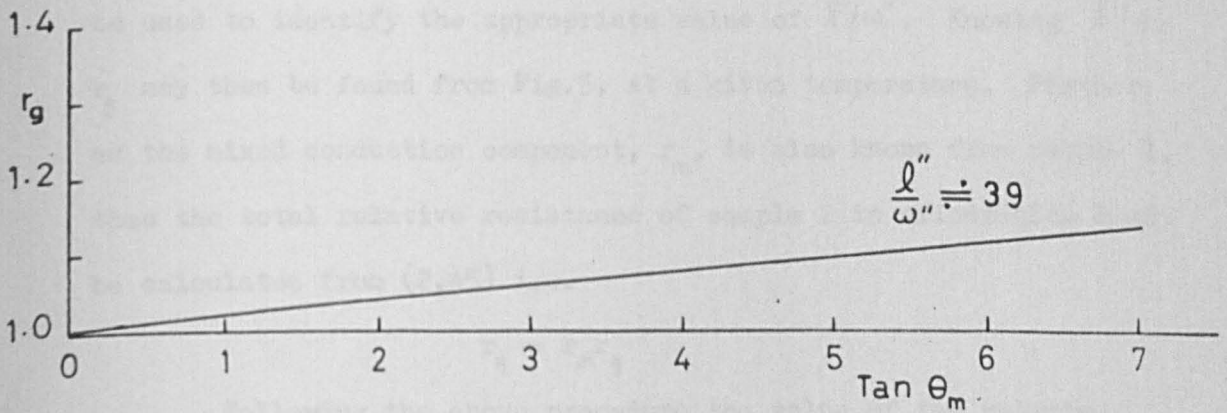
Fig. 31

PROPERTIES OF InSb/NiSb SAMPLE 1, ORIENTATION A, AT 698° K.

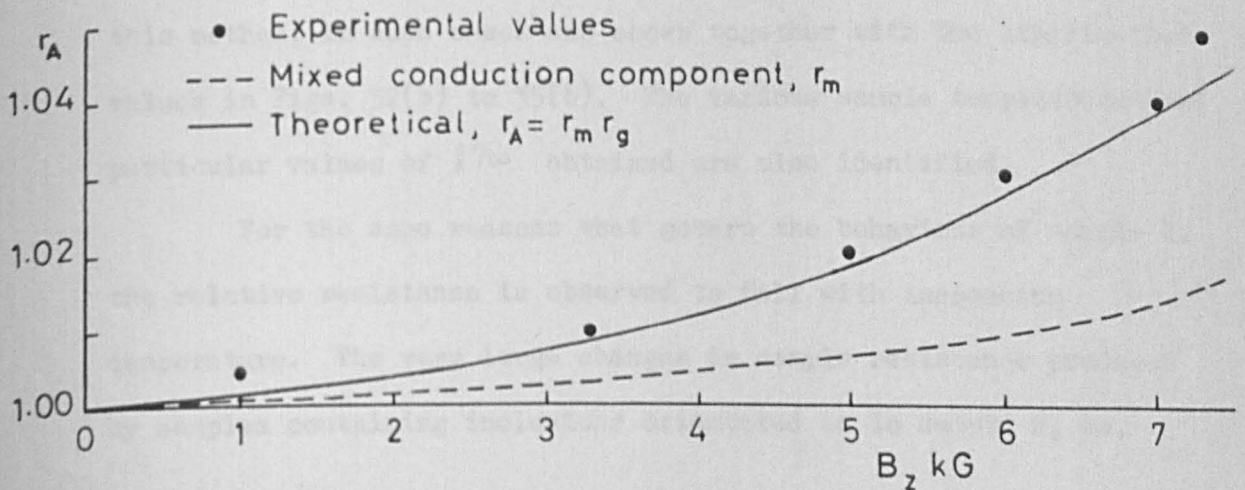
(a) Hall Coefficient (R_H^A) V Magnetic Field (B_z)



(b) Geometrical Resistance (r_g) V Tan Hall Angle ($\text{Tan } \theta_m$)



(c) Relative Resistance (r_A) V Magnetic Field (B_z)



at the highest temperature (698°K) however, appears to break this trend. This behaviour is consistent with an underestimation of r_m and $\tan \theta_m$, probably arising from a reduced mobility ratio at 700°K .

In orientation B, the inclusion rods of sample 2 lie with their long axes perpendicular to the sample current and the magnetic field. The resulting shorting of the Hall voltage reduces the Hall coefficient, R_H , to the measured value, R_H^B . It was shown in 7.1.2. that the composite model in Fig.7 and Fig.23(b) applies to this case, and that from the ratio R_H^B/R_H and the Hall angle, unique geometry l'/w' , could be assigned to each of the InSb elements present. It was also shown that since the Hall angle is conserved in all three samples, for given temperature and magnetic field, the value of θ_m obtained from sample 1 in orientation A could be used to identify the appropriate value of l'/w' . Knowing l'/w' , r_g may then be found from Fig.5, at a given temperature. Further, as the mixed conduction component, r_m , is also known from sample 1, then the total relative resistance of sample 2 in orientation B may be calculated from (2.45) i.e.

$$r_g = r_m r_g$$

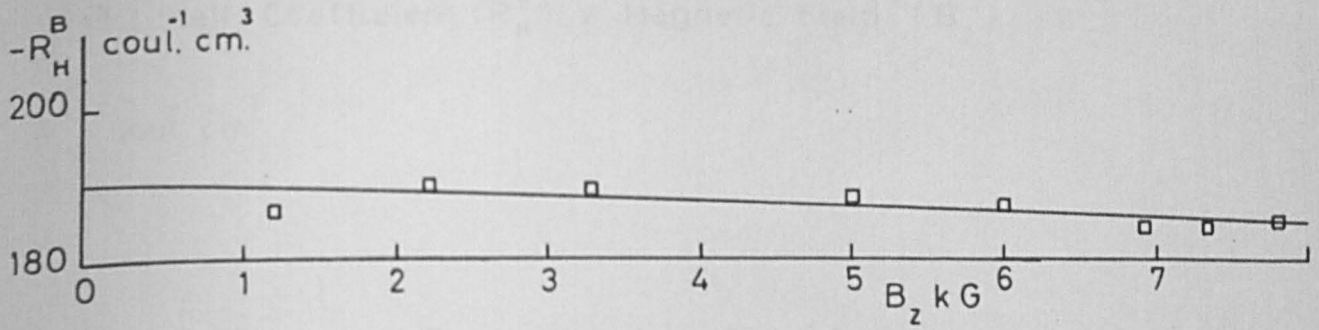
Following the above procedure the value of the relative resistance, r_g , may be deduced over a range of magnetic fields and sample temperatures. The theoretical curves of r_g obtained using this method, in such cases are shown together with the experimental values in Figs. 32(b) to 35(b). The various sample temperatures and particular values of l'/w' obtained are also identified.

For the same reasons that govern the behaviour of sample 1, the relative resistance is observed to fall with increasing temperature. The very large changes in sample resistance produced by samples containing inclusions orientated as in sample 2, do,

Fig.32

PROPERTIES OF InSb/NiSb SAMPLE 2 IN ORIENTATION B, AT 294°K.

(a) Hall Coefficient (R_H^B) V Magnetic Field (B_z)



(b) Relative Resistance (r_B) V Magnetic Field (B_z)

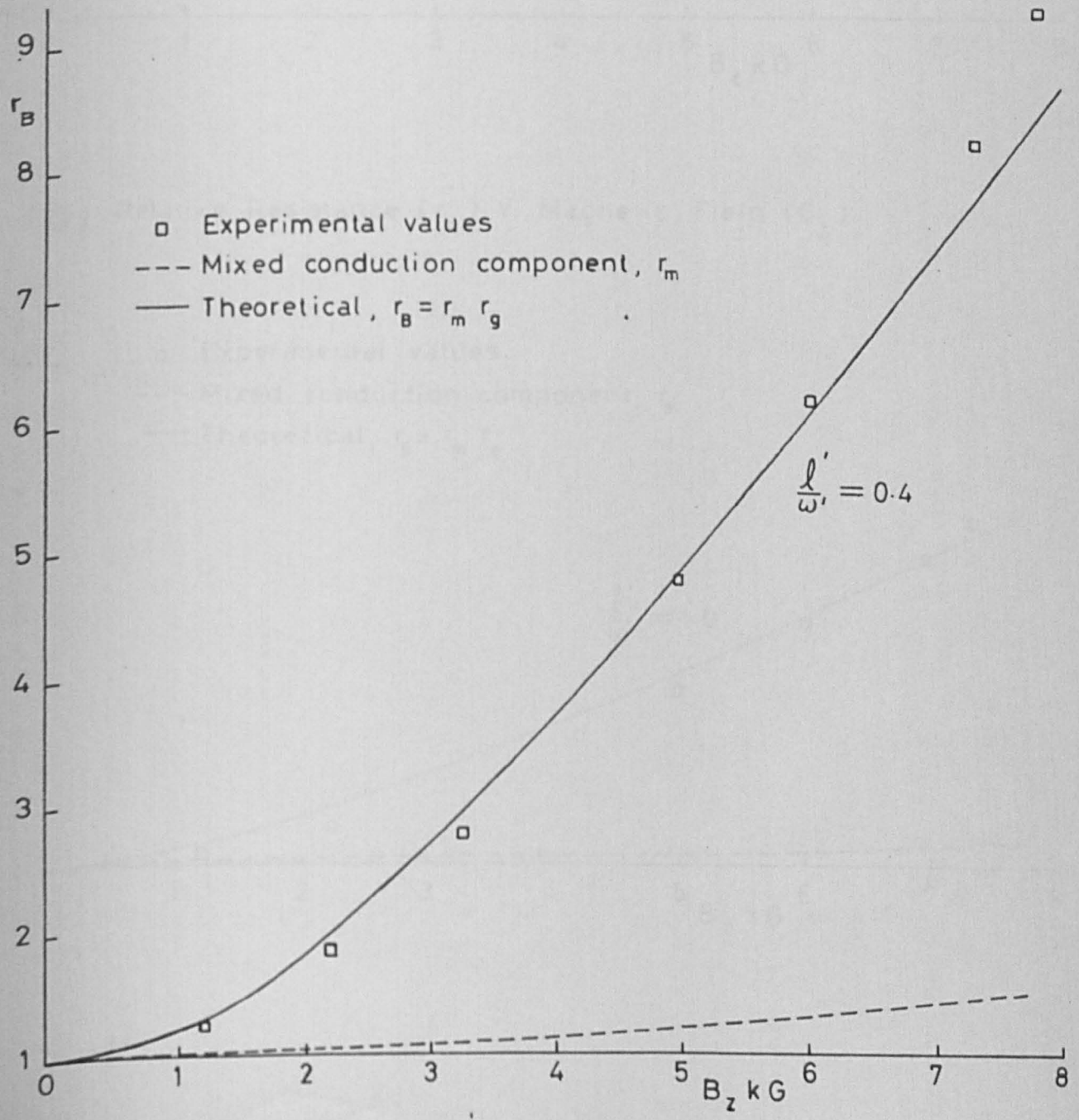
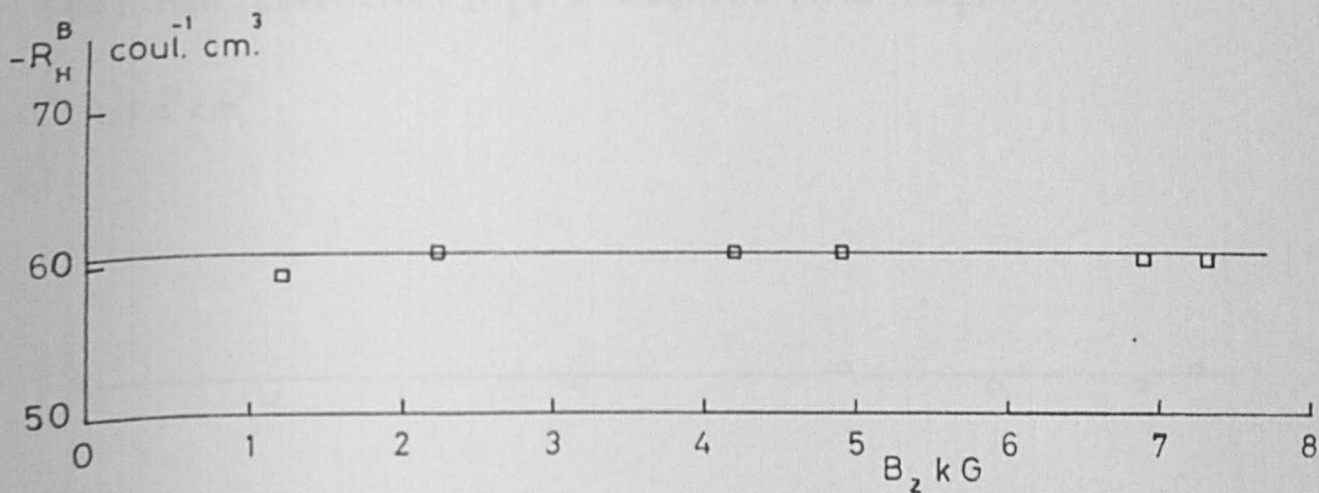


Fig. 33

PROPERTIES OF InSb/NiSb SAMPLE 2 IN ORIENTATION B, AT 377° k.

(a) Hall Coefficient (R_H^B) V Magnetic Field (B_z)



(b) Relative Resistance (r_B) V Magnetic Field (B_z)

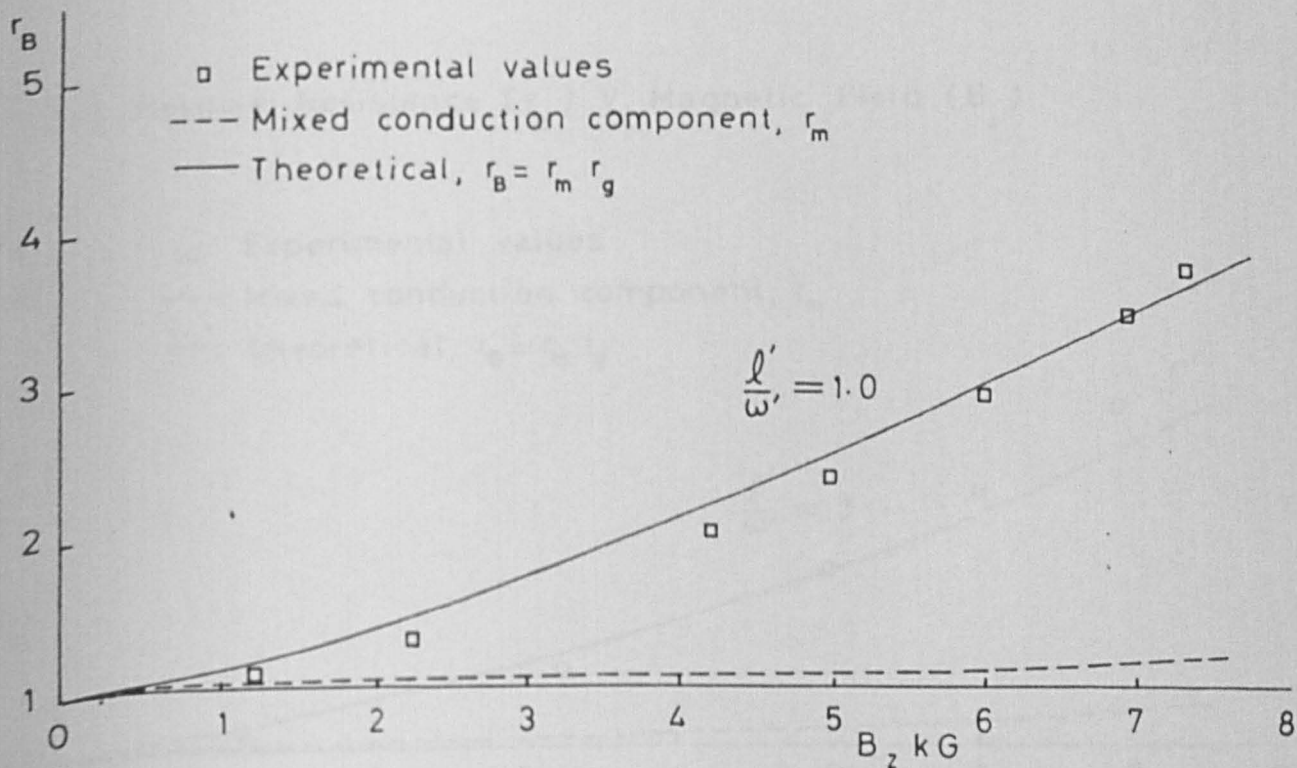
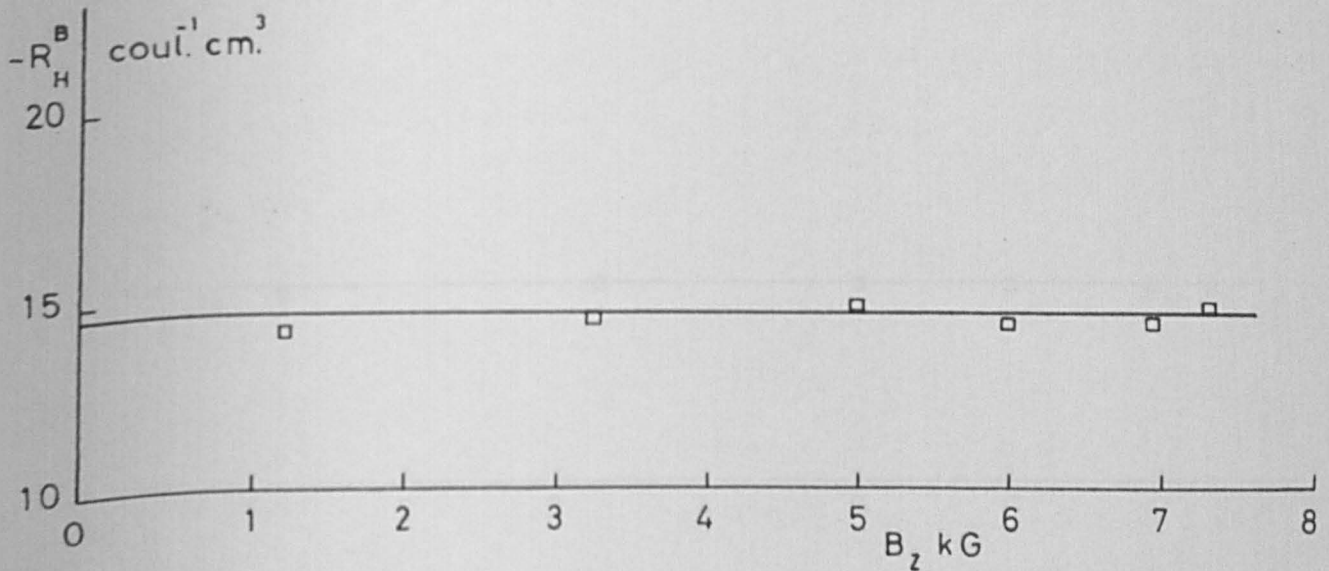


Fig. 34

PROPERTIES OF InSb/NiSb SAMPLE 2 IN ORIENTATION B, AT 529° K.

(a) Hall Coefficient (R_H^B) V Magnetic Field (B_z)



(b) Relative Resistance (r_B) V Magnetic Field (B_z)

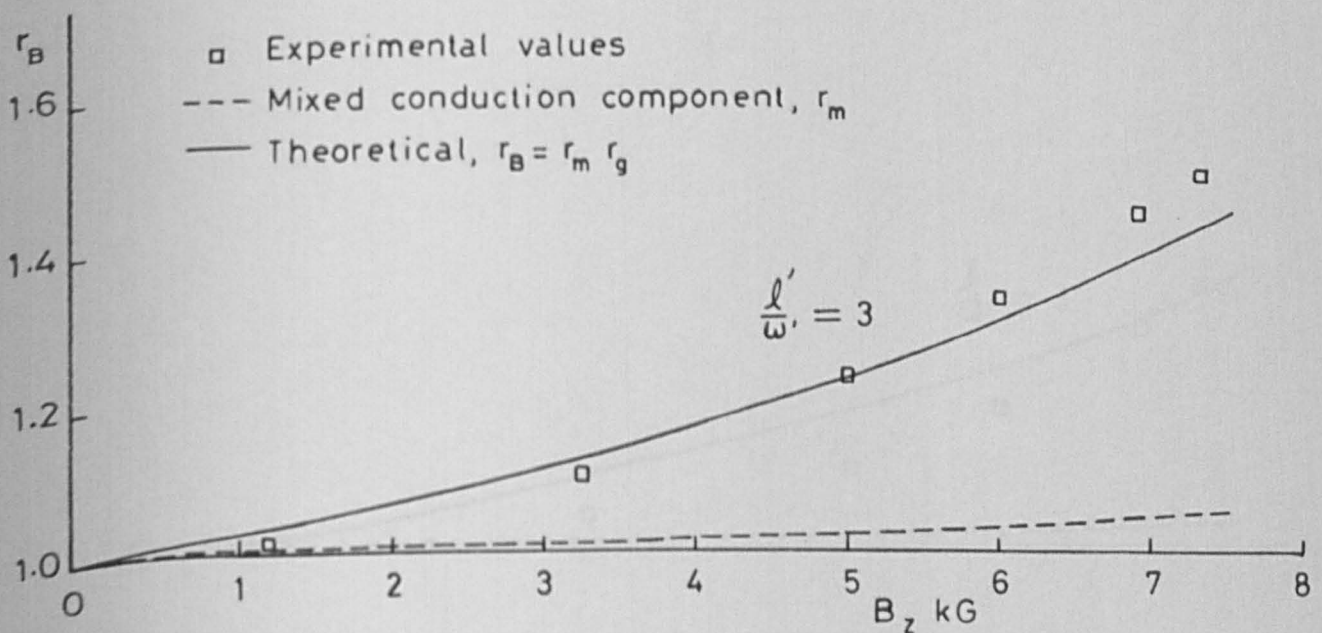
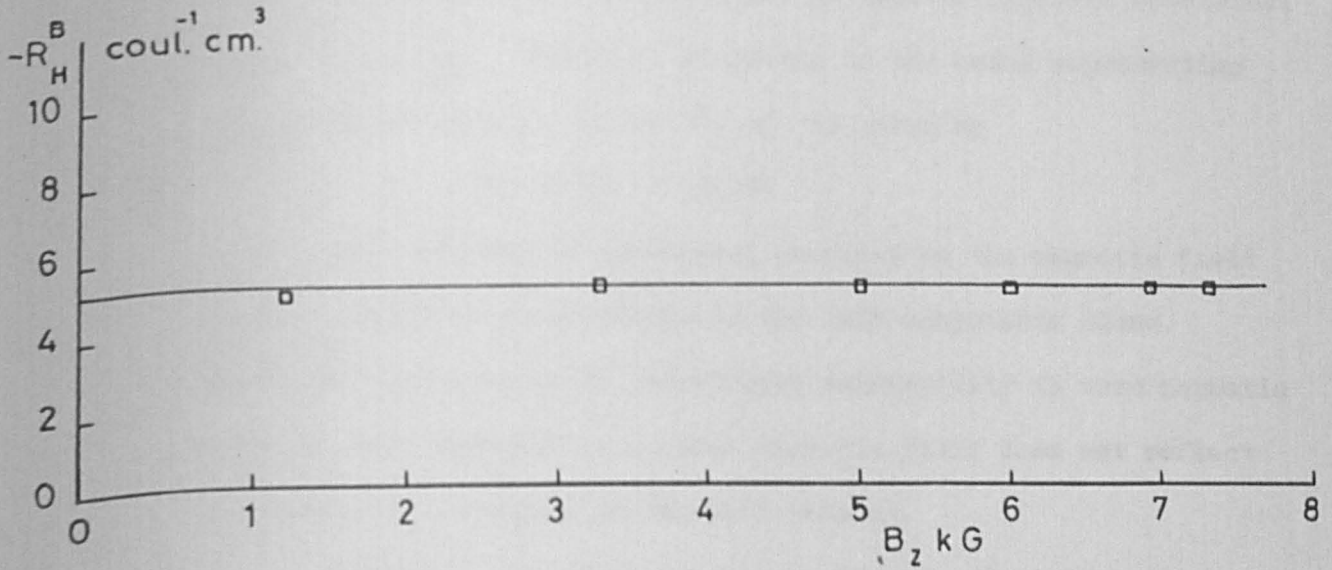


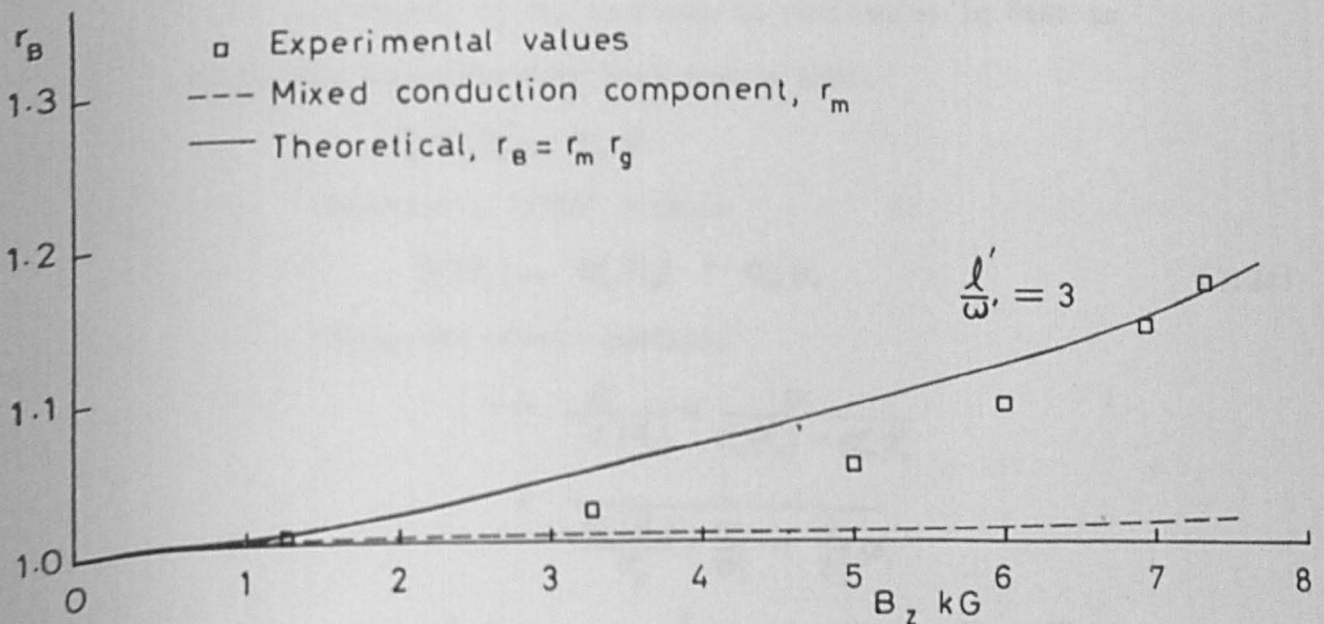
Fig. 35

PROPERTIES OF InSb/NiSb SAMPLE 2 IN ORIENTATION B, AT 696° K.

(a) Hall Coefficient (R_H^B) V Magnetic Field (B_z)



(b) Relative Resistance (r_B) V Magnetic Field (B_z)



however, suggest that InSb/NiSb has possible practical application as a switching device or for constructing variable resistances without moving parts.

Sample 3 in orientation C contains inclusions which lie along the direction of current flow, so that an improved electrical conductivity, $\sigma_{||}$, results. According to the model representing this sample, shown in Fig 23(a), $\sigma_{||}$ is given by

$$\sigma_{||} = \sigma_i + \sigma_N \phi_i$$

The increase in resistance produced by the magnetic field in this sample is attributable to the InSb components alone. Therefore the ratio of the electrical conductivity in zero magnetic field to that produced by a given magnetic field does not reflect the relative resistance of the InSb present.

Rewriting the above expression for the electrical conductivities in the absence of an applied magnetic field,

$$\sigma_i = \sigma_{||} - \sigma_N \phi_i \quad (7.22)$$

In the presence of a magnetic field B_z , this becomes

$$\sigma_i(B_z) = \sigma_{||}(B_z) - \sigma_N(B_z) \phi_i \quad (7.23)$$

Further, as the increase in resistance in NiSb is negligible compared with that due to InSb,

$$\sigma_N(B_z) \phi_i = \sigma_N \phi_i$$

Therefore, (7.23) becomes

$$\sigma_i(B_z) = \sigma_{||}(B_z) - \sigma_N \phi_i \quad (7.24)$$

Using the above equation,

$$\begin{aligned} r &= \frac{\sigma_i}{\sigma_i(B_z)} = \frac{\sigma_i}{\sigma_{||}(B_z) - \sigma_N \phi_i} \\ &= \frac{1}{\frac{\sigma_{||}(B_z)}{\sigma_{||}} \cdot \frac{\sigma_{||}}{\sigma_i} - \frac{\sigma_N \phi_i}{\sigma_i}} \end{aligned}$$

$$\therefore r = \frac{1}{\frac{1}{r_c} \frac{\sigma_{||}}{\sigma_i} - M \phi_i} \quad \text{where} \quad r_c = \frac{\sigma_{||}}{\sigma_{||}(B_z)}$$

Further, as $\frac{\sigma_{ii} - 1}{\sigma_i} = M \phi_i$

$$r = \frac{1}{\frac{1}{r} \cdot \frac{\sigma_{ii} - (\sigma_{ii} - 1)}{\sigma_i}}$$

$$\therefore r_c = \frac{1}{1 - \frac{\sigma_i}{\sigma_{ii}} \left(1 - \frac{1}{r}\right)}$$

From equation (7.4), $\sigma_i = \sigma_1$ then

$$r_c = \frac{1}{1 - \frac{\sigma_1}{\sigma_{ii}} \left(1 - \frac{1}{r}\right)} \quad (7.25)$$

This expression gives the value of the experimental parameter r_c . If a perfectly orientated inclusion system were present in sample 3, the corrected Hall coefficient, R_H^{ct} , would be equal to R_H . However, $R_H > R_H^{ct}$, as shown in 7.1.2. so that the orientation of the inclusion system was not perfect and "geometrical" influence is present in sample 3 and $r = r_m r_g$ in (7.25).

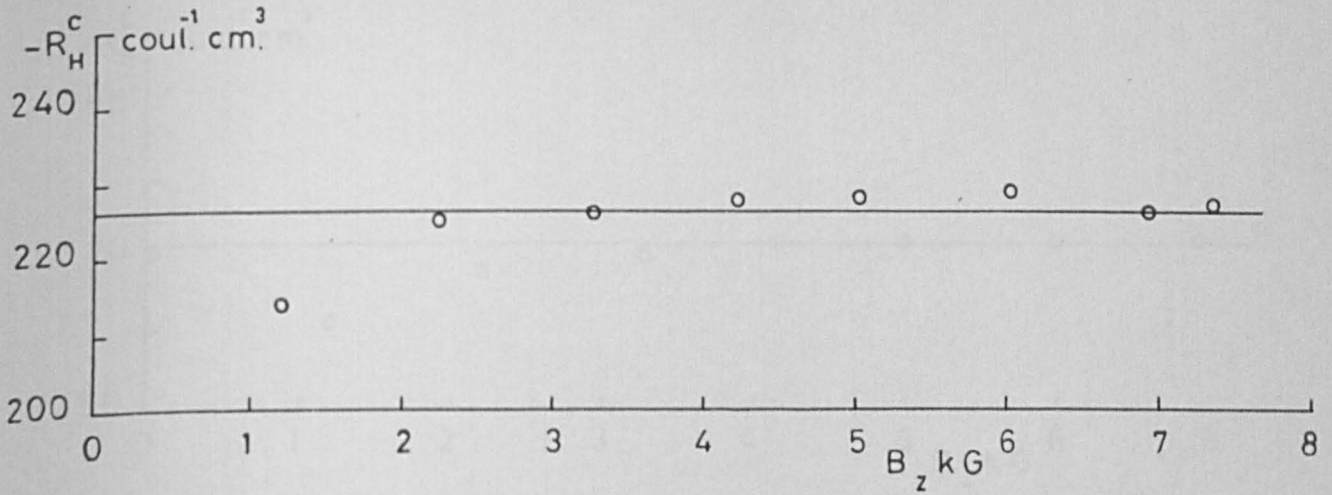
Proceeding as before, the appropriate value of r_c can be found from the ratio R_H^{ct}/R_H and the Hall angle, which has already been shown to have the same value as in sample 1. Knowing the "geometry" and the Hall angle, r_g may be found from Fig.5 and r may be calculated from (7.25). The values of r_c and l'/ω' deduced in this way for various magnetic fields and temperatures are shown in Figs. 36(c) to 39(c), while a plot of r_g v $\tan \theta_m$ is given in Figs. 36(b) to 39(b).

The figures show a deterioration in the agreement obtained between the experimental and theoretical values of r_c as the temperature rises. This is a result of the excessive demands made on the accuracy of the experimental parameters associated with the application of (7.25), at high temperatures. In common with samples 1 and 2, however, the "geometrical" effects in sample B are reduced

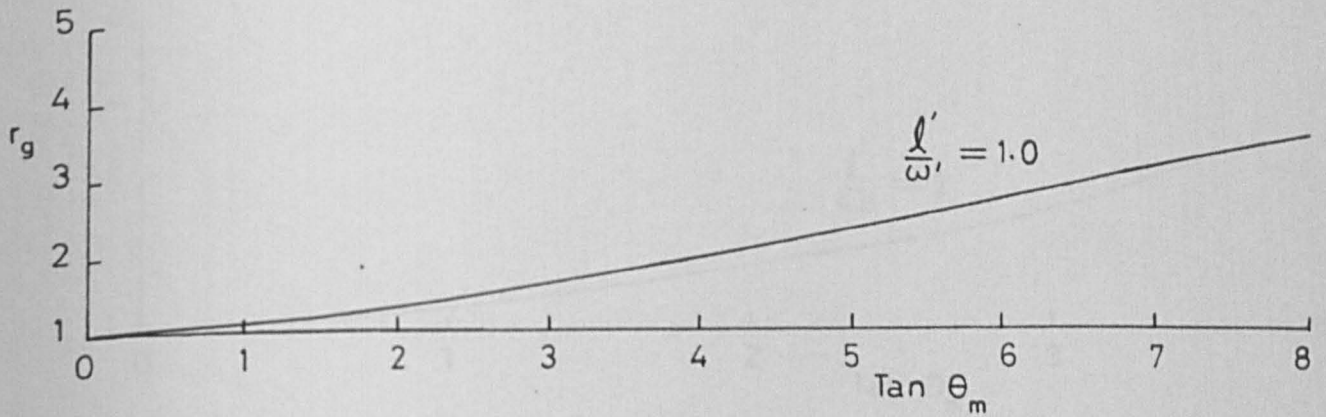
Fig.36

PROPERTIES OF InSb/NiSb SAMPLE 3 IN ORIENTATION C, AT 292°K.

(a) Hall Coefficient (R_H^C) V Magnetic Field (B_z)



(b) Geometrical Resistance (r_g) V Tan Hall Angle ($\text{Tan } \theta_m$)



(c) Relative Resistance (r_c) V Magnetic Field (B_z)

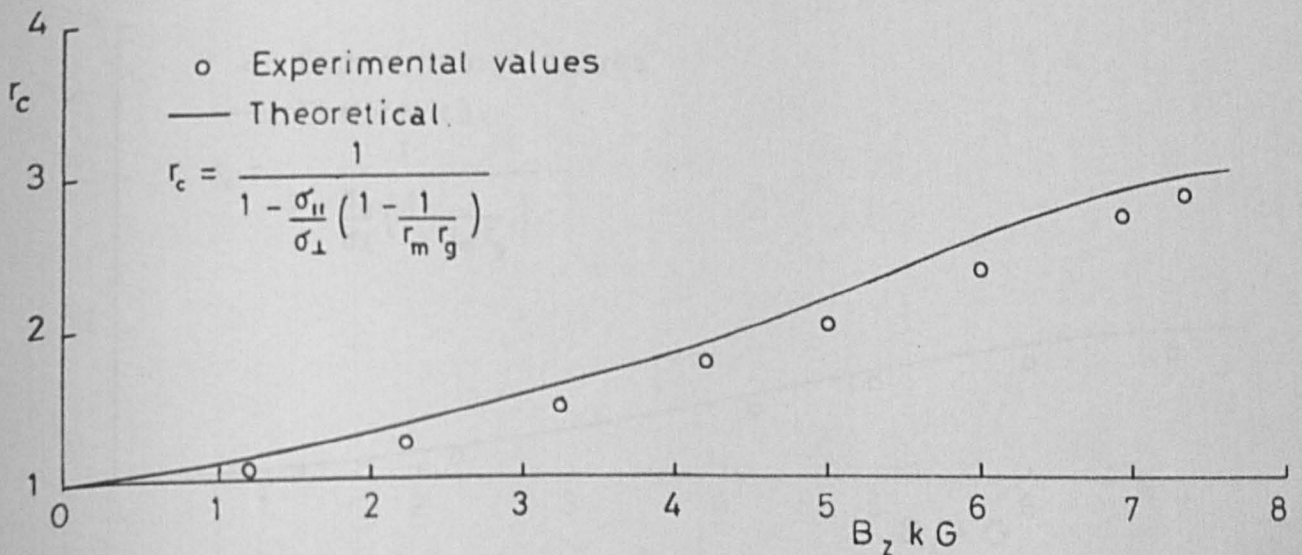
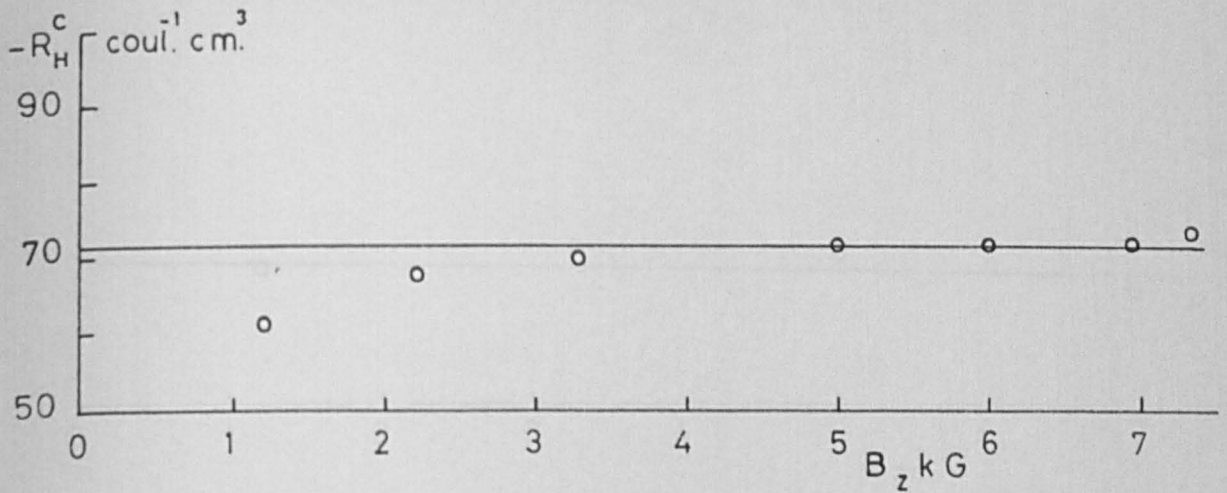


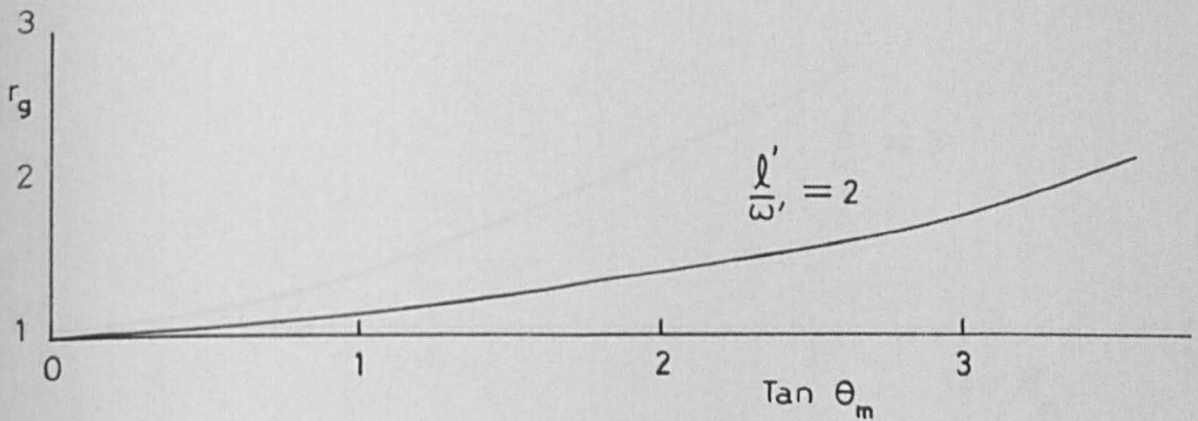
Fig.37

PROPERTIES OF InSb/NiSb SAMPLE 3 IN ORIENTATION C, AT 370° K

(a) Hall Coefficient (R_H^c) V Magnetic Field (B_z)



(b) Geometrical Resistance (r_g) V Tan Hall Angle ($\tan \theta_m$)



(c) Relative Resistance (r_c) V Magnetic Field (B_z)

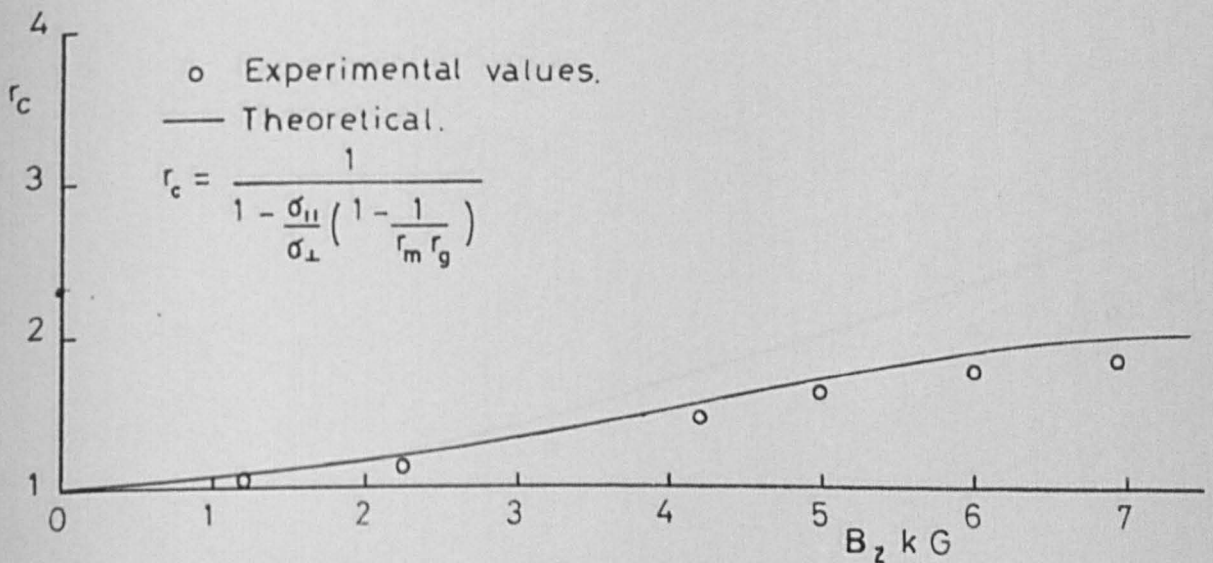
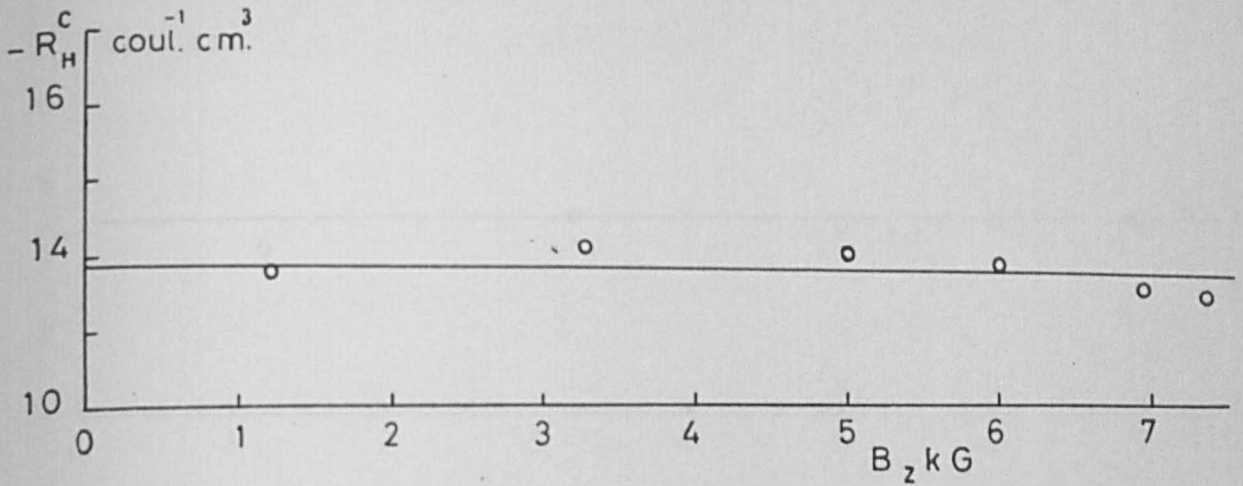


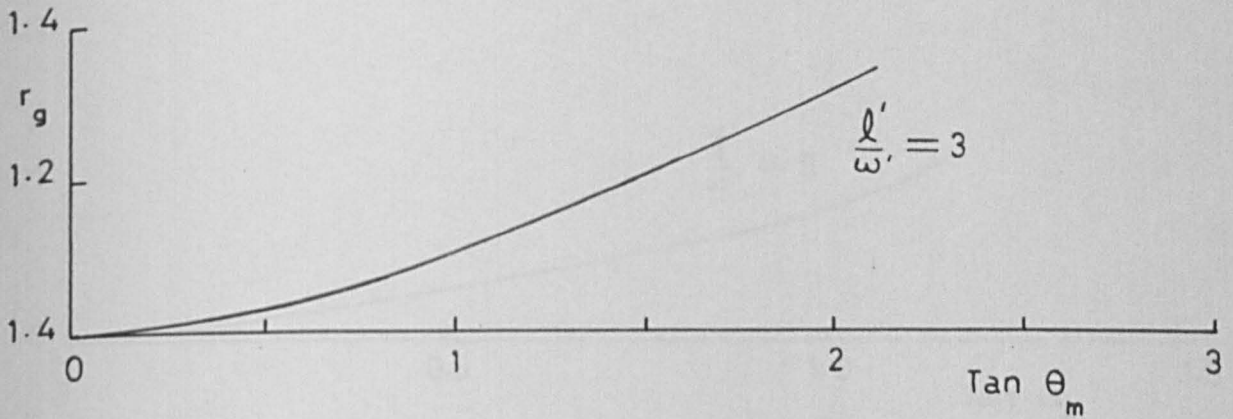
Fig.38

PROPERTIES OF InSb/NiSb SAMPLE 3 IN ORIENTATION C, AT 529°k.

(a) Hall Coefficient (R_H^C) V Magnetic Field (B_z)



(b) Geometrical Resistance (r_g) V Tan Hall Angle ($\tan \theta_m$)



(c) Relative Resistance (r_c) V Magnetic Field (B_z)

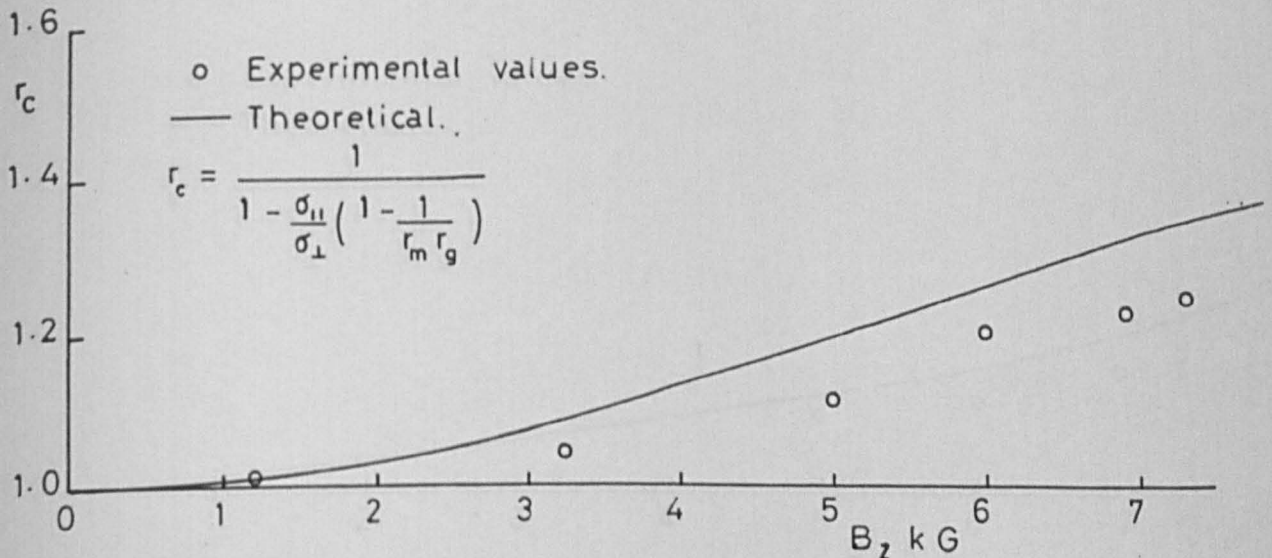
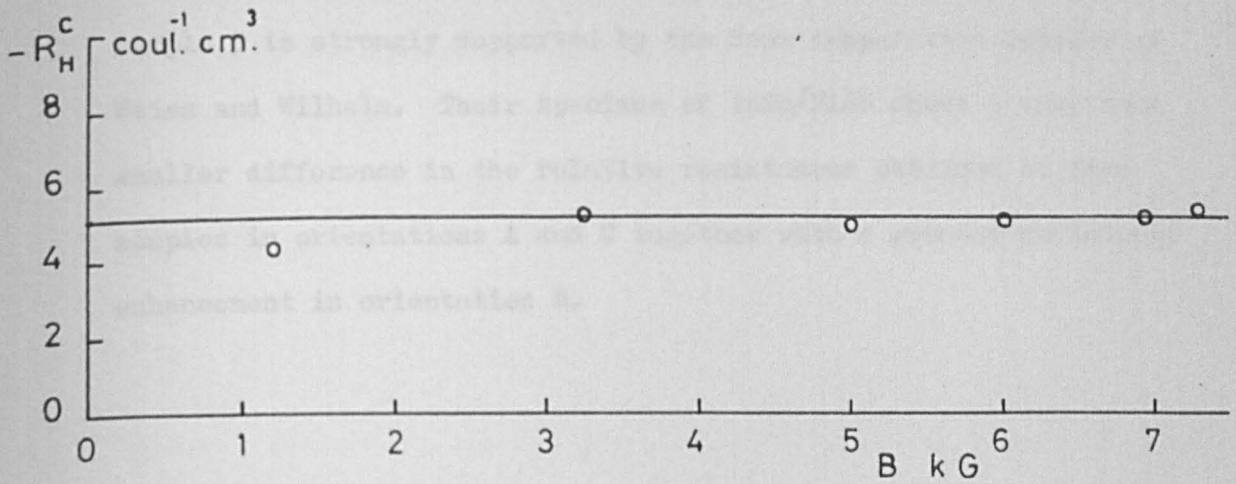


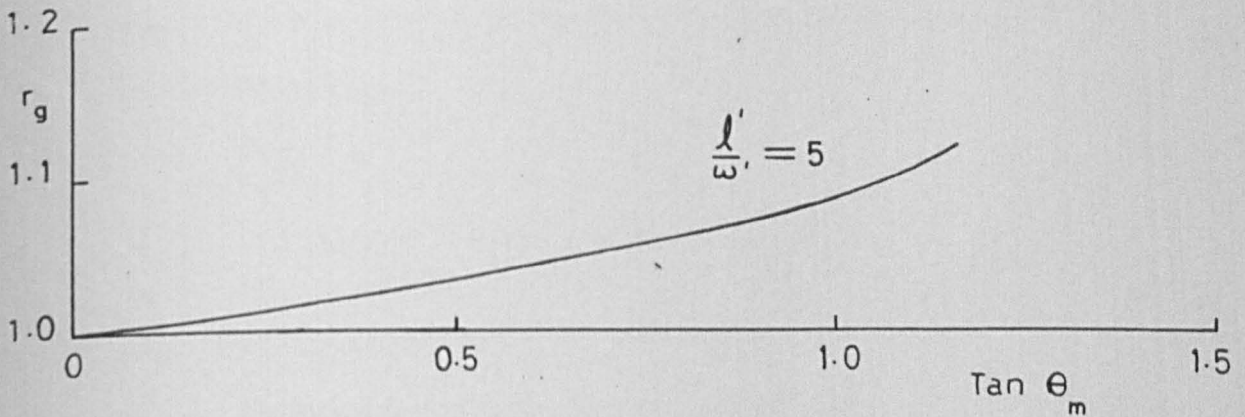
Fig.39

PROPERTIES OF InSb/NiSb SAMPLE 3 IN ORIENTATION C, AT 683°K

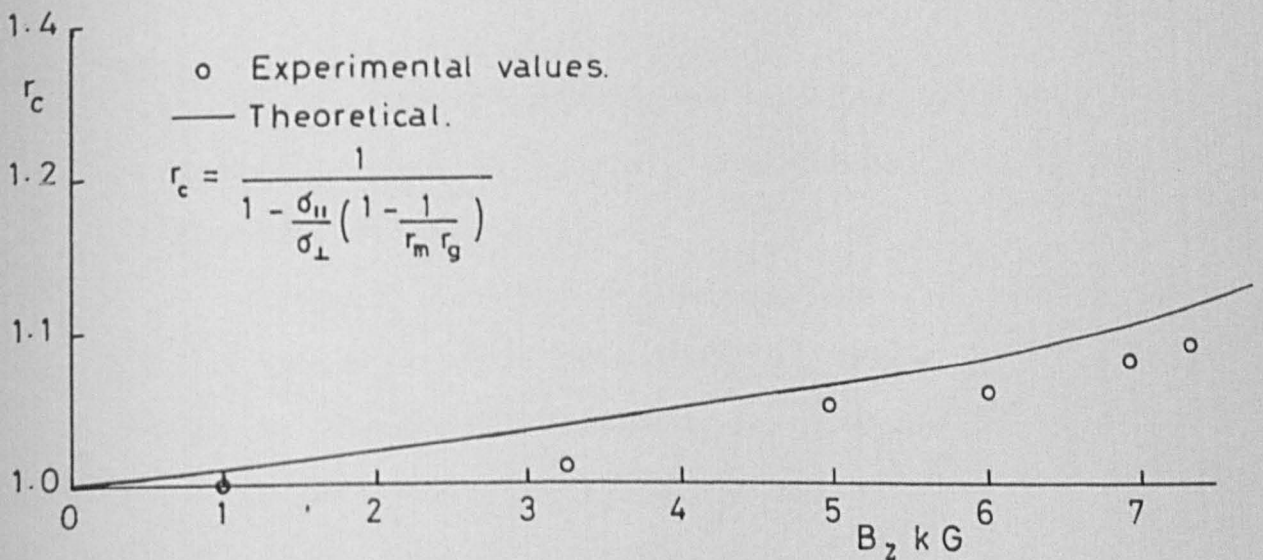
(a) Hall Coefficient (R_H^c) V Magnetic Field (B_z)



(b) Geometrical Resistance (r_g) V Tan Hall Angle ($\tan \theta_m$)



(c) Relative Resistance (r_c) V Magnetic Field (B_z)



as the temperature rises so that l'/ω' increases through σ_i approaching σ_N .

The conclusion that some inclusion misorientation exists in sample 3 is strongly supported by the room temperature results of Weiss and Wilhelm. Their specimen of InSb/NiSb shows a very much smaller difference in the relative resistances obtained in from samples in orientations A and C together with a greater resistance enhancement in orientation B.

7.2. Thermoelectric Power.

For the case of inclusion rods parallel to the applied temperature gradient, ΔT , the same model is used as for the case of electrical conductivity. The observed thermoelectric power of the InSb/NiSb sample, $\alpha_{||}$, is linked to the absolute thermoelectric powers of the constituents InSb and NiSb, α_i and α_N respectively by the relationship

$$\alpha_{||} = \alpha_i + \frac{\rho_i(1+\phi_2)(\alpha_N - \alpha_i)}{\rho_i(1+\phi_2) + \rho_N\phi_2^{-1}(1+\phi_2)} \quad (7.26)$$

where ρ_i and ρ_N are the resistivities of InSb and NiSb respectively and ϕ_2 is the ratio of the volume of NiSb to the volume of InSb. Clearly, if a different sample of InSb/NiSb is used to measure the thermoelectric power than is used to measure the electrical conductivity then $\phi_2 \neq \phi_1$.

From (7.26),

$$\alpha_{||} = \alpha_i - \left(\frac{\alpha_N - \alpha_i}{1 + M^{-1}\phi_2^{-1}} \right) \quad (7.27)$$

where $M = \rho_i/\rho_N$.

Measurements of the thermoelectric power of NiSb by Wagini show that $|\alpha_N| \ll |\alpha_i|$ at all temperatures, so that

$$\alpha_{||} = \frac{\alpha_i}{1 + M\phi_2} \quad (7.28)$$

For the case of inclusion rods perpendicular to the temperature gradient, the resultant thermoelectric power may be obtained from the model in 23(b).

Wagini has shown that at room temperature the thermoelectric power of NiSb, α_N , is small and positive and, therefore, if the total temperature drop over all the InSb layers is ΔT_i and the total temperature drop over the NiSb layers is ΔT_N , then

$$\alpha_{\perp} \Delta T = \alpha_i \Delta T_i - \alpha_N \Delta T_N \quad (7.29)$$

$$\therefore \alpha_{\perp} = \alpha_i \frac{\Delta T_i}{\Delta T} - \alpha_N \frac{\Delta T_N}{\Delta T}$$

From the flow of heat perpendicular to the InSb and NiSb layers, for $\phi_2 \leq 0.02$, from 7.3, $\Delta T_i / \Delta T \doteq K_1 / K_i \doteq 1$. It also follows that $\Delta T_N / \Delta T \doteq (K_1 / K_N) \phi_2$ is negligible since from Wagini's results $K_N \gg K_1$.

$$\alpha_{\perp} = \alpha_i \quad (7.30)$$

Since the absolute thermoelectric power of NiSb is small and positive then the application of a thermal gradient perpendicular to the inclusion rod axes causes circulating currents to develop around the inclusions. By applying a model that takes these currents into account, Liebmann and Millar obtained an expression which also reduced to (7.30) for small ϕ_2 .

Combining (7.28) and (7.30), it is possible to relate the thermoelectric powers measured in both orientations in the form

$$\alpha_{\parallel} = \frac{\alpha_{\perp}}{1 + M\phi_2} \quad (7.31)$$

$$\text{or } \alpha_{\perp} = \alpha_{\parallel} (1 + M\phi_2) \quad (7.32)$$

Equation (7.30) suggests that the thermoelectric power of a specimen of InSb/NiSb, with inclusions pointing perpendicular to the applied temperature gradient, approximate to that of the InSb matrix alone. This is so even if the volume ratio of NiSb to InSb is different from ϕ_2 , as in the case of electrical conductivity.

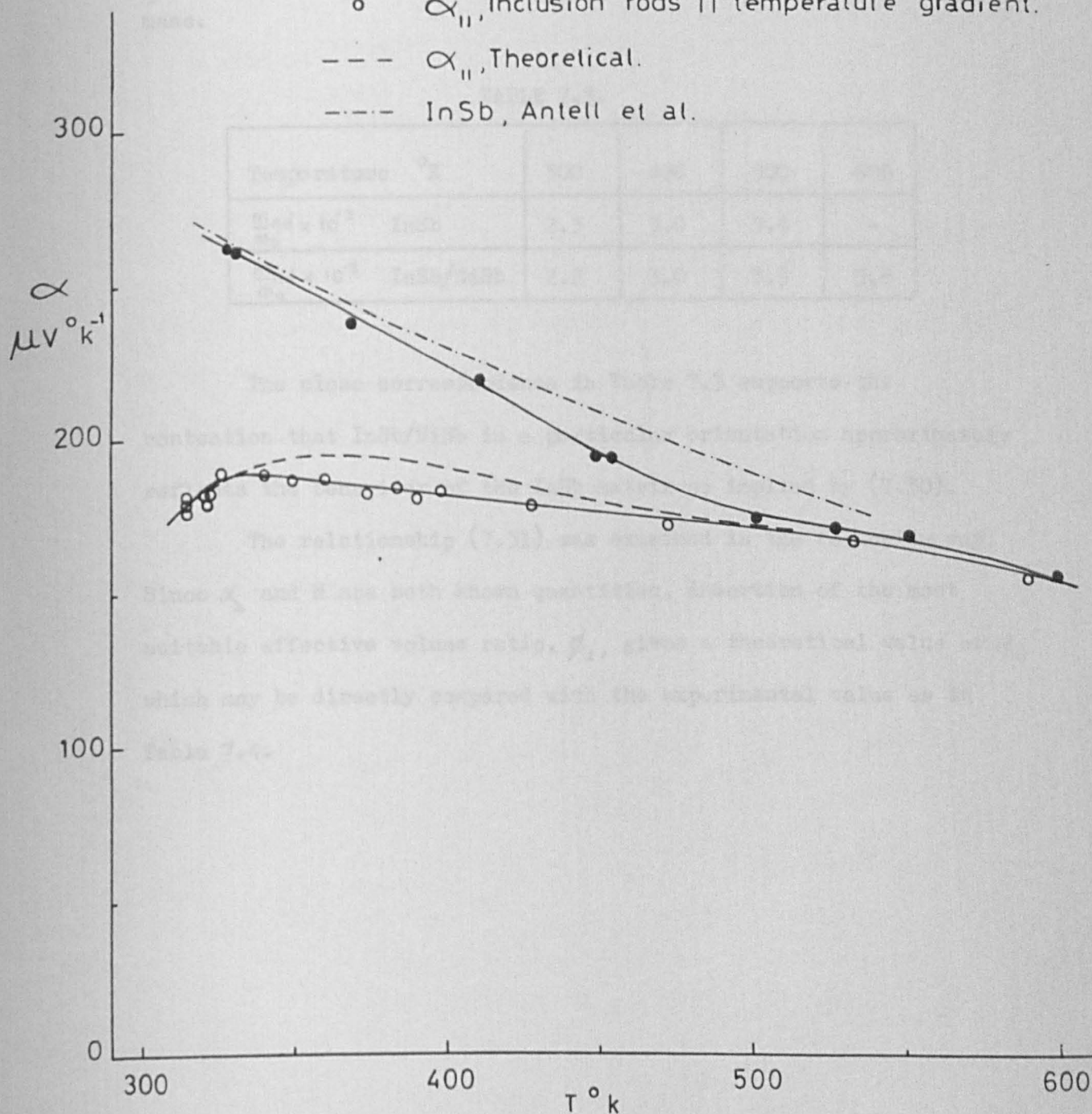
The experimental measurements of α_{\parallel} and α_{\perp} against temperature are shown together with those of Antell, Chasmar et al in Fig.40. Direct comparison shows that the thermoelectric power of InSb/NiSb is in fact slightly lower than that of InSb. However, (7.30) remains a reasonable approximation and the α_{\perp} v T curve has been used to provide values for the effective mass of the electrons

Fig. 40

THERMOELECTRIC POWER (α) V TEMPERATURE (T)

FOR InSb/NiSb

- α_{\perp} , Inclusion rods \perp temperature gradient.
- α_{\parallel} , Inclusion rods \parallel temperature gradient.
- α_{\parallel} , Theoretical.
- - - InSb, Antell et al.



at various temperatures. By making the same general assumptions as Chasmar and Stratton⁶⁴ the values of effective mass, m_{nd} obtained from InSb/NiSb may be compared with those obtained from InSb. Therefore, for purposes of comparison it has been assumed that InSb/NiSb has parabolic energy bands and carriers which undergo thermal acoustic scattering. Using the expressions derived in 2.2 the values contained in Table 7.3 were deduced, where m_0 is the electronic mass.

TABLE 7.3.

Temperature °K	300	400	500	600
$\frac{m_{nd}}{m_0} \times 10^{-2}$ InSb	2.3	3.0	3.4	-
$\frac{m_{nd}}{m_0} \times 10^{-2}$ InSb/NiSb	2.2	3.0	3.3	3.8

The close correspondence in Table 7.3 supports the contention that InSb/NiSb in a particular orientation approximately reflects the behaviour of the InSb matrix as implied by (7.30).

The relationship (7.31) was examined in the following way. Since α_1 and M are both known quantities, insertion of the most suitable effective volume ratio, ϕ_2 , gives a theoretical value of α_{11} which may be directly compared with the experimental value as in Table 7.4.

TABLE 7.4.

Effective volume ratio, $\phi_2 = 1.83 \times 10$						
Temperature T ^o K	294	331	367	409	450	528
Experimental (V/ ^o K) $\alpha_1 \doteq \alpha_i$	280	258	237	217	194	170
M	434	219	121	76.0	51.0	28.6
Theoretical (V/ ^o K) $\alpha_{ii} \doteq \alpha_1 (1 + M\phi_2)^{-1}$	156	184	194	190	178	162
Experimental (V/ ^o K) α_{ii}	156	189	185	180	175	166

The calculated α_{ii} v T curve is shown dashed in Fig.40 and may be seen to follow the experimental α_{ii} v T curve in a qualitative manner.

7.3. Thermal Conductivity.

The same models as were used to discuss the electrical conductivity of InSb/NiSb were employed. When a temperature gradient is applied parallel to the axes of the inclusions, then the model in 23(a) is used to describe the flow of heat through the InSb and NiSb layers. In analogy to (7.2) the equation

$$K_{||} = K_i + K_N \phi_2 \quad (7.33)$$

may be written. $K_{||}$ is the thermal conductivity of the InSb sample and K_i and K_N are the thermal conductivities of the InSb and NiSb layers. Since the same sample was used to measure $K_{||}$ and $\alpha_{||}$ the same volume ratio ϕ_2 must be retained.

When a temperature gradient is applied perpendicular to the axes of the inclusions, in analogy to (7.3),

$$K_{\perp} = \frac{K_i (1 + \phi_2)}{(1 + \phi_2/N)} \quad (7.34)$$

where $N = K_N/K_i$.

From the results of Wagini N has a value of 5.2 at 300°K. Since the values of resistivity and thermal conductivity show that the Wiedemann Franz law [i.e. $K_N = (\pi^2/3)(k/e)^2 \sigma_N T$] is obeyed by NiSb at 300°K and 400°K the value of K_N has been calculated assuming it is also obeyed at 500°K. The value of K_N deduced in this way showed that N increased to a value of 8.2. From the orders of magnitude involved (7.34) reduced to

$$K_{\perp} \doteq K_i (1 + \phi_2) \doteq K_i \quad (7.35)$$

From (7.33) and (7.35),

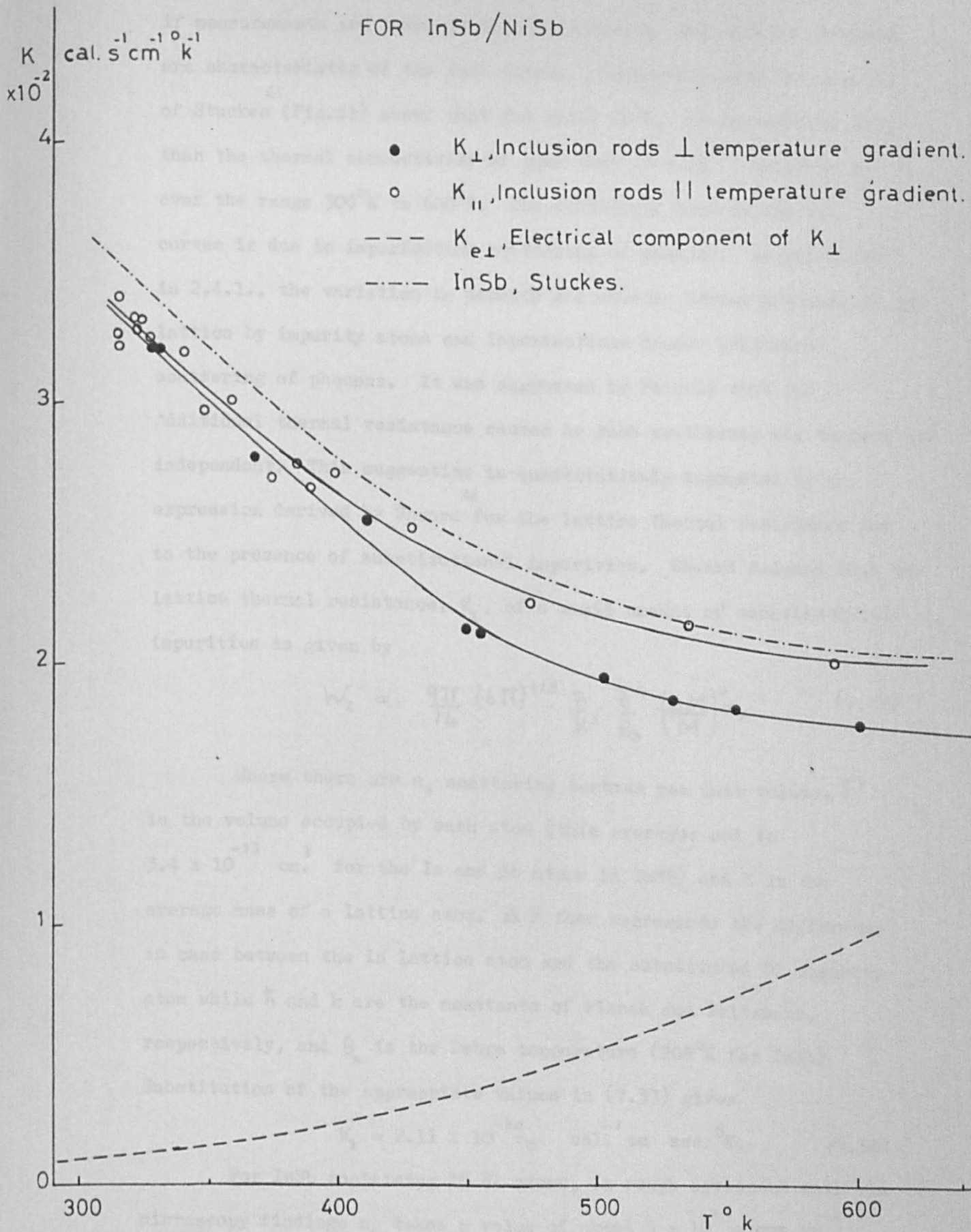
$$K_{||} = K_{\perp} (1 + N\phi_2) \quad (7.36)$$

In this case also (7.35) remains true even if a different volume ratio is present in the sample in which the inclusions are orientated perpendicular to the temperature gradient, so long as the

Fig. 41

THERMAL CONDUCTIVITY (K) V TEMPERATURE (T)

FOR InSb/NiSb



order of magnitude is the same as that of ρ_2 . This suggests that if measurements are taken in this orientation, the results obtained are characteristic of the InSb matrix. Comparison with the results of Stuckes⁶⁵ (Fig.41) shows that the value of K_1 is appreciably lower than the thermal conductivity of pure InSb (2×10^{15} acceptors cm^{-3}), over the range 300°K to 600°K . The difference between the two curves is due to imperfection scattering of phonons. As mentioned in 2.4.1., the variation in density and elastic forces produced in the lattice by impurity atoms and imperfections causes additional scattering of phonons. It was suggested by Peierls that the additional thermal resistance caused by such scattering was temperature independent. This suggestion is quantitatively supported by an expression derived by Sheard⁶⁶ for the lattice thermal resistance due to the presence of substitutional impurities. Sheard deduced that the lattice thermal resistance, W_1 , of a small amount of substitutional impurities is given by

$$W_1 = \frac{9\pi}{14} (6\pi)^{1/3} \frac{\hbar}{k^2} \frac{\delta^4}{\theta_D} \left(\frac{\Delta M}{M}\right)^2 n_s \quad (7.37)$$

Where there are n_s scattering centres per unit volume, δ^3 is the volume occupied by each atom (this averages out to $3.4 \times 10^{-23} \text{ cm}^3$ for the In and Sb atoms in InSb) and M is the average mass of a lattice atom. ΔM then represents the difference in mass between the In lattice atom and the substituted Ni impurity atom while \hbar and k are the constants of Planck and Boltzmann, respectively, and θ_D is the Debye temperature (208°K for InSb). Substitution of the appropriate values in (7.37) gives

$$W_1 = 2.11 \times 10^{-20} n_s \text{ cal.}^{-1} \text{ cm sec.}^\circ\text{K.} \quad (7.38)$$

For InSb containing 1% Ni atoms, in rough agreement with the microscopy findings n_s takes a value of about $3 \times 10^{20} \text{ atoms cm}^{-3}$.

The lattice thermal resistance arising from the substitution of 3×10^{20} atoms of Ni atoms for In atoms in InSb by (7.38) takes a temperature independent value of order $6 \text{ cal.}^{-1} \text{ cm. sec.}^{\circ}\text{K}$.

The experimental results show that $(W/W) (K/K)$ takes values of 3 at 400°K and 7 at 500°K . Therefore, the expression derived by Sheard gives a value of the right order of magnitude for the observed increase in thermal resistance, but does not, however, provide a complete explanation of its temperature dependence.

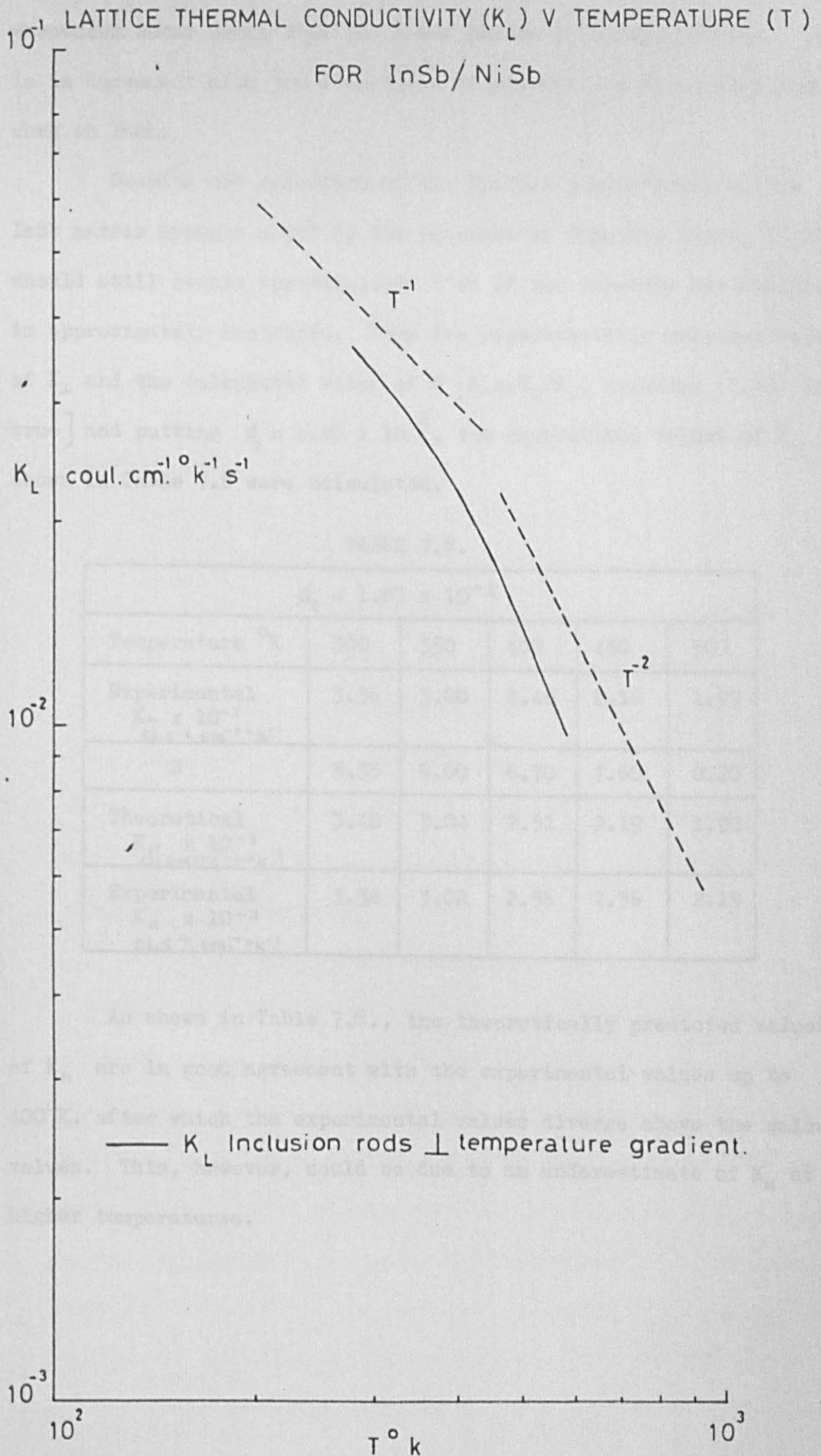
The variation of the electronic component of the thermal conductivity may be determined as outlined in 2.4.2. The values of γ , q , A_n , B_n and B_p obtained at various temperatures are given in Table 7.5 below.

TABLE 7.5

Temperature	γ	q	A_n	B_n	B_p
$\sim 350^{\circ}\text{K}$	-1.1	2	3.3	3.7	3.5
$\sim 450^{\circ}\text{K}$	-1.5	0	2.7	2.9	2.5
$\sim 550^{\circ}\text{K}$	-1.9	0	2.8	3.1	2.5

The above results allowed the electronic component of the thermal conductivity to be calculated from (2.58). The results of the calculation are shown as K_{e1} in Fig.41, together with the experimental plots of $K_{||}$ and K_{\perp} against temperature. The lattice component K_{L1} was then determined from (2.56) and is shown in Fig.42. This confirms that the lattice component of InSb/NiSb, K_{L1} , tends from a T^{-1} variation at 300°K to a T^{-2} variation at 580°K . Therefore, as the temperature rises an increasing number of 4 phonon

Fig. 42



processes occur along with the three phonon processes present. This is in agreement with the deductions of Stuckes and Steigmeier from work on InSb.

Despite the reduction of the thermal conductivity of the InSb matrix brought about by the presence of impurity atoms, (7.36) should still remain approximately true if the impurity distribution is approximately isotropic. From the experimentally measured values of K_{\perp} and the calculated value of N [i.e. K_N/K_{\perp} , assuming (7.35) to be true] and putting $\phi_2 = 1.83 \times 10^{-3}$, the theoretical values of K_{\parallel} shown in Table 7.6 were calculated.

TABLE 7.6.

$\phi_2 = 1.83 \times 10^{-3}$					
Temperature $^{\circ}\text{K}$	300	350	400	450	500
Experimental $K_{\perp} \times 10^{-2}$ $\text{cl. s}^{-1} \text{ cm}^{-1} \text{ } ^{\circ}\text{K}^{-1}$	3.36	3.00	2.48	2.16	1.95
N	5.35	6.00	6.70	7.60	8.20
Theoretical $K_{\parallel} \times 10^{-2}$ $\text{cl. cm}^{-1} \text{ s}^{-1} \text{ } ^{\circ}\text{K}^{-1}$	3.40	3.04	2.51	2.19	1.98
Experimental $K_{\parallel} \times 10^{-2}$ $\text{cl. s}^{-1} \text{ cm}^{-1} \text{ } ^{\circ}\text{K}^{-1}$	3.38	3.02	2.56	2.36	2.19

As shown in Table 7.6., the theoretically predicted values of K_{\parallel} are in good agreement with the experimental values up to 400°K , after which the experimental values diverge above the calculated values. This, however, could be due to an underestimate of K_N at the higher temperatures.

7.4. Discussion.

Using a simple model the anisotropy of the electrical conductivity and thermoelectric power has been explained in terms of an apparent volume ratios of NiSb in InSb. However, the apparent volume ratio necessary to explain the electrical conductivity results ϕ_1 was 6.1×10^{-4} whereas a volume ratio, , three times larger than this was necessary to explain the thermoelectric power results.

Some light is shed on the values of ϕ_1 and ϕ_2 by examining the constriction of the lines of current flow brought about by the inclusions. When the inclusions lie perpendicular to the current flow the electrical conductivity is characteristic of the matrix so that the shorting of the matrix caused by the inclusions is counteracted by the increase in resistance caused by constricting the current flow. When the inclusions lie parallel to the current flow a similar increase in resistance arises from the constriction of the current flow but the shorting is enhanced by the greater length of inclusion in the direction of current flow, so that the electrical conductivity is increased.

The electron microscopy enabled the structure of the InSb/NiSb used in the present work to be simplified into "even" layers containing regularly placed inclusions, separated by "odd" layers of pure InSb. The inclusions in each even layer were, however, laterally displaced with respect to those in the next even layer. Further, adapting the theory of constrictions developed by Holm,⁶⁷ a highly conducting inclusion of radius A may be assumed to constrict lines of current flow within a hemisphere of radius $14A$ to flow through it. This meant that current lines constricted to flow through an inclusion in an even layer, did not flow through an inclusion in the

next similar layer. On the basis that the current lines flowed through the matrix parallel to the inclusions and through matrix-inclusion-matrix paths the apparent volume ratios ϕ_1 (6.1×10^{-4}) and ϕ_2 (1.83×10^{-3}) were then found to correspond to real volume ratios of 5.5×10^{-3} and 7.4×10^{-3} , respectively. The implication that the true volume ratio of the thermoelectric power sample is greater than that of the electrical conductivity sample by 30% is certainly a reasonable one, considering the variation in inclusion density apparent in the electron micrographs. Both real volume ratios, however, remain of comparable order to the previously estimated volume ratio of 8×10^{-3} .

CHAPTER 8CONCLUSION

Stereoscan electron microscopy has confirmed that the InSb/NiSb sample was composed of about 1% by volume of NiSb in a matrix of InSb. The NiSb was included in the form of orientated rods of length 2.2μ and diameter 0.72μ , whose density varied throughout the sample.

The "magnetoresistance", electrical conductivity and Hall coefficient have been measured from 77°K to 700°K using the designed sample holder, cryostat and furnace and the chopped D.C. technique of Dauphinee and Mooser.

Samples were orientated so that the current flowed parallel and perpendicular to the rods, with the magnetic field always perpendicular to the current.

The most striking anisotropy observed occurred in the changes in resistivity brought about by the application of a magnetic field. According to its orientation, the sample resistivity increased by factors 9.0, 2.8 and 1.4 respectively, in a 7kG magnetic field.

The electrical conductivity observed when the current flowed parallel to the inclusions was higher than that observed when the current flowed perpendicular to the inclusions by a factor of 16 at 77°K , but only by a factor of 1.2 at 300°K . When the current flowed perpendicular to the inclusions the electrical conductivity of the sample was approximately that of pure InSb. Similarly, the Hall coefficient was most representative of the matrix when the inclusions were parallel to the transverse magnetic field.

At 320°K , with the temperature gradient parallel to the inclusions the thermoelectric power of $184\mu\text{V}^{\circ}\text{K}^{-1}$ was markedly lower than the value of $265\mu\text{V}^{\circ}\text{K}^{-1}$ obtained with the temperature gradient

perpendicular to the inclusions. The corresponding values at 600°K were, however, almost identical at about $155\mu\text{V}^{\circ}\text{K}^{-1}$. The thermo-electric power obtained with the temperature gradient perpendicular to the inclusions was fairly close to that obtained from pure InSb, although the temperature variation appeared to be slightly different.

The thermal conductivity was lower when the temperature gradient was perpendicular to the inclusions than when it was parallel to the inclusions. The difference which was less than 3% at 320°K , increased to 10% at 600°K . When the temperature gradient was perpendicular to the inclusions a similar behaviour to that of pure InSb was observed, but the lattice thermal conductivity of InSb/NiSb was noticeably lower over the whole range of measurement. The increased thermal resistance was of the order of magnitude which might be expected if 1% of the Indium atoms are replaced by Nickel atoms.

By adopting simple layer models for the eutectic it has been possible to give a qualitative account of the various anisotropies described, in terms of volume ratios which have been shown to be of the appropriate order of magnitude.

The most useful practical features of InSb/NiSb appear to be the result of its structural anisotropy. At 77°K , the anisotropy in electrical conductivity would enable the material to be used as a current regulator, while at room temperature the large magneto-resistance available could allow it to be used as a variable resistance which does not require manual adjustment. The increase in resistance of a sample of InSb/NiSb in a given magnetic field is, however, lower than is produced by a Corbino disc sample of pure InSb. On the other hand, the eutectic allows the "magnetoresistance" of short broad elements to be combined with the high resistance of

long, thin samples. Further, the ninefold increase in resistance produced by the present sample in a 7kG. magnetic field, may be enhanced by producing a more uniform microstructure, as comparison with the results of Wilhelm and Weiss confirms.

Since both the electrical conductivity and the magnetoresistance of the material are strongly temperature dependent, the anisotropies and hence the usefulness of the material can only be maintained under conditions of stringent temperature control.

1. J. Wilhelm and H. Weiss, *Z. Phys.*, **113**, 451 (1940).
2. J. Wilhelm and H. Weiss, *Z. Phys.*, **113**, 451 (1940).
3. J. Wilhelm and H. Weiss, *Z. Phys.*, **113**, 451 (1940).
4. J. Wilhelm and H. Weiss, *Z. Phys.*, **113**, 451 (1940).
5. J. Wilhelm and H. Weiss, *Z. Phys.*, **113**, 451 (1940).
6. J. Wilhelm and H. Weiss, *Z. Phys.*, **113**, 451 (1940).
7. J. Wilhelm and H. Weiss, *Z. Phys.*, **113**, 451 (1940).
8. J. Wilhelm and H. Weiss, *Z. Phys.*, **113**, 451 (1940).
9. J. Wilhelm and H. Weiss, *Z. Phys.*, **113**, 451 (1940).
10. J. Wilhelm and H. Weiss, *Z. Phys.*, **113**, 451 (1940).
11. J. Wilhelm and H. Weiss, *Z. Phys.*, **113**, 451 (1940).
12. J. Wilhelm and H. Weiss, *Z. Phys.*, **113**, 451 (1940).
13. J. Wilhelm and H. Weiss, *Z. Phys.*, **113**, 451 (1940).
14. J. Wilhelm and H. Weiss, *Z. Phys.*, **113**, 451 (1940).
15. J. Wilhelm and H. Weiss, *Z. Phys.*, **113**, 451 (1940).
16. J. Wilhelm and H. Weiss, *Z. Phys.*, **113**, 451 (1940).
17. J. Wilhelm and H. Weiss, *Z. Phys.*, **113**, 451 (1940).
18. J. Wilhelm and H. Weiss, *Z. Phys.*, **113**, 451 (1940).
19. J. Wilhelm and H. Weiss, *Z. Phys.*, **113**, 451 (1940).
20. J. Wilhelm and H. Weiss, *Z. Phys.*, **113**, 451 (1940).

R E F E R E N C E S

1. W. Heitler & F. London Z. Phys. 44, 455, 1927.
2. A. Sommerfeld. Z. Physik 47, 1, 1928.
3. F. Bloch Z. Physik 52, 555, 1928.
4. R. de L. Kronig & W.G. Penney. Proc. Phys. Soc. (London) A 130, 499, 1930.
5. A.H. Wilson Proc. Roy. Soc. A 133, 458 e 134, 277. 1931.
6. P. Debye Ann. Physik, 39, 789, 1912.
7. H. Ehrenreich J. Phys. Chem. Solids, 2, 131, 1957.
8. E.M. Conwell and V.F. Weisskopf Phys. Rev. 77, 388, 1950.
9. M.S. Sodha Prog. in Semiconductors 3, 153, 1958.
10. C. Eginsoy Phys. Rev. 79, 1013, 1950.
11. W.T. Read Phil. Mag. 45, 775, 1119, 1934, 46, 111, 1954.
12. C.A. Coulson, L.B. Redei & D Stocker Proc. Roy. Soc. 270, 357 ff., 1962.
13. N.N. Sirota, N.M. Olekhnovich & E.M. Gololobov Dol. Acad. Nauk. S.S.S.R. 130 ff., 160, 660. 1961.
14. V. Roberts & J.E. Quarrington. J. Electronics 1, 151, 1955.
15. G. Desselhaus et al. Phys. Rev. 98, 556, 1955.
16. E.O. Kane J. Phys. Chem. Solids 1, 294, 1937.
17. H. Y. Fan and G.W. Gobeli Phys. Rev. Lett. 4, 546, 1960.
18. C.H. Champness Phys. Rev. Lett. 1, 439, 1958.
19. J.C. Wooley, B.A. Smith, J.A. Evans Solid State Physics in Electronics and Telecommunications. Vol. 2, Acad. Press, N Y. p. 802.

20. J.C. Wooley, J.A. Evans, Proc. Phys. Soc. 78, 354, 1961.
21. M.S. Abrahams, R. Braunstein and F.D. Rosi. Metallurgical Soc. Conf. V.5. Props. of Elemental & Compound Semiconductors. Interscience, N-Y p.275.
22. F. Oswald Z. Naturforsch 14a, 374, 1959.
23. F.S. Galasso Journal of Metals, 1967.
24. W.K. Liebmann and E.A. Millar, J. App. Phys. 34, 2653, 1963.
25. H. Wilhelm and H. Weiss Zeit. fur Physik 176, 399, 1963.
26. H. Wagini Z. Naturforsch. 21, 362, 1966.
27. H. Ehrenreich J. Phys. Chem. Solids. 9, 129, 1959.
28. C. Hilsum & R. Barrie Proc. Phys. Soc. (L) 71, 676, 1958.
29. E. Steigmeier & G. Busch Helveticia Physica Acta 34, 28, 1960.
30. I. Isenberg, B.R. Russell and R.F. Green, Rev. Sci. Inst. 19, 685, 1948.
31. J. Volger Phys. Rev. 79, 1023, 1950.
32. R.F. Wick J. App. Phys. 25, 741, 1954.
33. C. Hilsum and R. Barrie "3-5" Semiconductors Pergamon Press.
34. R.K. Willardson & A.C. Beer. See "Hall Effect and Related Phenomena." by E.H. Putley.
35. H. Welker & H. Weiss Z. Phys. 138, 322, 1954.
36. C.A. Simmons. J. App. Phys. 32, 1970, 1961.
37. H.J. Lippmann & F. Kuhrt Z. Naturforsch 13a, 462, 1958.
38. H.J. Lippmann & F. Kuhrt Z. Naturforsch 13a, 474, 1958.
39. C. Herring J. App. Phys. 31, 1939, 1960.

40. Juretsche, Landsauer & Swanson J. App. Phys. 27, 838, 1936.
41. J. McDougall & E.C. Stoner. Trans. Roy. Soc. A 237, 67,
1939.
42. Wright Proc. Phys. Soc. (L) A64, 350, 1951.
43. O. Madelung Handbuch der Physik, Springer Verlag 1,
20, 1957.
44. R. Peierls Ann Physik 3, 1055, 1929.
45. I. Pomeranchuk Phys. Rev. 60, 820, 1941.
46. B. Abeles J. Phys. Chem. Sol. 8, 340, 1959.
47. A.D. Stuckes Phil. Mag. 5, 84, 1960.
48. G.C. Danielson Phys. Rev. 130, 1743, 1963.
49. G.A. Slack and C.G. Glassbrenner Phys. Rev. 134A, 1058,
1964.
50. H.B.G. Casimir Physica, 5, 495, 1938.
51. G.K. White & S.B. Woods Phys. Rev. 103, 569, 1956.
52. Curruthers et al. Proc. Roy. Soc. (L) A238, 502.
53. O. Madelung Encyclopedia of Physics 20, p.88, 1957.
54. T.M. Dauphinee & E. Mooser Rev. Sci. Inst. 26, 660, 1955.
55. A.D. Stuckes & R.P. Chasmar Proc. of the Rugby Conference.
Phys. Soc., 119, 1957.
56. R.W. Powell Proc. Phys. Soc. (L) 46, 659, 1934.
57. O.G. Folberth, O. Madelung & H. Weiss Z. Naturforsch
9a, 954, 1956.
58. R.P. Chasmar, G.R. Antell, C.H. Champness & E. Cohen
Proc. of the Rugby Conference. Phys. Soc. 99, 1957.
59. R.P. Chasmar & C.H. Champness J. Electronics 3, 494, 1957.
60. H. Weiss Z. Naturforsch 12a, 80, 1957.

61. E.H. Putley (C19) Proc. Phys. Soc. 73, 128 1959.
62. H.J. Hrostowski et al. Phys. Rev. 100, 1672, 1955.
63. O. Madelung Z. Naturforsch 9a, 527, 1954.
64. R.P. Chasmar & R. Stratton Phys. Rev. 102, 1686, 1956.
65. A.D. Stuckes Phys. Rev. 107, 427.
66. Sheard. Phil. Mag., 5., 887, 1960.
67. R. Holm. See "Electrical Contacts, Theory and Application"
Springer Verlag, Berlin 1967.
68. C.H. Champness J. Elect. 4, 201, 1958.

A P P E N D I X 1

EXPERIMENTAL RESULTS ON INDIUM ARSENIDE

1.1. Variation of Hall Coefficient, R_H , with Temperature T.

Magnetic Field, $B_2 = 7.328$ kG.

T	$T^{-1} \text{ } ^\circ\text{K}^{-1}$	R_H coul. $^{-1}\text{cm}^3$	T $^\circ\text{K}$	$T^{-1} \text{ } ^\circ\text{K}^{-1}$ $\times 10^3$	R_H coul. $^{-1}\text{cm}^3$
151.5	6.60	464	293.6	3.41	403
156.1	6.41	453	339.0	2.95	357
156.6	6.39	458	380.5	2.63	283
161.8	6.18	450	418.9	2.39	192
183.5	5.45	446	469.3	2.13	103
187.0	5.35	443	533.0	1.88	44.9
208.5	4.80	439	547.0	1.83	37.0
213.0	4.61	429	620.8	1.61	23.9
219.7	4.55	429	634.4	1.58	16.4
226.3	4.42	420	700.2	1.43	9.03
250.0	4.00	415	734.6	1.36	7.41
			806.7	1.24	4.82

1.3. Variation of Electron Mobility, μ_e , with Temperature T

T °K	σ $\Omega^{-1}\text{cm}^{-1}$	$-R_H$ Coul. $^{-1}\text{cm}^3$	$\mu_e = R_H \sigma$
156.0	53.2	453	24,100
179.0	52.5	450	23,600
208.5	51.5	439	22,600
226.3	50.4	420	21,800
250.5	49.9	415	20,700
293.6	48.8	403	19,600
339.0	50.6	357	18,200
380.5	60.1	283	17,000
419.0	86.7	192	16,600
469.3	153	103	15,800
533.0	312	44.9	14,000
547.0	362	37.0	13,400
620.8	538	23.9	12,900
634.3	683	16.4	11,200
701.0	1160	9.03	10,500
731.5	1170	7.41	8,660
809	1600	4.82	7,710

1.3. Variation of Electron Mobility, μ_e , with Temperature T

T °K	σ $\Omega^{-1}\text{cm}^{-1}$	$-R_H$ Coul. $^{-1}\text{cm}^3$	$\mu_e = R_H \sigma$
156.0	53.2	453	24,100
179.0	52.5	450	23,600
208.5	51.5	439	22,600
226.3	50.4	420	21,800
250.5	49.9	415	20,700
293.6	48.8	403	19,600
339.0	50.6	357	18,200
380.5	60.1	283	17,000
419.0	86.7	192	16,600
469.3	153	103	15,800
533.0	312	44.9	14,000
547.0	362	37.0	13,400
620.8	538	23.9	12,900
634.3	683	16.4	11,200
701.0	1160	9.03	10,500
731.5	1170	7.41	8,660
809	1600	4.82	7,710

1.4. Room Temperature Magnetoresistance and Hall Coefficient

Room Temperature = 293.1 °K

Magnetic Field B_z kG.	Hall Coef- ficient (-) R_H coul. \cdot -1cm ³	Resistivity ρ_B cm $\times 10^{-2}$	$\frac{\rho_B}{\rho_0}$	$\frac{\Delta\rho_B}{\rho_0}$ $\times 10^{-3}$
0	392	2.049	1.000	0
1.191	394	2.058	1.004(5)	4.5
2.235	394	2.145	1.009(6)	9.6
4.205	395	2.102	1.026(1)	20.6
4.985	399	2.123	1.035(7)	36.7
6.011	402	2.149	1.049(4)	49.4
6.927	405	2.178	1.063(2)	63.2
7.328	406	2.185	1.067(6)	67.6
7.796	..	2.199	1.073(0)	73.0

A P P E N D I X 2

2.1. Experimental Results on InSb/NiSb. Sample 1
in Orientation A.

2.1.1. Variation of Hall Coefficient, R_H^A , Electrical
Conductivity, σ , and $|R_H^A|\sigma$, with Temperature T

$T^{\circ}K$	$T^{-1} \times 10^3$ $^{\circ}K^{-1}$	σ $\Omega^{-1} \text{cm}^{-1}$	R_H^A $\text{cm}^3 \text{ccul.}^{-1}$	$ R_H^A \sigma$ $\text{cm}^2 \text{V}^{-1} \text{s}^{-1}$
77	13.0	0.129	+ 7,620	983
78	12.8	0.138	+ 6,930	957
88	11.4	0.174	-	-
102	9.80	0.230	+ 2,810	647
106	9.43	0.271	+ 1,600	434
122	8.20	0.500	- 3,490	246
124	8.07	0.524	- 6,930	3,630
134	7.46	-	-29,000	-
154	6.51	2.52	-	-
165	6.06	4.17	-12,800	53,400
205	4.88	22.0	- 3,640	80,000
251	3.98	93.5	- 866	81,000
256	3.77	128	- 628	76,000
294	3.40	212	- 327	69,300

cont.

$T^{\circ}\text{K}$	$T^{-1} \times 10^3$ $^{\circ}\text{K}^{-1}$	σ $\Omega^{-1}\text{cm}^{-1}$	R_H^A $\text{cm}^3\text{coul.}^{-1}$	$ R_H^A \sigma$ $\text{cm}^2\text{V}^{-1}\text{s}^{-1}$
331	3.02	381	- 163	62,100
367	2.73	605	- 90.5	54,800
409	2.44	920	- 50.3	46,200
450	2.22	1,240	- 32.0	39,800
528	1.89	1,906	- 15.2	29,000
581	1.72	2,280	- 10.7	24,400
623	1.60	2,590	- 8.06	20,800
698	1.43	2,920	- 5.50	16,100

2.1.2. Variation of "Magnetoresistance" r_A , and Hall Coefficient R_H^A , with Magnetic Field, B_z , at 106°K .

B_z kG	σ_B $\Omega^{-1}\text{cm}^{-1}$	$r_A = \frac{\sigma}{\sigma_B}$	$+ R_H^A$ $\text{cm}^3\text{coul.}^{-1}$
0	0.271(σ)		
2.235	0.268	1.01	1580
4.205	0.263	1.03	1600
4.985	0.259	1.05	1610
6.010	0.253	1.07	1610
6.927	0.251	1.08	1600
7.328	0.249	1.09	1600

2.1.3. Variation of Hall Coefficient, R_H^A , "Magnetoresistance", r_A , and Hall Angle, θ_m^0 , with Magnetic Field, B_z , at $294^\circ K$

B_z kG	R_H^A $cm^3 \cdot coul^{-1}$ (-)	Tan θ_m	θ_m^0	r_g	r_m	$r_A = r_m r_g$ (theory)	r_A (expt)
1.191	328	0.82	39.5	1.020	1.010	1.03	1.02
2.235	325	1.51	56.5	1.040	1.030	1.07	1.07
3.272	330	2.14	65.0	1.060	1.060	1.12	1.12
4.985	329	3.11	72.2	1.090	1.140	1.21	1.22
6.011	329	3.48	74.0	1.100	1.200	1.32	1.31
6.927	331	3.78	75.2	1.110	1.270	1.41	1.39
7.328	334	3.91	75.5	1.110	1.300	1.44	1.44

2.1.4. Variation of Hall Coefficient, R_H^A , "Magnetoresistance", r_A , and Hall Angle, θ_m^0 , with Magnetic Field, B_z , at $367^\circ K$

B_z kG	R_H^A $cm^3 \cdot coul^{-1}$ (-)	Tan θ_m	θ_m^0	r_g	r_m	r_A (theory)	r_A (expt)
1.191	88.0	0.65	33.0	1.020	1.005	1.02(5)	1.02
3.272	91.5	1.73	60.0	1.035	1.036	1.07	1.05
4.985	92.0	2.52	68.4	1.050	1.084	1.14	1.12
6.011	91.6	2.94	71.2	1.060	1.122	1.19	1.20
6.927	91.2	3.27	73.0	1.067	1.162	1.24	1.22
7.328	91.0	3.40	73.6	1.070	1.181	1.26	1.30

2.1.5. Variation of Hall Coefficient, R_H^A , "Magnetoresistance"
 r_A and Hall Angle θ_m^0 with Magnetic Field at 528°K

B_z kG	R_H^A $\text{cm}^3 \text{coul}^{-1}$	Tan θ_m	θ_m^0	r_g	r_m	$r_A = r_g r_m$ (theory)	r_A (expt)
1.191	14.7	0.345	19.0	1.005	1.00	1.01	1.01
3.272	15.0	0.940	43.2	1.012	1.01	1.02	1.02
4.985	15.3	1.42	54.8	1.017	1.023	1.04	1.04
6.011	15.2	1.68	59.3	1.020	1.034	1.06	1.06
6.927	15.2	1.93	62.6	1.024	1.045	1.07	1.08
7.328	15.2	2.03	63.8	1.025	1.051	1.08	1.10

2.1.6. Variation of Hall Coefficient, R_H^A , "Magnetoresistance"
 r_A , and Hall Angle, θ_m^0 , with Magnetic Field at 698°K

B_z kG	R_H^A $\text{cm}^3 \text{coul}^{-1}$	Tan θ_m	θ_m^0	r_g	r_m	$r_A = r_g r_m$ (theory)	r_A (expt)
1.191	5.00	0.178	10.1	1.005	1.000	1.00	1.00
3.272	5.70	0.485	25.9	1.010	1.003	1.01	1.01
4.985	5.60	0.740	36.5	1.014	1.007	1.02	1.02
6.011	5.40	0.890	41.7	1.020	1.011	1.03	1.03
6.927	5.40	1.03	46.0	1.020	1.014	1.03	1.04
7.328	5.40	1.09	47.5	1.021	1.016	1.04	1.05

2.2. Results On INSb/NISb Sample 2 in Orientation B

2.2.1. Variation of Hall Coefficient, R_H^B , Electrical Conductivity, σ and $|R_H^B|\sigma$ with Temperature T.

$T^{\circ}K$	$T^{-1} \times 10^3$	σ $\Omega^{-1}cm^{-1}$	R_H^B $cm^3 coul.^{-1}$	$ R_H^B \sigma$ $cm^2V^{-1}S^{-1}$
77	13.0	0.130	+ 582	75.5
106	9.43	0.251	+ 295	74.0
119	8.40	0.380	+ 180	68.4
121	8.26	-	+ 140	-
139	7.21	1.03	-	-
166	6.00	4.06	- 151	613
175	5.70	7.50	- 230	1,725
199	5.02	19.9	- 362	7,200
230	4.35	50.8	-	-
255	3.91	98.3	- 298	29,300
293	3.40	210	-	-
326	3.07	352	- 121	39,400
377	2.65	659	- 60.0	39,400
421	2.37	1,070	- 35.3	37,800
455	2.18	1290	- 25.4	32,800
529	1.89	1,910	- 14.6	27,900
547	1.83	2,200	10.8	24,000
636	1.57	2,640	- 7.08	18,700
683	1.47	2,880	- 5.75	16,600
696	1.44	2,920	- 5.20	15,100

2.2.2. Variation of "Magnetoresistance" r_B and Hall Coefficient, R_H^B , with Magnetic Field, B_z , at 106°K

B_z kG	σ_B $\Omega^{-1}\text{cm}^{-1}$	$r_B = \frac{\rho}{\rho_0}$	(+) R_H^B $\text{cm}^3\text{coul}^{-1}$
0	0.251	1	..
2.235	0.248	1.01	295
4.405	0.246	1.02	297
4.985	0.241	1.04	301
6.011	0.235	1.07	295
6.927	0.231	1.08	291
7.328	0.231	1.08	294

2.2.3 Variation of "Magnetoresistance" r_B , and Hall Coefficient, R_H^B , with Magnetic Field, B_z , at 294°K

At 294°K , $E_H^B/R_H = 0.57$, so that from the values of θ_m and Fig. 6, $\lambda'/\omega' = 0.4$

B_z kG	$(-R_H^B)$ $\text{cm}^3 \text{cou}^{-1}$	$\text{Tan } \theta_m$	θ_m°	r_m	r_g	$r_B = r_m r_g$ (theory)	r_B (expt).
1.191	185	0.82	39.5	1.01	1.25	1.26	1.23
2.235	190	1.51	56.5	1.03	1.98	2.04	1.87
3.272	189	2.14	65.0	1.06	2.83	3.00	2.74
4.985	188	3.11	72.2	1.11	4.28	4.75	4.73
6.011	187	3.48	74.0	1.20	5.13	6.17	6.17
6.927	184	3.78	75.2	1.27	5.70	7.24	7.54
7.328	184	3.91	75.5	1.30	5.90	7.68	8.18
7.797	185	4.03	76.0	1.34	6.15	8.25	9.25

2.2.4 Variation of "Magnetoresistance" r_B , and Hall Coefficient, R_H^B , with Magnetic Field at 377°K.

At 377°K, $R_H^B/R_H \doteq 0.77$, so that from the values of θ_m and Fig. 6, $l'/\omega' = 1$.

B_z kG	$(-)\frac{R_H^B}{\text{cm}^3 \text{cou}^{-1}}$	Tan θ_m	θ_m°	r_m	r_g	$r_B = r_m r_g$ (theory)	r_B (expt)
1.191	59.2	0.612	32.0	1.00	1.16	1.16	1.09
2.235	60.4	1.13	48.1	1.02	1.44	1.46	1.31
4.205	60.5	2.07	64.2	1.05	2.06	2.16	2.00
4.985	60.6	2.42	67.5	1.06	2.32	2.46	2.35
6.011	60.6	2.81	70.4	1.09	2.66	2.90	2.94
6.927	60.0	3.12	72.3	1.14	3.00	3.42	3.41
7.328	60.0	3.24	72.9	1.46	3.08	3.58	3.72

2.2.5. Variation of "Magnetoresistance" r_B , and Hall Coefficient,

R_H^B , with Magnetic Field, B_z , at 529°K

At 529°K, $R_H^B/R_H \doteq 0.96$, so that from the values of θ_m and Fig. 6, $\ell'/\omega' = 3$

B_z kG	$(-)\frac{R_H^B}{\text{cm}^3 \text{cou}^{-1}}$	Tan θ_m	θ_m°	r_m	r_g	$r_B = r_m r_g$ (theory)	r_B (expt)
1.191	14.0	0.345	19.1	1.00	1.02	1.02	1.01
3.272	14.4	0.945	43.3	1.01	1.10	1.11	1.10
4.985	14.8	1.42	54.9	1.02	1.23	1.25	1.23
6.011	14.5	1.68	59.2	1.03	1.30	1.34	1.33
6.927	14.6	1.93	62.6	1.04	1.34	1.39	1.44
7.328	14.8	2.03	63.5	1.05	1.37	1.44	1.48

2.2.6 Variation of "Magnetoresistance" r_B , and Hall Coefficient

R_H^B , with Magnetic Field, B_z , at 696°K

At 696°K, $R_H^B/R_H \doteq 0.95$ so that from the values of θ_m and Fig. 6, $\ell'/\omega' = 3$.

B_z kG	$(-)\frac{R_H^B}{\text{cm}^3 \text{cou}^{-1}}$	Tan θ_m	θ_m°	r_m	r_g	$r_B = r_m r_g$ (theory)	r_B (expt.)
1.191	5.01	0.178	10.1	1.00	1.00(5)	1.00(5)	1.00
3.272	5.20	0.485	25.9	1.003	1.05	1.05	1.02
4.985	5.20	0.740	36.5	1.007	1.08	1.09	1.05
6.011	5.21	0.890	41.7	1.011	1.11	1.12	1.09
6.927	5.21	1.03	46.0	1.014	1.15	1.16	1.14
7.328	5.20	1.09	47.5	1.016	1.16	1.18	1.17

2.3 Results on InSb/NiSb Sample 3 in Orientation C

2.3.1 Variation of Hall Coefficient, R_H^C , Electrical Conductivity, σ , and R_H^C with Temperature

T °K	$T^{-1} \times 10^3$ °K ⁻¹	σ $\Omega^{-1} \text{cm}^{-1}$	R_H^C $\text{cm}^3 \text{coul}^{-1}$	$ R_H^C \sigma$ $\text{cm}^2 \text{V} \text{s}^{-1}$
77	13.0	2.12	+ 1230	2610
105	9.52	2.23	+ 583	1300
124	8.08	2.47	+ 292	7210
133	7.51	2.51	+ 146	366
144	6.93	3.65	-	-
157	6.38	4.51	- 252	1,140
173	5.77	9.20	- 476	4,390
180	5.55	12.3	- 656	8,070
192	5.21	22.0	- 752	16,500
208	4.80	-	- 735	-
216	4.63	57.1	- 705	40,300
265	3.77	154	- 342	52,700
292	3.45	247	- 226	55,800
320	3.13	381	- 148	56,400
331	3.02	447	- 123	55,000

T °K	$T^{-1} \times 10^3$ °K ⁻¹	$\Omega^{-1} \text{cm}^{-1}$	R_H^C cm ³ coul ⁻¹	$ R_H^C \sigma$ cm ² V ⁻¹ s ⁻¹
358	2.80	604	- 84.5	51,000
370	2.71	698	- 71.4	49,000
399	2.50	893	- 49.4	44,100
432	2.37	1080	- 37.6	40,600
461	2.17	1380	- 25.6	35,300
501	2.00	1710	- 17.8	30,400
529	1.89	2006	- 13.8	27,600
581	1.72	2390	- 9.96	23,800
621	1.61	2620	- 7.86	20,600
669	1.50	2930	- 5.89	17,300
683	1.47	2970	- 5.20	15,500

2.3.2 Variation of "Magnetoresistance" r_C , & Hall Coefficient R_H^C , with Magnetic Field, B_z , at 105°K.

B_z kG	$\Omega^{-1} \text{cm}^{-1}$	R_H^C cm ³ coul. ⁻¹
0	2.23	1
1.191	2.21	1.01
3.272	2.19	1.02
4.985	2.14	1.04
6.011	2.10	1.06
6.927	2.08	1.07
7.328	2.05	1.09

2.3.3 Variation of "Magnetoresistance" r_c , and Hall Coefficient R_H^C , with Magnetic Field, B_z , at 292°K

From equation (7.10) $R_H^C/R_H \cong 0.83$ and the values of θ^0 and Fig. 6 give $l/\omega' \cong 1.0$. The values of r_g

were then determined from Fig. 5 and of r_c using (7.25)

B_z kG	$(-R_H)$ $\text{cm}^3 \text{coul}^{-1}$	$\text{Tan } \theta_m$	θ_m^0	r_m	r_g	r_c (theory)	r_c (expt.)
1.191	214	0.82	39.5	1.01	1.25	1.21	1.06
2.235	225	1.51	56.5	1.03	1.63	1.55	1.23
3.272	226	2.14	65.0	1.05	2.10	1.64	1.49
4.985	228	3.11	72.2	1.11	2.80	2.07	1.99
6.011	229	3.48	74.0	1.20	3.21	2.68	2.38
6.927	226	3.78	75.2	1.27	3.36	2.90	2.71
7.328	224	3.91	75.5	1.30	3.47	2.99	2.83

2.3.4 Variation of "Magnetoresistance" r_c , and Hall Coefficient

R_H^C with Magnetic Field at 370°K

From equation (7.10), $R_H^C/R_H \doteq 0.93$ and the values of

θ° and Fig. 6 give $l/w' \doteq 2$. The values of r_g

were then determined from Fig. 5 and of r_c using (7.25)

B_z kG	$(-R_H)$ $\text{cm}^3 \text{coul}^{-1}$	Tan θ_m	θ_m°	r_m	r_g	r_c (theory)	r_c (expt.)
1.191	61	0.637	32.5	1.005	1.05	1.05	1.05
2.235	68	1.18	49.8	1.016	1.25	1.23	1.13
3.272	70	1.70	59.5	1.035	1.37	1.35	1.27
4.205	-	2.14	64.8	1.057	1.50	1.48	1.34
4.985	72	2.52	68.3	1.064	1.63	1.58	1.45
6.010	72	3.02	71.7	1.068	1.85	1.75	1.61
6.927	72	3.22	72.8	1.155	1.95	1.94	1.76
7.328	74	3.35	73.4	1.176	2.00	2.00	1.83

2.3.5 Variation of "Magnetoresistance" r_C and Hall Coefficient R_H^C with Magnetic Field at 529°K

From equation (7.10) $R_H^{Ct} / R_H^0 = 0.95$ and the values of θ^0 and Fig. 6 give $\lambda' / \omega' = 3$. The values of r_g were then determined from fig. 5 and of r_C using (7.25)

B_z kG	$(-R_H^C)$ $\text{cm}^3 \text{coul}^{-1}$	$\text{Tan } \theta_m$	θ_m^0	r_m	r_g	r_C (theory)	r_C (expt)
1.191	13.6	0.345	19.1	1.000	1.02	1.01	1.01
3.272	14.2	0.940	43.3	1.010	1.10	1.10	1.03
4.985	14.0	1.42	54.6	1.023	1.20	1.22	1.11
6.010	13.7	1.68	59.2	1.034	1.26	1.28	1.19
6.927	13.1	1.93	62.6	1.045	1.28	1.32	1.22
7.328	12.9	2.03	63.5	1.050	1.30	1.35	1.24

2.3.6 Variation of "Magnetoresistance" Γ_C , and Hall Coefficient

R_H^C , with Magnetic Field, B_z

From equation (7.10), $R_H^{Ct} / R_H \doteq 0.99$ and the values of θ^0 and Fig. 6 give $l/\omega' = 5$. The values of Γ_g were then determined from Fig. 5 and of Γ_C using (7.25).

B_z kG	$(-R_H^C)$ $\text{cm}^3 \text{coul}^{-1}$	$\text{Tan } \theta_m$	θ_m^0	Γ_m	Γ_g	Γ_C (theory)	Γ_C (expt)
1.191	4.3	0.183	10.4	1.000	1.00	1.00	1.00
3.272	5.24	0.505	26.8	1.000	1.04	1.04	1.01
4.905	4.99	0.768	37.5	1.00	1.06	1.06	1.05
6.011	5.12	0.925	42.7	1.010	1.08	1.08	1.06
6.927	5.18	1.04	46.1	1.013	1.09	1.10	1.08
7.328	5.40	1.12	48.3	1.014	1.11	1.12	1.09

Results at 77°K.

TABLE 7.7.

Sample	1	2	3
Orientation (α)	A	B	C
$\sigma \Omega^{-1} \text{cm.}^{-1}$	0.129	0.130	2.12
(+) $R_H^x \text{ coul.}^{-1} \text{cm.}^3$	7620	582	1230
r_x (7.3 kG.)	1.08	1.09	1.10

Despite the differences in R_H^A , R_H^B and R_H^C shown in the table above, the "geometrical" components of the resistivity are greatly reduced at 77°K. This is a result of mixed conduction being replaced by extrinsic hole conduction. In the extrinsic range the relative resistance of a corbino disc is

$$r = r_p r_g$$

where r_p is the physical magnetoresistance and r_g is the "geometrical" resistance. The value of the latter is given by ³⁷

$$\begin{aligned} r_g &= 1 + \tan^2 \theta_p \\ &= 1 + \mu_p^2 B_z^2 \end{aligned}$$

For a hole mobility, μ_p , of order $10^2 \text{ cm.}^2 \text{V.}^{-1} \text{S.}^{-1}$ and a magnetic field, B_z , of 7 kG., r_g does not depart from unity by more than 1%. As this type of sample gives the largest possible "geometrical" increase in resistance, then at 77°K the geometrical influence is unimportant in InSb/NiSb so that r_A , r_B and r_C all represent the physical magnetoresistance of the samples. The magnitude of the relative observed compare with the 4% increase in resistance ⁶⁸ observed by Champness with a sample of InSb containing 2×10^6 acceptors cm.^{-3}

The theory embodied in equations (2.16) and (2.17) shows that for a constant relaxation time and one type of carrier no

physical magnetoresistance is possible, so that an energy dependent relaxation process is probably responsible for the results observed. However, acoustic lattice scattering alone and ionised impurity scattering alone cannot account for the results observed, so that the relaxation process arises from a combination of scattering mechanisms which probably include ionised impurity scattering and dislocation scattering. It is felt, however, that a fuller investigation than was possible with the present apparatus is required before the results obtained at 77°K can be fully appreciated.

100	2.11	150	730	3.20	20
105	2.20	155	740	3.25	20
110	2.27	160	750	3.30	20
115	2.35	165	760	3.35	20
120	2.42	170	770	3.40	20
125	2.50	175	780	3.45	20
130	2.57	180	790	3.50	20
135	2.65	185	800	3.55	20
140	2.72	190	810	3.60	20
145	2.80	195	820	3.65	20
150	2.87	200	830	3.70	20
155	2.95	205	840	3.75	20
160	3.02	210	850	3.80	20
165	3.10	215	860	3.85	20
170	3.17	220	870	3.90	20
175	3.25	225	880	3.95	20
180	3.32	230	890	4.00	20
185	3.40	235	900	4.05	20
190	3.47	240	910	4.10	20
195	3.55	245	920	4.15	20
200	3.62	250	930	4.20	20
205	3.70	255	940	4.25	20
210	3.77	260	950	4.30	20
215	3.85	265	960	4.35	20
220	3.92	270	970	4.40	20
225	4.00	275	980	4.45	20
230	4.07	280	990	4.50	20
235	4.15	285	1000	4.55	20
240	4.22	290	1010	4.60	20
245	4.30	295	1020	4.65	20
250	4.37	300	1030	4.70	20
255	4.45	305	1040	4.75	20
260	4.52	310	1050	4.80	20
265	4.60	315	1060	4.85	20
270	4.67	320	1070	4.90	20
275	4.75	325	1080	4.95	20
280	4.82	330	1090	5.00	20
285	4.90	335	1100	5.05	20
290	4.97	340	1110	5.10	20
295	5.05	345	1120	5.15	20
300	5.12	350	1130	5.20	20
305	5.20	355	1140	5.25	20
310	5.27	360	1150	5.30	20
315	5.35	365	1160	5.35	20
320	5.42	370	1170	5.40	20
325	5.50	375	1180	5.45	20
330	5.57	380	1190	5.50	20
335	5.65	385	1200	5.55	20
340	5.72	390	1210	5.60	20
345	5.80	395	1220	5.65	20
350	5.87	400	1230	5.70	20
355	5.95	405	1240	5.75	20
360	6.02	410	1250	5.80	20
365	6.10	415	1260	5.85	20
370	6.17	420	1270	5.90	20
375	6.25	425	1280	5.95	20
380	6.32	430	1290	6.00	20
385	6.40	435	1300	6.05	20
390	6.47	440	1310	6.10	20
395	6.55	445	1320	6.15	20
400	6.62	450	1330	6.20	20
405	6.70	455	1340	6.25	20
410	6.77	460	1350	6.30	20
415	6.85	465	1360	6.35	20
420	6.92	470	1370	6.40	20
425	7.00	475	1380	6.45	20
430	7.07	480	1390	6.50	20
435	7.15	485	1400	6.55	20
440	7.22	490	1410	6.60	20
445	7.30	495	1420	6.65	20
450	7.37	500	1430	6.70	20
455	7.45	505	1440	6.75	20
460	7.52	510	1450	6.80	20
465	7.60	515	1460	6.85	20
470	7.67	520	1470	6.90	20
475	7.75	525	1480	6.95	20
480	7.82	530	1490	7.00	20
485	7.90	535	1500	7.05	20
490	7.97	540	1510	7.10	20
495	8.05	545	1520	7.15	20
500	8.12	550	1530	7.20	20
505	8.20	555	1540	7.25	20
510	8.27	560	1550	7.30	20
515	8.35	565	1560	7.35	20
520	8.42	570	1570	7.40	20
525	8.50	575	1580	7.45	20
530	8.57	580	1590	7.50	20
535	8.65	585	1600	7.55	20
540	8.72	590	1610	7.60	20
545	8.80	595	1620	7.65	20
550	8.87	600	1630	7.70	20
555	8.95	605	1640	7.75	20
560	9.02	610	1650	7.80	20
565	9.10	615	1660	7.85	20
570	9.17	620	1670	7.90	20
575	9.25	625	1680	7.95	20
580	9.32	630	1690	8.00	20
585	9.40	635	1700	8.05	20
590	9.47	640	1710	8.10	20
595	9.55	645	1720	8.15	20
600	9.62	650	1730	8.20	20
605	9.70	655	1740	8.25	20
610	9.77	660	1750	8.30	20
615	9.85	665	1760	8.35	20
620	9.92	670	1770	8.40	20
625	10.00	675	1780	8.45	20
630	10.07	680	1790	8.50	20
635	10.15	685	1800	8.55	20
640	10.22	690	1810	8.60	20
645	10.30	695	1820	8.65	20
650	10.37	700	1830	8.70	20
655	10.45	705	1840	8.75	20
660	10.52	710	1850	8.80	20
665	10.60	715	1860	8.85	20
670	10.67	720	1870	8.90	20
675	10.75	725	1880	8.95	20
680	10.82	730	1890	9.00	20
685	10.90	735	1900	9.05	20
690	10.97	740	1910	9.10	20
695	11.05	745	1920	9.15	20
700	11.12	750	1930	9.20	20
705	11.20	755	1940	9.25	20
710	11.27	760	1950	9.30	20
715	11.35	765	1960	9.35	20
720	11.42	770	1970	9.40	20
725	11.50	775	1980	9.45	20
730	11.57	780	1990	9.50	20
735	11.65	785	2000	9.55	20
740	11.72	790	2010	9.60	20
745	11.80	795	2020	9.65	20
750	11.87	800	2030	9.70	20
755	11.95	805	2040	9.75	20
760	12.02	810	2050	9.80	20
765	12.10	815	2060	9.85	20
770	12.17	820	2070	9.90	20
775	12.25	825	2080	9.95	20
780	12.32	830	2090	10.00	20
785	12.40	835	2100	10.05	20
790	12.47	840	2110	10.10	20
795	12.55	845	2120	10.15	20
800	12.62	850	2130	10.20	20
805	12.70	855	2140	10.25	20
810	12.77	860	2150	10.30	20
815	12.85	865	2160	10.35	20
820	12.92	870	2170	10.40	20
825	13.00	875	2180	10.45	20
830	13.07	880	2190	10.50	20
835	13.15	885	2200	10.55	20
840	13.22	890	2210	10.60	20
845	13.30	895	2220	10.65	20
850	13.37	900	2230	10.70	20
855	13.45	905	2240	10.75	20
860	13.52	910	2250	10.80	20
865	13.60	915	2260	10.85	20
870	13.67	920	2270	10.90	20
875	13.75	925	2280	10.95	20
880	13.82	930	2290	11.00	20
885	13.90	935	2300	11.05	20
890	13.97	940	2310	11.10	20
895	14.05	945	2320	11.15	20
900	14.12	950	2330	11.20	20
905	14.20	955	2340	11.25	20
910	14.27	960	2350	11.30	20
915	14.35	965	2360	11.35	20
920	14.42	970	2370	11.40	20
925	14.50	975	2380	11.45	20
930	14.57	980	2390	11.50	20
935	14.65	985	2400	11.55	20
940	14.72	990	2410	11.60	20
945	14.80	995	2420	11.65	20
950	14.87	1000	2430	11.70	20
955	14.95	1005	2440	11.75	20
960	15.02	1010	2450	11.80	20
965	15.10	1015	2460	11.85	20
970	15.17	1020	2470	11.90	20
975	15.25	1025	2480	11.95	20
980	15.32	1030	2490	12.00	20
985	15.40	1035	2500	12.05	20
990	15.47	1040	2510	12.10	20
995	15.55	1045	2520	12.15	20

Variation of Thermal Conductivity, K, and Thermoelectric Power,
 α , of InSb/NiSb with Temperature T.

T $^{\circ}\text{K}$	$K_{11} \times 10^{-2}$ $\text{cal. S}^{-1} \text{cm}^{-1}$ $^{\circ}\text{K}^{-1}$	α_{11} $\mu\text{V}^{\circ}\text{K}^{-1}$	T° $^{\circ}\text{K}$	$K_{\perp} \times 10^{-2}$ $\text{cal. S}^{-1} \text{cm}^{-1}$ $^{\circ}\text{K}^{-1}$	α_{\perp} $\mu\text{V}^{\circ}\text{K}^{-1}$
325	3.13	189	330	3.20	261
373	2.70	182	410	2.55	219
321	3.17	179	368	2.79	237
427	2.52	178	454	2.12	194
314	3.21	178	501	1.96	174
472	2.24	171	551	1.84	168
314	3.16	176	448	2.13	193
534	2.16	166	599	1.78	156
321	3.32	182	527	1.87	170
397	2.72	183	328	3.20	263
322	3.31	182			
389	2.66	180			
383	2.75	184			
314	3.40	181			
347	2.97	185			
358	3.00	187			
339	3.19	188			
590	2.01	154			